

# **STUDY ON STAR FORMING REGIONS IN WOLF RAYET GALAXIES**

THESIS

For the degree of  
DOCTOR OF PHILOSOPHY  
(PHYSICS)

Submitted to  
**KUMAUN UNIVERSITY**  
NAINITAL

by

**CHRISPHIN KARTHICK, M**

**ARYABHATTA RESEARCH INSTITUTE OF  
OBSERVATIONAL SCIENCES(ARIES)**

Manora Peak, Nainital-263 129

April 2012

- 1. Name of the Supervisor** : Dr. B. B. Sanwal,  
Aryabhata Research Institute of  
Observational Sciences,  
Manora Peak,(ARIES),  
Nainital 263 129, India.
  
- 2. Name of the Co-Supervisor** : Dr. Shuchi Bisht,  
Department of Physics, DSB Campus,  
Kumaun University,  
Nainital 263 129, India.
  
- 3. Name of the Research Institute** : Aryabhata Research Institute of  
Observational Sciences,  
Manora Peak, Nainital 263 129,  
Uttarakhand, India.

Collaborators: Dr. D. K. Sahu, Associate Professor from Indian Institute of Astrophysics(IIA) and Dr. Ángel López-Sánchez, Joint Anglo Australia Telescope(AAO) & Macquarie University, Post doctoral Fellow, Australia.

## DECLARATION

I hereby declare that the work presented in this thesis is a result of the investigation carried out by me at the Aryabhata Research Institute of observational sciencES (ARIES), Nainital, under the joint supervision of Dr. B. B. Sanwal (ARIES) and Dr. Shuchi Bisht (Department of Physics, Kumaun University, Nainital). This thesis has not been submitted for the award of any degree, diploma, associateship or fellowship of any other University or Institute.

Place: Nainital

Date: 04/04/2012



(Chrispin Karthick, M)

ARIES, Manora Peak,

Nainital 263 129.

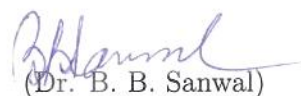
## CERTIFICATE FROM THE SUPERVISOR

This is to certify that

1. The thesis submitted by Chrisphin Karthick, M on the topic entitled, **“Study on Star Forming Regions in Wolf Rayet Galaxies”** embodies the work of the candidate himself for the award of the degree of Doctor of Philosophy in Physics was approved by the Kumaun University, Nainital.
2. The candidate worked under the joint supervision of myself and Dr. Shuchi Bisht, Department of Physics, Kumaun University, Nainital for the period required under the ordinance for Ph.D. degree programme of Kumaun University, Nainital on this thesis as a Research Fellow at ARIES, Nainital.
3. This thesis has not been submitted for the award of any degree, diploma, associateship, fellowship, etc of any other University or Institute.

Place: Nainital

Date: 4/4/2012

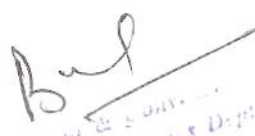


(Dr. B. B. Sanwal)

ARIES, Manora Peak,  
Nainital 263 129.

Forwarded by :

Head, Department of Physics &  
Convener, RDC,  
Kumaun University.



Head of Department  
RDC Physics Dept  
Kumaun University,  
NAINITAL (U.K.) 263001

---

## CERTIFICATE FROM THE CO-SUPERVISOR

This is to certify that

1. The thesis entitled “**Study on Star Forming Regions in Wolf Rayet Galaxies**” for the award of the degree of Doctor of Philosophy in Physics was approved by the Kumaun University, Nainital.
2. This thesis embodies the work of Mr. Chrisphin Karthick, M himself.
3. Mr. Chrisphin Karthick, M worked under my supervision on this thesis as a Research Fellow at ARIES, Nainital.
4. This thesis has not been submitted for the award of any degree, diploma, associateship, fellowship, etc of any other University or Institute.

Place: Nainital

Date : 3/4/12



(Dr. Shuchi Bisht)  
Department of Physics,  
Kumaun University,  
Nainital 263 002.

*To*  
*My Dear Father*  
*&*  
*Mother...*

# *Acknowledgements*

I thank Dr. B. B. Sanwal, for being my supervisor, being helpful and supportive till my completion of thesis work, without his acceptance and co-operation I could not come upto this stage. I thank Prof. Ram Sagar, ARIES for his career guidance and help. I admire his speech and scientific thoughts and handling things softly and wisely from whom I learned many things. And thanks to Dr. Shuchi Bisht, Kumaun university for her kind support and accepting to be a co-supervisor for my work.

I thank Dr. D. K. Sahu, IIA for his great support for my work till the end, whose contact and collaborative work gave me turning point in my Ph.D career. I thank Ramya Sethuram, IIA from whom I could learn my beginning scientific work stuffs. I heartfully thank Prof. T. P. Prabhu, IIA for his great support for my work by giving permission to stay at CREST, without this stay at CREST campus all these work were not be concluded nicely. I thank very much to my well wisher Dr. Stalin ji, IIA for his strong encouragement and support from the beginning of my work to till end. I thank Time Allocation Committee (HCT) for allotting time for my observations in HCT. It was a very nice experience being at IIA-CREST campus and working for my Ph.D. I heart fully thank once again Dr. D. K. Sahu, because of whose co-operation, I could make use of this visit and could use all the facilities.

I also give very BIG thanks to Dr. Angel Lopez-Sanchez, from Anglo Australian Observatory & Macquarie University, Australia for his great support from beginning (2008 Onwards) to till now by giving updated ideas in my work and who was so close and very kind enough to interact and share about all my scientific problems. His entry was really helpful. Especially I really felt great during my final phase of Ph.D. Also, thanking to Dr. Ian Stevans from University of Birmingham for his suggestions.

And I thank my dear friend Chhavi Pant who was very supportive and encouraged me all the time and helped me in all the ways. I also thank my dear friend Eswar, with whom I had a very nice time in ARIES. His company was very pleasant because of him I felt like lived an another college life. It was really memorable. I thank my dear family friend Jessy jose, who was very supportive

and encouraged me towards my Ph.D work. And who helped me voluntarily when I was in need of any help. I also thank Manash for his help and support during the last phase. A special thanks to Hem (Chhavi's husband) who was so keen on me to finish my Ph.D, and tried to help me in many ways. And also a very special thanks to Sindhuja. M, from NIT-T who was very supportive and encouraged me constantly in my ups and downs. I thank Arti Goyal for her timing collaboration on AGN which made me to explore my interest in AGN-starburst connection. And, I heart fully thank to my dear best friend and my ultimate physics GURU Dr. Valan Bruno Cruz, Post Doc fellow at Germany and my best buddy ever in science; From my B.Sc to now; From whom I learned what is physics? apart from being an amateur astronomer from my college days to now. He helped me in many ways, throughout my physics life. I really proud to say that He is my friend and a real scientist with whom I spent 3 years of my college life to now. And thanks to Vishnu, IIT, Chennai and dear Berdil who were with me in my difficult times. Also, I thank to my dear school friend Satheesh Kumar; whose philosophical thoughts and approach made me to come in this science way. And I thank my other colleagues Uday, IIA who shared his observing nights with me and Pepsi Anto from IIA who helped for my observation in HCT.

I remember my B.Sc Seniors Avinash and Ramkarthick (who we used to say and as Sir C. V. Raman's relation; IIT-M) were my inspiration and made my love towards physics. Also, I thank my college mates Bala from Max planck Institute, Heidelberg, Germany, Vino from Univeristy of Brimingam and my junior in college Balagopal, WIPRO who was always talking about physics and its problem solving which made me to be enthusiasm in physics more and also thank to friend Dr. Sridhar, IMsc, Chennai and also inspiration of Sai, IIT-M (2000-2003), Prabha (Caltech) and Dr. Soundrajaperumal, Deputy Director of Chennai Birla planetarium because of whom all those people contacts and thoughts, I really felt like am always being in scientific environment and felt the same all through in my scientific career.

I thank Prof. J. N. Goswami, PRL for his guidance to choose this Ph.d. option and I also thank Prof. S. V. S. Murty, PRL for the same. I thank other faculties(scientists) Muthu ji, Hum chand ji, Biman dha, Dr. Brijesh Kumar, Jeevandha, Shashi Bhushan Pandey ji, Mahesh ji, Sanjit Sahu ji and Dr. Mahendra Singh for their supportive thoughts and encouragement. Also, here I remember

Rev. Fr. Victor, Rev. Fr. Boniface Jayaraj and Rev. Fr. Lourdu Xavier from Loyola College, Chennai for their great support in my college days towards my scientific career which made me to come through all these journey. I thank all Manora village people who made my stay in Nainital memorable. Every one might have helped me at some circumstances, when I was in need. So I do not want miss anyone's name, hence I thank all those people and research scholars of ARIES, IIA and CREST campus who made my stay and work so memorable and enjoyable.

I acknowledges the financial assistance through a sponsored project Grant No: SR/S2/HEP-10/2002 of Department of Science and Technology (DST), Government of India, New Delhi for the project entitled 'Study on star forming regions in Wolf-Rayet galaxies" with the position of JRF and SRF. This research has made use of the NASA/IPAC Extragalactic Database (NED) which is operated by the Jet Propulsion Laboratory, California Institute of Technology, under contract with the National Aeronautics and Space Administration. This research has made extensive use of the SAO/NASA Astrophysics Data System Bibliographic Services (ADS).

At last but, not the least I thank my Mother, Sister & Constone and mainly to my dear Zenith (niece) who was so patience till my Ph.D. work completion and gave me a moral support and encouragement. And very special thanks to my dear cute Zenith (5th std, Chennai) who always strongly believes about her 'Mama' as great and high and encouraged 'Him' all the time.

" Many people are coming and going in our day to day life; But very few only remains in our heart ; Thanks for those all heartfelt people. "

- Chrisphin Karthick .M

# *List of Publications*

## **Refereed Journals**

Photometric and spectroscopic studies of star-forming regions within Wolf-Rayet Galaxies;

**Chrisphin Karthick, M.**, López-Sánchez Ángel R., Sahu, D. K., Sanwal, B. B., Bisht, S.

(2012 submitted to the MNRAS journal).

**2011 MNRAS.416..101G**

Rapid optical variability of TeV blazars

Gopal-Krishna, Goyal, A., Joshi, S., **Karthick, Chrisphin.**, Sagar, R., Wiita, Paul J., Anupama, G. C., Sahu, D. K.

## **Book**

**2012 LAP**

"Astronomer's Data Reduction Guide"

**Chrisphin karthick. M**, LAP Lambert Academic Publishing, Pp 123

ISBN:978-3-8473-3193-3, Germany.

## **Conference Proceedings**

**2008 BASI...25S..66C**

Proc. 25th meeting of ASI (2007), p. 66, 25, 66

Photometric and Spectrophotometric studies on Wolf-Rayet Galaxies

**Chrisphin, K.**, Sanwal, B. B., Sahu, D. K., and Singh, M.

**2011 AAS...21832703W.**

American Astronomical Society, AAS Meeting #218, #327.03;

Bulletin of the American Astronomical Society, Vol. 43, 2011

Intranight Optical Variability of Core Dominated Quasars and TeV Blazars.

Wiita, P. J. and Goyal, A. and Krishna, G. and Anupama, G. C. and Sahu, D. K. and Joshi, S. and **Karthick, C.** and Sagar, R.

**In Preparation** <sup>1</sup>

**Book**

Astronomer's Guide.

**2012** Springer

**Chrisphin Karthick**

Wolf Rayet Galaxy NGC 2403

**2012** MNRAS

**Chrisphin Karthick et al.**

WR galaxies NGC 3995, NGC 5430 and MRK 1239

**2012** MNRAS

**Chrisphin Karthick et al.**

---

<sup>1</sup>Title and journal are tentative; Subject to change.

*“My goal is simple. It is a complete understanding of the universe,  
why it is as it is and why it exists at all.”*

*- Stephen Hawking*

# Contents

<b>List of Publications</b>	<b>viii</b>
<b>List of Figures</b>	<b>xv</b>
<b>List of Tables</b>	<b>xix</b>
<b>Abbreviations and Notations</b>	<b>xxi</b>
<b>Physical Constants</b>	<b>xxv</b>
<b>1 Introduction</b>	<b>1</b>
1.1 Introduction . . . . .	1
1.1.1 Types of Galaxies . . . . .	3
1.1.2 Starburst Galaxy . . . . .	10
1.1.3 AGN-Starburst Connection . . . . .	11
1.2 Wolf-Rayet Definition . . . . .	12
1.2.1 Wolf-Rayet Star . . . . .	13
1.2.2 Wolf-Rayet Galaxies . . . . .	16
1.3 Star Forming Regions in a Galaxy . . . . .	18
1.3.1 H II regions . . . . .	18
1.3.2 Physical processes in H II region . . . . .	19
1.3.3 Formation of Forbidden lines . . . . .	20
1.3.4 Solar abundances . . . . .	21
1.3.5 Metallicity . . . . .	23
1.4 Motivation . . . . .	25
1.4.1 Thesis Outline . . . . .	26
<b>2 Observations and Data Analysis</b>	<b>29</b>
2.1 Introduction . . . . .	29
2.2 Observations . . . . .	30
2.2.1 Instruments Used . . . . .	30

2.2.2	Scientific Objectives	32
2.2.3	Sample Selection	33
2.3	Data Reductions	35
2.3.1	Pre-Processing	36
2.3.2	Cleaning	36
2.3.3	Aligning and Combining of sub exposure frames	37
2.4	Processing	38
2.4.1	Aperture photometry	38
2.4.2	Calibrating Instrumental Magnitudes	39
2.4.3	Determination of Extinction Coefficients	40
2.5	Post-Processing	41
2.6	Spectroscopic Reduction	42
2.6.1	Introduction	42
2.6.2	Observations	44
2.6.3	Instruments Used	44
2.7	Data reduction	45
2.7.1	Aperture Extraction	45
2.7.2	Wavelength Calibration	46
2.7.3	Flux Calibration	47
<b>3</b>	<b>Star Formation Rate</b>	<b>49</b>
3.1	Introduction	49
3.2	Observations	50
3.3	Identifying Star forming Regions	50
3.4	Continuum Subtraction	52
3.4.1	Methodology	52
3.4.2	Continuum Subtracted Images of WR Galaxies	54
3.4.3	Arc distance	62
3.5	Calculation of flux in IRAS 07164+5301	63
3.6	SFR relation	65
3.7	Narrow band H $\alpha$ photometry	66
3.8	Agnes of the most recent star-forming event	68
<b>4</b>	<b>Oxygen abundances</b>	<b>71</b>
4.1	Introduction	71
4.2	Observations	72
4.3	Reddening Correction	73
4.3.1	C(H $\beta$ ) through reddening Correction	74
4.4	R23 indicator	75
4.5	Optical Spectra of analyzed WR Galaxies	77
4.6	Results from optical spectroscopy	84
4.6.1	Physical conditions of the ionized gas	86

---

4.6.2	Estimation of the chemical abundances . . . . .	88
4.6.3	Analysis of the WR features . . . . .	92
<b>5</b>	<b>Stellar Populations</b>	<b>95</b>
5.1	Introduction . . . . .	95
5.2	Observations . . . . .	96
5.3	Model Starburst99 . . . . .	96
5.4	Broad-band Photometry results . . . . .	100
5.5	Ages of the dominant stellar populations . . . . .	100
<b>6</b>	<b>Analysis of individual galaxies</b>	<b>113</b>
6.1	NGC 1140 . . . . .	113
6.2	IRAS 07164+5301 . . . . .	115
6.3	NGC 3738 . . . . .	116
6.4	UM 311 . . . . .	117
6.5	NGC 6764 . . . . .	118
6.6	NGC 4861 . . . . .	120
6.7	NGC 3003 . . . . .	121
<b>7</b>	<b>Summary, Conclusions and Future Prospects</b>	<b>123</b>
7.1	Summary . . . . .	123
7.2	Conclusion . . . . .	125
7.3	Future Prospects . . . . .	128
7.3.1	Continuation of Optical studies . . . . .	128
7.3.2	Multiwavelength Studies of Galaxies . . . . .	128
7.3.3	Proping the AGN-Starburst Connection . . . . .	130
	<b>Appendices</b>	<b>132</b>
<b>A</b>	<b>HCT- H<math>\alpha</math> Filter Response Curve</b>	<b>133</b>
<b>B</b>	<b>Solar abundances</b>	<b>135</b>
<b>C</b>	<b>Empirical calibrations of the oxygen abundance</b>	<b>137</b>



# List of Figures

1.1	Hubble classification of galaxies (Mark & Robert 2003) . . . . .	4
1.2	Illustrates the Unified Model of AGN classification with respect to viewing from different angle line of sight.(Arrow marked). . . . .	7
1.3	Spectrum of different types of Galaxies (Image credit: Srateva et al 2001;) . . . . .	9
1.4	Evolution of WR star . . . . .	14
1.5	Observational evidence of the presence of hot and massive "Wolf-Rayet" stars in a metal-rich H II region (designated "-014+081") in the spiral galaxy NGC 4254, a member of the Virgo cluster of galaxies at a distance of about 50 million light-years. Comparison spectra of two types of Wolf-Rayet stars (WC and WN) in the Milky Way galaxy are shown. The characteristic spectral features of ionized helium (He II) and double and triple ionized carbon (C III, C IV) are identical. (Image credit: Press release of ESO image Id: eso0223c, 15/02; & Lopez Sanchez Thesis 2006) . . . . .	16
1.6	A typical H II Regions Spectra . . . . .	19
1.7	Different optical energy level transitions for [O II] and [O III]. "g" is the ground state and "m" is the metastable state(s). Splitting not to scale. . . . .	21
1.8	Plot of mean abundances by number in the Solar scale against atomic number . . . . .	22
2.1	HCT 2-m Telescope . . . . .	30
2.2	ARIES 1-m Telescope . . . . .	32
2.3	Typical Star spectra (WIP graphics courtesy T.Tomov) . . . . .	43
3.1	Broad-band R filter image of NGC 1140. . . . .	55
3.2	Continuum subtracted H $\alpha$ image of NGC 1140. . . . .	55
3.3	Broad-band R filter image of IRAS 07164+5301 . . . . .	56
3.4	continuum subtracted H $\alpha$ image of IRAS 07164+5301 . . . . .	56
3.5	Broad-band R filter image of NGC 3738 . . . . .	57
3.6	Continuum subtracted H $\alpha$ image of NGC 3738 . . . . .	57
3.7	Broad-band R filter image of UM 311 . . . . .	58
3.8	Continuum subtracted H $\alpha$ image of UM 311 . . . . .	58
3.9	Broad-band R filter image of NGC 6764 . . . . .	59

3.10	Continuum subtracted H $\alpha$ image of NGC 6764 . . . . .	59
3.11	Broad-band R filter and continuum subtracted H $\alpha$ image of NGC 4861 . . . . .	60
3.12	Broad-band R filter and continuum subtracted H $\alpha$ image of NGC 4861 . . . . .	60
3.13	Broad-band R filter image of NGC 3003 . . . . .	61
3.14	Continuum subtracted H $\alpha$ image of NGC 3003 . . . . .	61
3.15	Plot of knots ID Vs equivalent width of NGC 3003 . . . . .	62
4.1	Image credit: Lopez 2010 et al. Empirical calibrations of oxygen abundance using the R23 parameter. Note that they are bi-valuated. The dashed zone indicates the region with higher uncertainties in O/H. The empirical calibrations plotted in the figure are: EP94: Edmunds & Pagel (1984); M91: McGaugh (1991) using $y = 0$ (R2 = R3 ); P01: Pilyugin (2001) using $P = 0.5$ (R2 = R3 ); (KD02+KK04): Kewley & Dopita (2002) using the formulation of Kobulnicky & Kewley (2004) assuming $q = 7.5 \times 10^7 \text{ cm s}^{-1}$ ; N06: Nagao et al. (2006) using their cubic fit to R23. (See Appendix.C for more ) . . . . .	76
4.2	Spectrum of the galaxy NGC 1140 . . . . .	78
4.3	Spectrum of the galaxy IRAS 07164+5301 . . . . .	78
4.4	Spectrum of the galaxy NGC 3738 . . . . .	79
4.5	Spectrum of the galaxy UM 311 . . . . .	79
4.6	Spectrum of knot region ID:1 of the galaxy NGC 6764 . . . . .	80
4.7	Spectrum of central region of the galaxy NGC 6764 . . . . .	80
4.8	Spectrum of the galaxy NGC 4861 . . . . .	81
4.9	Spectrum of the galaxy NGC 3003 . . . . .	81
4.10	WR Blue bump spectrum of the galaxy NGC 1140 . . . . .	82
4.11	WR red bump spectrum of the galaxy NGC 1140 . . . . .	82
4.12	WR Blue bump spectrum of the galaxy NGC 4861 . . . . .	83
4.13	WR Red bump spectrum of the galaxy NGC 4861 . . . . .	83
4.14	Comparison of some observational flux ratios obtained for all analyzed WR galaxies (black crosses) with the diagnostic diagrams proposed by Dopita et al. (2000), blue continuous line (D00), and Kewley et al. (2001), red discontinuous line (K01). The left panel also shows the empirical relation provided by Kauffmann et al. (2003) with a dotted-dashed dark yellow line (Ka03). We also plot the observed flux ratios for the center of NGC 6764 (red x), which is classified as a LINER. . . . .	87
5.1	SB99 model plot of NGC 1140 (Knot IDs 1, 2, 3 and 4), IRAS 07164+5301, UM 311 and NGC 3738 for the metallicity $z=0.008$ . . . . .	101
5.2	SB99 model plot of NGC 6764 for the metallicity $z=0.008$ . . . . .	102

5.3	SB99 model plot of NGC 3738 and UM 311 for the metallicity $z=0.008$ . . . . .	103
5.4	SB99 model plot of NGC 3003 for the metallicity $z=0.02$ . . . . .	104
5.5	foreground corrected Colour-Colour plot of the galaxy NGC 1140, for the metallicity $z=0.008$ ; (a) U-B Vs B-V (b) B-V Vs V-R (c) V-R Vs V-I (d)U-B Vs V-I . . . . .	106
5.6	Colour-Colour plot of the galaxy IRAS 07164+5301, for the metallicity $z=0.008$ ; (a) U-B Vs B-V (b) B-V Vs V-R (c) V-R Vs V-I (d)U-B Vs V-I . . . . .	107
5.7	Foreground corrected colour-colour plot of the galaxy NGC 3738, for the metallicity $z=0.008$ ; (a) U-B Vs B-V (b) B-V Vs V-R (c) V-R Vs V-I (d)U-B Vs V-I . . . . .	108
5.8	Foreground corrected colour-colour plot of the galaxy UM 311, for the metallicity $z=0.008$ ; In this figure only ID number 3 is the galaxy other ID's 1 and 2 are near by galaxies. (a) U-B Vs B-V (b) B-V Vs V-R (c) V-R Vs V-I (d)U-B Vs V-I . . . . .	109
5.9	Foreground corrected colour-colour plot of the galaxy NGC 6764, for the metallicity $z=0.008$ ; (a) U-B Vs B-V (b) B-V Vs V-R (c) V-R Vs V-I (d)U-B Vs V-I . . . . .	110
5.10	Foreground corrected colour-colour plot of the galaxy NGC 4861, for the metallicity $z=0.008$ ; (a) U-B Vs B-V (b) B-V Vs V-R (c) V-R Vs V-I (d)U-B Vs V-I . . . . .	111
5.11	Foreground corrected colour-colour plot of the galaxy NGC 3003, for the metallicity $z=0.008$ ; (a) U-B Vs B-V (b) B-V Vs V-R (c) V-R Vs V-I (d)U-B Vs V-I . . . . .	112
7.1	An example for advantage of Multiwavelength studies in galaxies	129
A.1	HCT-H $\alpha$ Filter response curve ( $66563/100 \text{ \AA}$ ) . . . . .	134
B.1	Element abundances in the present-day solar photosphere. (Asplund, Grevesse & Sauval 2005) . . . . .	136
C.1	Empirical calibrations of oxygen abundance using the $R_{23}$ parameter. Note that they are bi-valuated. The dashed zone indicates the region with higher uncertainties in O/H. The empirical calibrations plotted in the figure are: EP94: Edmund & Pagel (1984); M91: McGaugh (1991) using $y=0$ ( $R_2 = R_3$ ); P01: Pilyugin (2001) using $P = 0.5$ ( $R_2 = R_3$ ); (KD02+KK04): Kewley & Dopita (2002) using the formulation of Kobulnicky & Kewley (2004) assuming $q = 7.5 \times 10^7 \text{ cm s}^{-1}$ ; N06: Nagao et al. (2006) using their cubic fit to $R_{23}$ (Lopez sanchez et al 2010). . . . .	138



# List of Tables

2.1	System parameters of the telescope, filters and detectors used for observations . . . . .	31
2.2	List of WR galaxies observed in our study <sup>a</sup> . . . . .	34
2.3	List of Standards Observed . . . . .	35
3.1	H $\alpha$ Observations . . . . .	50
3.2	H $\alpha$ flux, H $\alpha$ luminosity (corrected for extinction and [NII]) and derived star-formation rate for the knots of the WR galaxies analyzed in this work. . . . .	69
4.1	Low Resolution Spectroscopic Observations . . . . .	73
4.2	Dereddened line intensity ratios with respect to $I(\text{H}\beta)=100$ for the galaxies analyzed in this work. We also compile the H $\beta$ flux, the size of the extracted area, the reddening coefficient, $c(\text{H}\beta)$ , and the equivalent widths of the absorption in the hydrogen lines, $W_{abs}$ , used to correct the spectra for internal reddening, and the equivalent widths of the emission H I Balmer lines. . . . .	85
4.3	Physical conditions and chemical abundances of the ionized gas of the regions analyzed in NGC 1140 and NGC 4861. . . . .	88
4.4	Parameters used to derive the oxygen abundance following the strong emission-line methods. . . . .	90
4.5	Oxygen abundances derived for our WR galaxy sample using the most commonly used strong emission-line methods. Last two columns compile the adopted oxygen abundance and the branch (lower, medium or upper) used. The third column also lists previous estimations of the O/H ratio in the literature. The strong emission-line calibrations are: M91: McGaugh (1991); KD02: Kewley & Dopita (2002); PT05: Pilyugin & Thuan (2005); P01: Pilyugin (2001a,b); PP04a: Pettini & Pagel (2004), using a linear fit to the $N_2$ parameter; PP04c: Pettini & Pagel (2004), using the $O_3N_2$ parameter. . . . .	91
5.1	Details of optical broad-band observations . . . . .	96
5.2	Results of the analysis of the broad-band photometry in the detected star-forming regions within our WR galaxy sample. . . . .	99

---

5.3 Estimation of the age of the young and old stellar populations using the broad-band colors. . . . .	105
--	-----

# Abbreviations and Notations

The most commonly used notations and abbreviations in the thesis are given below. If a symbol has been used in a different connection than listed here, it has been explained at the appropriate place.

ADU	Analog-to-Digital Unit
AGN	Active Galactic Nuclei
BLAZARS	Blazing quasi-stellar object
BCD	Blue Compact Dwarf Galaxies
CCD	Charge-Couple Device
FIR	Far infrared
FOV	Field Of View
FWHM	Full Width at Half Maximum
GMC	Giant Molecular Cloud
HCT	Himalayan Chandra Telescope
HFSOC	Hanle Faint Object Spectrograph Camera
hr	hour
IMF	Initial Mass Function
INOV	Intra Night Optical variability
IRAF	Image Reduction and Analysis Facility
IRAS	Infrared Astronomical Satellite
IR	Infra-Red
ISM	Inter Stellar Medium

---

kpc	Kiloparsec(unit of distance)
LF	Luminosity Function
LINER	Low-Ionization Nuclear Emission-line Region
LMC	Large Magellanic Cloud
mag	magnitude (stellar)
MHz	Mega Hertz
MIDAS	Munich Image Data Analysis System
Myr	Million year
NGC	New General Catalogue
PSF	Point Spread Function
QSO	Quassi-Stellar object
SED	Spectral Energy Distribution
SFE	Star Forming Efficiency
SFR	Star Formation Rate
ST	Sampurnanand telescope
SDSS	Sloan Digital Sky Survey
UV	Ultra-violet
Tev	Tera electron Volt
yr	Year/Years

**Abbreviations of Journals and Books**

A&A	Astronomy and Astrophysics
ApJ	Astrophysical Journal
AJ	Astronomical Journal
ARAA	Annual Reviews of Astronomy and Astrophysics
ASI	Astronomical Society of India
BASI	Bulletin of Astronomical Society of India
MNRAS	Monthly Notices of Royal Astronomical Society
LAP	Lambert Academic Publishers

---

$A_V$	Total absorptions in the visual magnitude
$A_V$	Extinction in V filter (5500 Å)
$U, B, V, R, I$	Apparent standard magnitudes in optical filters
$(U - B), (B - V), (V - R)$	Apparent standard colours
$(V - I), (U - I)$	
$\text{dex}(x)$	$10^x$
$E(B-V)$	Colour excess
$E(B-V)_{Fore}$	Foreground Colour extinction
$E(B-V)_{intrinsic}$	Intrinsic Colour extinction
$L_\odot$	Luminosity of the Sun
$M_\odot$	Mass of the Sun
$m_v$	Apparent visual magnitude
$M_V$	Absolute visual magnitude
$R_V$	Ratio of total to selective absorption, $A_V/E(B-V)$
$\alpha$	Right ascension
$\delta$	Declination
$T_e$	Electron temperature
X	Airmass
$Z_\odot$	Solar Metallicity

# Physical Constants

The most commonly used constants in the thesis are given below.

Solar Mass ( $M_{\odot}$ )	$1.98892 \times 10^{30}$ kilograms
Solar Luminosity ( $L_{\odot}$ )	$3.839 \times 10^{33}$ erg/s
Parsec (pc)	$3.26 \times$ light year
Light Year (ly)	$9.4605284 \times 10^{15}$ meters
Parsec (pc)	$3.08568025 \times 10^{16}$ meters
Astronomical Unit (AU)	$149.60 \times 10^9$ m
pi ( $\pi$ )	3.14159265
Speed of light (c) <sub>in vacuum</sub>	$\sim 3.00 \times 10^8$ m/s



# Chapter 1

## Introduction

### 1.1 Introduction

**Galaxies** are large collections of billions of stars, gas and interstellar dust, orbiting about a common center. Our home ‘Milky Way’ is one of them. There are probably more than  $1.7 \times 10^{11}$  galaxies in the observable Universe. The diameter of these galaxies ranges between 1 Kpc to 100 Kpc (Kilo parsecs). The typical separation between galaxies is of the order of Mpc (Megaparsecs). Intergalactic space (the space between galaxies) is filled with a tenuous gas of average density less than one atom per cubic meter. The majority of galaxies are organized into a hierarchy of associations called clusters, which, in turn, can form larger groups called superclusters. These larger structures are generally arranged into sheets and filaments, which surround immense voids in the Universe. The luminosity of the galaxies are in the range of ( $\sim 10^6 L_{\odot}$  to  $\sim 10^{12} L_{\odot}$ ). It is usually measured in solar luminosity,  $L_{\odot}$ .

Star formation is an ongoing processes in the galaxies in which lot of dust and gas is available. The new generation of stars are born out of gas that condenses within regions of giant molecular clouds. These stars are formed in groups called star clusters and in isolation, as well. During various stages of its evolution,

a star returns much of its gas and processed higher elements (which are called metals) back into the interstellar medium. The interstellar medium, enriched in higher elements acts as source for formation of next generation of stars. Thus, galaxies can be thought of as systems that turn gas into stars and back again.

When we look at a galaxy, the light we see comes from two sources. First, we see integrated light from its billions of stars. Since most galaxies are so far away, we could not resolve individual stars but what we see is just the combined diffuse light of all the stars in the galaxy. Second, we see the light emitted by gas which is ionized by hot, luminous stars. These glowing gas clouds mark the sites of newly born stars, they often look like beads stringing the arms of spiral galaxies. The light from both stars and gas is dimmed to some extent by dust within the interstellar medium of the galaxy. Typical galaxies range from dwarfs with as few as ten million ( $10^7$ ) stars up to giants having hundred trillion ( $10^{14}$ ) stars. Galaxies radiate a continuous spectrum of electromagnetic wave, right from high energy Gamma rays to low energy millimeter waves. There are many different types of galaxies, the most simple criterion for classifying galaxies is their appearance. These types of galaxies not only appear different in their shape but they have different evolutionary histories and different properties as well. The three basic category of galaxies are elliptical, spiral, and irregular. These categories are further classified into subclasses, often illustrated using a Hubble tuning fork diagram.(Fig. 1.1)

This thesis deals with Wolf-Rayet Galaxies which are basically a subset of starburst galaxies. These Wolf-Rayet features are found in variety of morphologies, like spiral, irregular galaxies, low-mass blue compact dwarf (BCDs), Ultra-luminous Infrared Galaxies (ULIRGs), interacting galaxies and some time in active galactic nuclei also. The star formation rate and history in each type of galaxies are also different. Hence, The star formation rate, metallicity and other physical properties are strongly depend upon their morphology. So, it is necessary to know about to have good understanding about the all types of

galaxies and its properties since the Wolf-Rayet galaxies also existing in all types of galaxies.

### 1.1.1 Types of Galaxies

**Elliptical Galaxies:** Elliptical galaxies are devoid of gas and dust. They have very little interstellar gas and dust from which next generation of stars can form. Hence, at present very little star formation occurs in these galaxies. Most of the stars in these galaxies are old and red in colour. They have little or no global angular momentum. They are supported by anisotropic velocity distribution of the stars. Stars in these galaxies orbit the center in different directions and there is no pattern of orderly rotation. Based on their apparent flattening they are subdivided into E0, E1, E2,...and E7, with E0s as the spheroidal systems and E7s being the most flattened systems. The Hubble classification scheme uses the apparent ellipticity, so basically it refers to the projection of the galaxy's shape on to the celestial sphere, and not to its actual shape.

**Spiral Galaxies:** These galaxies are most common in the nearby Universe. Spiral galaxies have a central nucleus, a bright bulge and long spiral arms winding toward a bright bulge/nucleus at the center. Some spiral galaxies have a bright line, or bar, running through them. These are called "barred spiral galaxies". The spiral galaxies can be called as "face-on spiral" or "edge-on spiral", depending on their orientation with respect to the line of sight. The arms of spiral galaxies have lots of gas and dust, and they are the sites of ongoing star formation. Very little star formation goes on in the bulge. The bulge of a spiral galaxy is composed primarily of old, red stars. About 77% of the observed galaxies in the universe are spiral galaxies. Our own galaxy, the Milky Way, is a typical spiral galaxy. Spiral galaxies are mostly found in low-density regions and are rare in the centers of galaxy clusters.

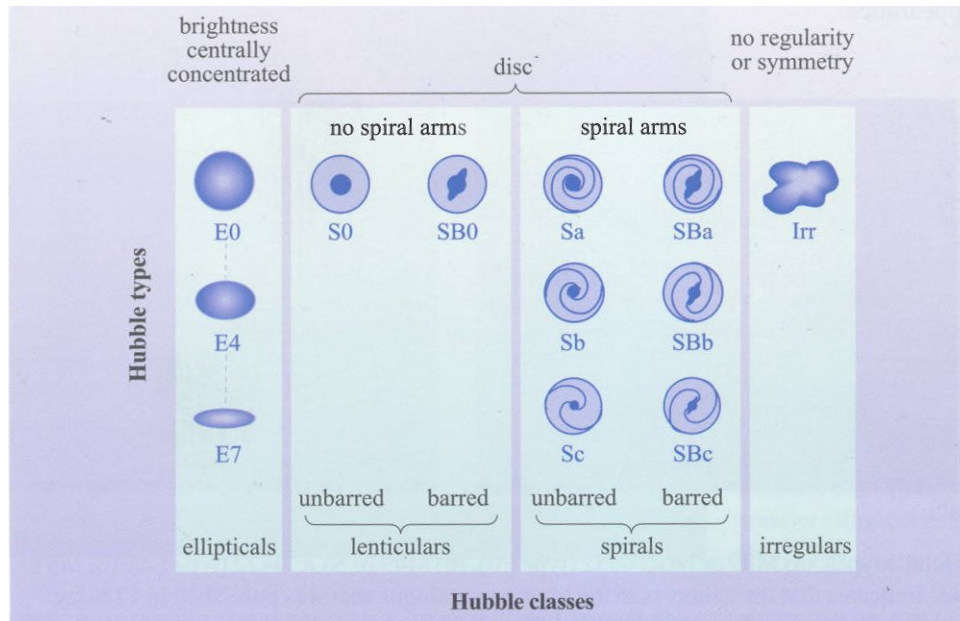


FIGURE 1.1: Hubble classification of galaxies (Mark & Robert 2003)

Among the spiral galaxies there are variation in the size of bulges, tightness of the spiral arms, number density of the star forming regions etc. Some spiral galaxies have arms that are wound tightly, while other galaxies have very loosely-wound arms. Spiral galaxies are further classified by how tightly their spiral arms are wound. A galaxy with very tightly wound arm and bigger bulge is called a “type a” galaxy. A “type b” galaxy has more loosely wound arms and “type c” galaxy has very loosely wound arms, they have smaller central bulge. The spiral arms are sites of ongoing star formation and are brighter than the surrounding disk because of the young, hot OB stars that inhabit them.)

**Irregular Galaxies:** Approximately 3% of the observed galaxies cannot be classified as either elliptical or spirals. These galaxies have little symmetry in their structure and are termed as irregular galaxies. Many of them are the results of galaxy collisions or near misses. Irregular galaxies also contain abundant amount of gas and dust. Irregular galaxies are usually found in groups or clusters, where collisions and near-misses between galaxies are common. In a few irregular galaxies, we can not even find out why they look so strange. Irregular galaxies are denoted by the letters Irr. Irregular galaxies are denoted by the letters

Irr. Again there are different classification of irregular galaxies. An Irr-I is an irregular galaxy that features some structure but not enough to place it clearly into the Hubble sequence. These are having like asymmetric objects with no spiral arms, but with many O and B stars. An Irr-II is an irregular galaxy that does not appear to feature any structure that can place it into the Hubble sequence. Asymmetric objects where the galaxy is more smooth with frequent dust lanes. A third classification of irregular galaxies are the dwarf irregulars, labelled as dI or dIrrs. This type of galaxy is now thought to be important to understand the overall evolution of galaxies, as they tend to have a low level of metallicity and relatively high levels of gas, and are thought to be similar to the earliest galaxies that populated the Universe. Apart from the three main classes discussed above, there are few more categories based on some specific properties of these galaxies, they are listed below.

**Lenticular Galaxies:** The galaxies which are populated in between ellipticals and spirals in the Hubble tuning fork diagram are known as Lenticular galaxies and also known as SO galaxies. These can be defined as galaxies with prominent disk but without any spiral structure. From their appearance and their stellar contents they look more like ellipticals rather than spirals. Because of this reason this is often misclassified.

**Blue compact galaxies (BCGs):** These galaxies are often low mass, low metallicity, dust-free objects. Because they are dust-free and contain a large number of hot, young stars, they are often blue in optical and ultraviolet colours. It was initially thought that BCGs were genuinely young galaxies in the process of forming their first generation of stars, thus explaining their low metal content. However old stellar populations have been found in most BCGs and it is thought that efficient mixing may explain the apparent lack of dust and metals. Most BCGs show signs of their recent mergers and (or) close interactions.

**Ultra-luminous Infrared Galaxies (ULIRGs):** These galaxies are generally extremely dusty objects. The ultraviolet radiation produced by the obscured

star-formation is absorbed by the dust and reradiated in the infrared spectrum at wavelengths of around 100 micron. This explains the extreme red colours associated with ULIRGs. It is not known for sure that the UV radiation is produced purely by star-formation and some astronomers believe ULIRGs to be powered (at least in part) by active galactic nuclei (AGN). X-ray observations of many ULIRGs that penetrate the dust suggest that many starburst are double cored systems, lending support to the hypothesis that ULIRGs are powered by star-formation triggered by major mergers. Well-studied ULIRGs include Arp 220.

**Dwarf Galaxies:** These galaxies have smaller physical sizes typically and lower luminosities. They can be further divided into dwarf ellipticals (dEs), dwarf spheroidals (dSphs) with very low surface brightness and dwarf irregulars (dIrrs). It is still unclear how the different classes, in particular, the dwarf spheroidals, form. Usually, physical size ( $\sim 0.1\text{kpc} - 10\text{kpc}$ ), which defines a dwarf  $\rightarrow$  giant sequence of galaxies

**Peculiar galaxies:** These type of galaxies are found in 5%-10%. This category includes the **starbursting** galaxies and powerful active galactic nuclei (**AGNs**). **Active Galactic Nuclei (AGN):** These are having very energetic central regions, due to either the presence of a black hole or star formation activity (Verma et al 2005) at the core of the galaxy. Three main types of AGN are quasars, which are very compact objects; Seyfert galaxies, characterized by fluctuations in brightness at their cores; and radio galaxies, which emit massive jets of gas powered by black holes at their cores. Generally, intensity variations have long been recognized as a defining characteristic of active galactic nuclei (AGNs). Variability is a powerful tool for probing AGN geometry and physical properties such as the black hole mass, size and bulk motions of the outflows in their innermost regions that are well beyond the current imaging capabilities of telescopes in any part of the electromagnetic spectrum (e.g. Urry & Padovani 1995; Wagner & Witzel 1995; Xie et al. 2001). The variations can be particularly

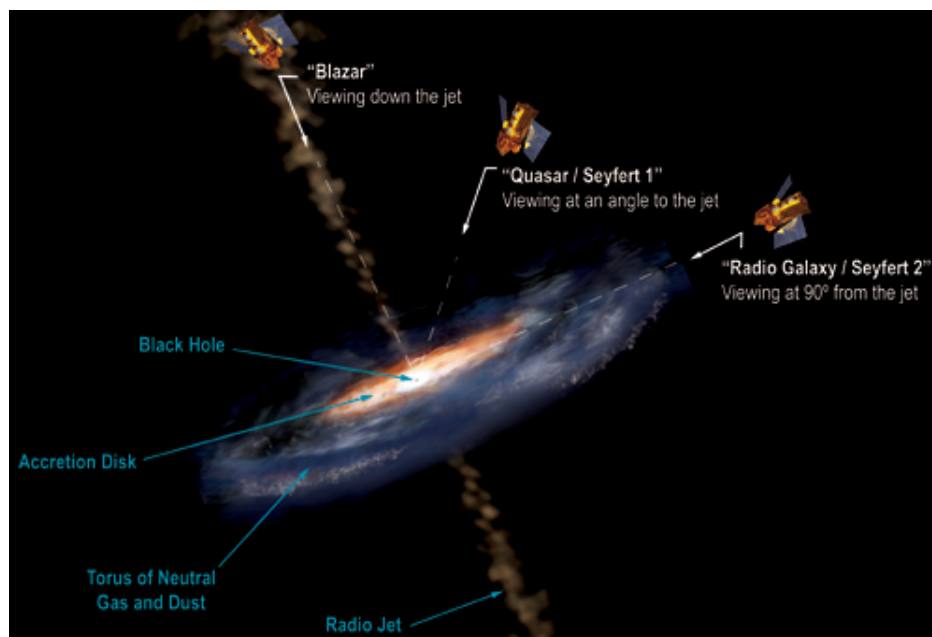


FIGURE 1.2: Illustrates the Unified Model of AGN classification with respect to viewing from different angle line of sight.(Arrow marked).

violent for those AGNs whose flux is dominated by relativistic jets of non-thermal radiation broadly pointing in our direction (e.g. Begelman, Blandford & Rees 1984). Intensities of such AGNs, called blazars, are known to vary across the entire electromagnetic spectrum and time-scales from minutes to years have been observed. For instance, in the soft X-ray band, several TeV-emitting blazars have been found to vary on a characteristic time-scale of  $\sim 1$  d, with the flares having substructures on shorter time-scales of  $\sim 10^4$  s (e.g. Kataoka et al. 2001; Tanihata et al. 2001). In the optical regime, there have been many detections of intranight optical variability (INOV), or optical microvariability, following the pioneering work of Carini, Miller & Goodrich (1990), who first used CCD detectors as multi-object photometers for this purpose. The shortest time-scale found for essentially all INOV events is around 1 h, with an amplitude of a few per cent (e.g. Xie et al. 2001; Romero et al. 2002; Stalin et al. 2004a). Such rapid continuum variability of blazars is usually explained by invoking relativistic jets (e.g. Marscher 1996; Schlickeiser 1996; Wiita 2006) (Gopal-krishna, including **Chrispin Karthick et al 2011**).

**Quasar:** (Fig. 1.2) The word quasar is short for quasi-stellar radio objects. Also known as QSO. Quasars were discovered by Allan R Sandage in 1964. It is a distant star-sized energy source in space with an excess of ultraviolet radiation. Some of these QSO's gives off large amounts of radiation, including radio waves and X-rays (but some are radio-quiet). As shown in the Fig. 1.2, these are all classification of the AGN as viewing from the different line of sight.

**Blazar:** (Fig. 1.2) This is an extreme quasar. Blazars are subset of active galactic nuclei, with relativistic jets oriented close to the line of sight with the observer. The special jet orientation explains the general peculiar characteristics: high observed luminosity, very rapid variations, high polarization (when compared with non-blazar quasars), and the apparent superluminal motions detected along the first few parsecs of the jets in most blazars. “**TeV Blazars**” are known as for their high energy (teraelectron-volt range) gamma-ray emission.

**Seyfert galaxy:** (Fig. 1.2) This is an active spiral galaxy. Its nucleus (center) has bright emission lines, including visible wavelengths. The brightness varies over relatively short time periods (less than a year). They may have massive black holes at their centers.

As mentioned above, though there are many types of galaxies, the three most common types of galaxies are ellipticals, spirals and irregulars. By going through their properties and spectral type, we can understand the major difference between them. And most of the galaxies studied in the present work are spirals and irregulars. Generally all these **galaxies can also be easily classified from their spectral information**. The basic trends in galaxy spectra with Hubble type are illustrated in Fig. 1.3, which shows examples of integrated spectra for E, Sa, Sc, and irregular galaxies. When progressing along this sequence, several changes in the spectrum are apparent: a broad rise in the blue continuum, a gradual change in the composite stellar absorption spectrum from K-giant dominated to A-star dominated, and a dramatic increase in the strengths of the nebular emission lines, especially  $H\alpha$ . Although the integrated spectra

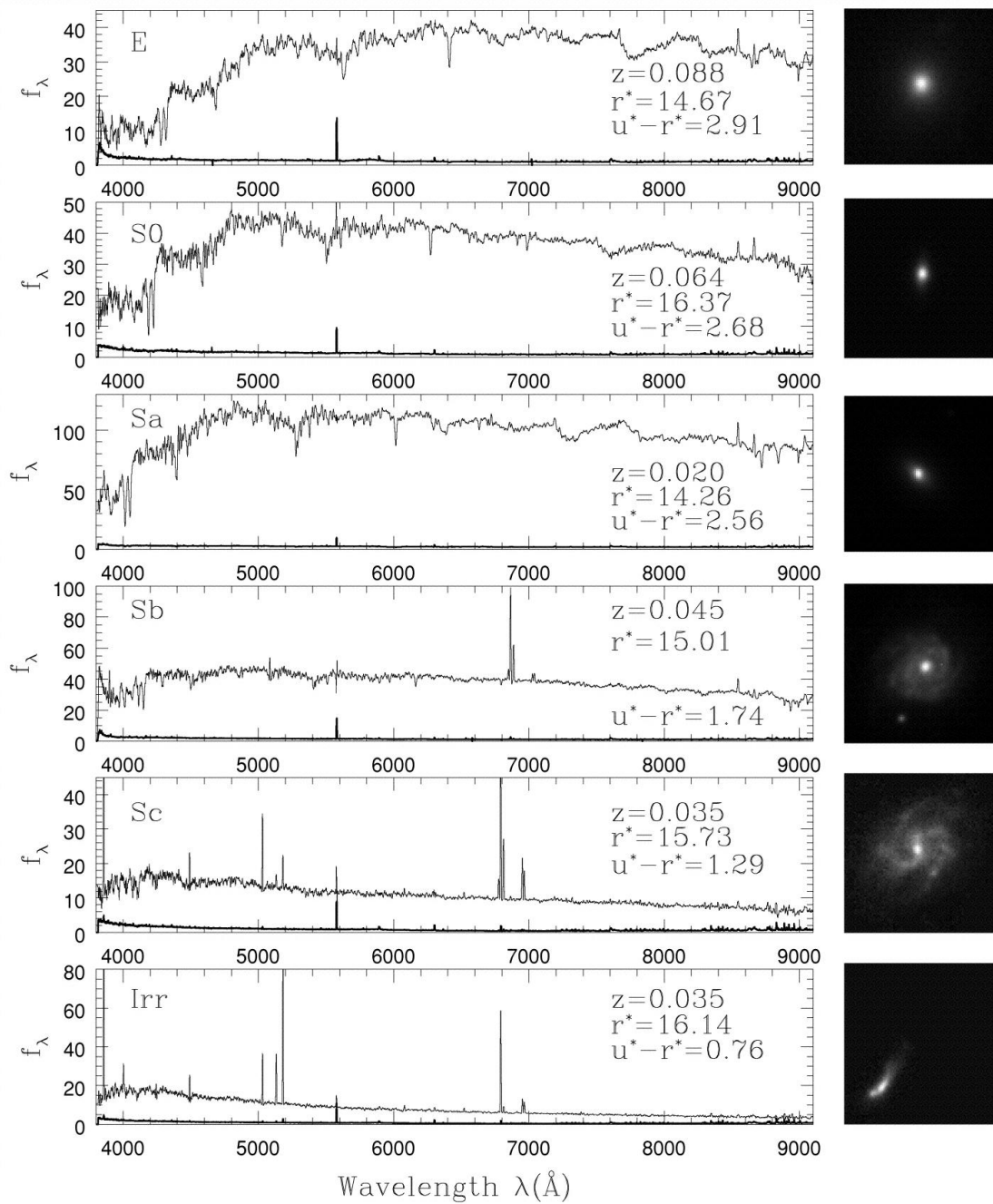


FIGURE 1.3: Spectrum of different types of Galaxies (Image credit: Srateva et al 2001;)

contain contributions from the full range of stellar spectral types and luminosities, it is easy to show that the dominant contributors at visible wavelengths are intermediate-type main sequence stars (A to early F) and G-K giants. As a result, the integrated colors and spectra of normal galaxies fall on a relatively tight sequence, with the spectrum of any given object dictated by the ratio of early- to late-type stars or, alternatively, by the ratio of young ( $< 1$  Gyr) to old (3-15 Gyr) stars. This makes it possible to use the observed colors to estimate the fraction of young stars and the mean SFR over the past  $10^8 - 10^9$  years (Kennicutt 1998). In similar way, Wolf Rayet galaxy also differs from other spectra by showing WR bumps as shown in (Fig. 1.5). Thus this spectral information plays an important role while classifying the galaxies.

### 1.1.2 Starburst Galaxy

A starburst galaxy is a galaxy in the process of an exceptionally high rate of star formation is going on compared to the usual star formation rate seen in most galaxies. The precise definition of a “starburst galaxy” is not yet defined. Galaxies are often observed to have a burst of star formation after a collision or close encounter between two galaxies. The rate of star formation in this are so great for a galaxy undergoing a starburst that, if the rate was sustained, the gas reservoirs from which stars are formed would be used up on timescales much shorter than the dynamical lifetime of the galaxy. For this reason, it is presumed that starbursts are temporary. These type of starburst phenomenon in galaxies was first described by Sargent & Searle (1970).

Currently, the most widely accepted theory is a collision or a close encounter with another galaxy that starts a chain reaction. The impact of such a collision produces shock waves throughout the galaxy that push on vast clouds of interstellar dust and gas that are present. These shock waves in turn cause the clouds to collapse and produce short-lived, massive stars. These Young, hot stars ionize

the gas (mainly hydrogen) around them creating H II regions. Groups of very hot stars are known as OB associations. The stars that form from this collision quickly use up their nuclear fuel and explode in a supernova (an extremely bright new star). This explosion produces yet more shock waves and consequently more star formations. The formation of a starburst galaxy ends when its giant clouds of gas are used up or pushed too far away due to the explosions. This rapid rate of supernova explosions in starburst galaxies produces expanding bubbles of multimillion degree gas. When the starburst is sufficiently intense, it can create a superbubble so hot and energetic that it expands out of the galaxy in what is called a superwind. Superwinds are thought to contain the carbon, nitrogen, oxygen, iron and other heavy elements dispersed by supernovas and spread these elements throughout the space between galaxies. Observationally, the overwhelming signature of starburst galaxies is intense emission in the far-infrared, caused by the ultraviolet emitted by numerous hot, young stars being absorbed by dust and re emitted at longer wavelengths.

These type of galaxies are seems to be quite rare in our local universe, and are more common further away indicating that there were more of them billions of years ago. All galaxies were closer together then, and therefore more likely to be influenced by each other's gravity. More frequent encounters produced more starbursts as galactic forms evolved with the expanding universe. Although not all Starbursts may be explained by galaxy collisions, many are clearly stimulated by collisions or mergers of gasrich galaxies.

### **1.1.3 AGN-Starburst Connection**

While discussing about the starburst galaxies and its activities, it is always better to have a glimpse of ideas about AGN. The issue of a Starburst-AGN connection in local and distant galaxies is relevant again for understanding galaxy formation and evolution, the star formation and metal enrichment history of the universe,

the origin of the extragalactic background at low and high energies, and the origin of nuclear activity in galaxies. While some investigations have found that the incidence of AGN is higher in interacting galaxies than in isolated galaxies (eg., Veilleux et al., 1995), others have found a deficiency of AGN in advanced mergers and strongly interacting systems (eg., Bushouse, 1986). It is unclear at this stage what effect a merger has on AGN activity. Nuclear (or circumnuclear) gas is often ionized at some level in most nearby galaxies (in particular, disk galaxies). It is known that there are two fundamental types of nuclear activities; (1) The nuclear starburst activity and (2) The nonthermal nuclear activity. Nuclear gas in the former class of galaxies is photoionized by massive OB stars while in the latter class of galaxies is photoionized by nonthermal ionizing continuum emission from the central engine of active galactic nuclei (AGN) (e.g., Rees 1984).

According to the recent extensive spectroscopic study of nuclear regions of 486 nearby galaxies promoted by Ho, Filippenko, & Sargent (1997), both types of galactic nuclei share approximately 40%, respectively, if we include objects with low emission-line luminosity or low activity. However, typical luminous starburst nuclei share approximately several percent of nearby galaxies (e.g., Balzano 1983). Also, Seyfert nuclei, typical AGNs in nearby universe, are found in approximately 10 percent of nearby galaxies (Ho et al. 1997). Therefore, roughly speaking,  $\sim 10\%$  of galactic nuclei experience the nuclear starburst activity,  $\sim 10\%$  of galactic nuclei experience the nonthermal activity, and the remaining  $\sim 80\%$  of galactic nuclei show little evidence for significantly high level of such activities (i.e., nearly normal galactic nuclei).

## 1.2 Wolf-Rayet Definition

Wolf-Rayet name comes from two French astronomers Charles Wolf and Georges Rayet who discovered a rare class of star, using the 0.4 metre Foucault telescope

in Paris in 1867. Wolf-Rayet features were first found in the dwarf emission galaxy He2-10 (Allen, Wright, & Goss, 1976). As more such features were discovered in galaxies, Osterbrock & Cohen (1982) defined Wolf-Rayet (W-R) galaxies as those galaxies which contain broad stellar emission lines in their spectra and therefore contain large numbers of W-R stars. The large numbers of W-R stars are thought to be a result of present or very recent star formation.

### 1.2.1 Wolf-Rayet Star

Before discussing about the Wolf Rayet galaxies, it is necessary to have a good understanding about the Wolf Rayet stars also. Wolf-Rayet stars (often referred to as WR stars) are evolved, massive stars (over 20 solar masses). Wolf-Rayet stars are characterized by broad emission lines. W-R stars, are subdivided into 3 broad spectroscopic classes based on the emission lines present in their spectra: WN (helium and nitrogen lines), WC (helium and carbon) and WO (helium, carbon, and oxygen). These spectra classes are further divided into subclasses on the basis of line ratios, yielding a classification by ionization. The WN stars which exhibit spectra showing emission from high ionization species (e.g., He II, N V, O VI) are designated WN2. Those showing emission from low ionization species (e.g., He I, N III) are classified as WN9, although recently the W-R spectral classification has been extended to WN11. Similarly, WC stars showing emission from high ionization species (e.g., He II, C IV, O VI), are designated WC4 while those exhibiting the lowest ionization (e.g., He I, C II) are designated WC9. In the literature there is also a tendency to refer to WN stars of classes 2 to 5 as early type (WNE) and classes 6 to 9 as late type (WNL). Similarly WC4-6 stars are designated as WCE, while WC7-9 stars are designated as WCL. Although there are important exceptions, WNE stars generally show no evidence for H emission while H emission is present in WNL stars.

Population I W-R stars are generally located in the spiral arms of our galaxy near H II regions. With masses ranging from 5 to 60 times that of our own Sun,

they are believed to be descended from O stars. Surface temperatures may range from 25,000 K to 100,000 K, and thus W-R stars are significantly hotter than the Sun. Significant mass-loss, which may cause the star to lose over half its mass during its lifetime, is one of the defining characteristics of W-R stars. This mass loss occurs via stellar winds and strongly affects the stellar evolution of a star. It is believed to be driven by radiation pressure. Approximately 220 W-R stars have been found in the Milky Way. All stars more massive than  $25 M_{\odot}$  will pass through a W-R phase. In addition, Wolf-Rayet stars and their progenitors have an important influence on the chemical evolution, energetics, and dynamics of the inter stellar medium, or ISM.

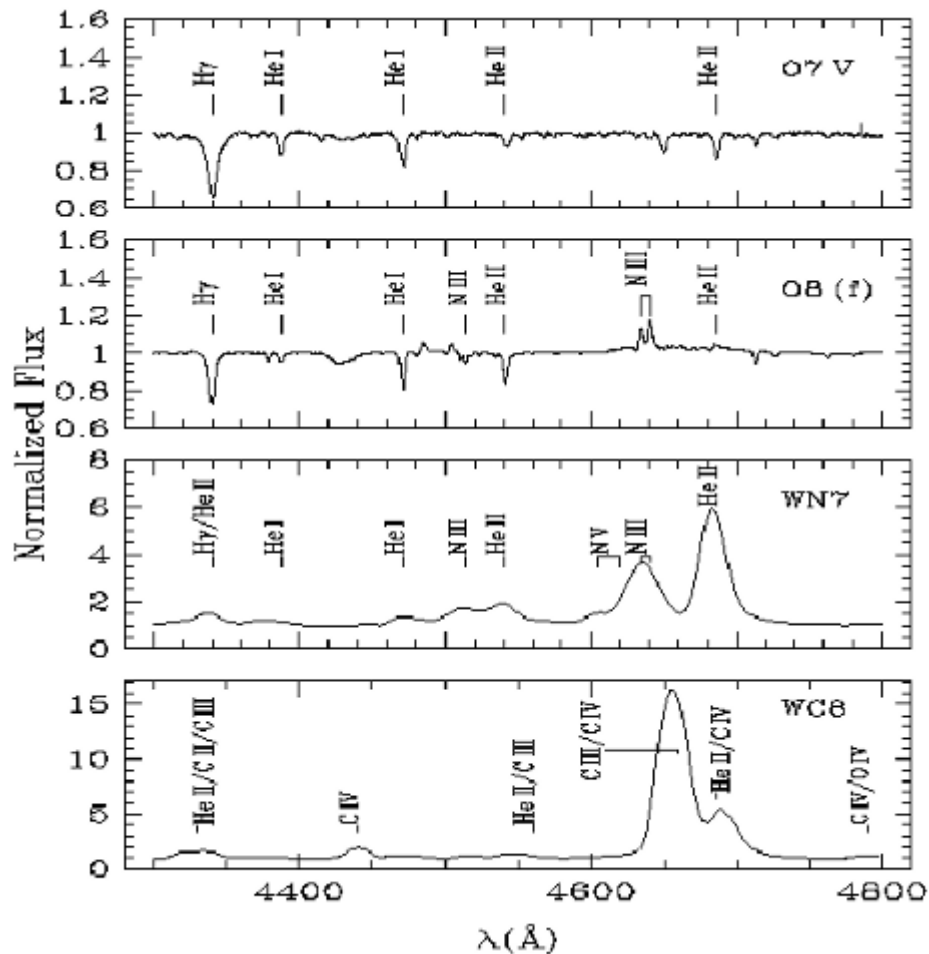


FIGURE 1.4: Evolution of WR star

WR stars are very windy and are losing their mass rapidly by means of a

---

very strong stellar wind, with speeds up to 2000 km/s which is much greater than our sun. WR star is surrounded by an atmosphere” of gas that is comparable in size to the star itself. In this way, when we observe this, we are really seeing the ionized gas surrounding the star. This gas is so hot it emits visible light, along with a variety of other kinds of photons (radiation) ranging from less energetic radio waves and microwaves to more energetic ultraviolet light and X rays. WR stars emit so much material because of the occasional upwelling of heavier elements fused inside the core, including carbon and oxygen. These heavier elements interrupt the energy flowing outward from the star by absorbing it. Eventually, this causes a tremendous outward pressure that takes the form of a powerful stellar wind blowing off the star. A typical WR star can lose a mass equivalent to that of the Earth in a year. Because WR stars burn so brightly and they have very short life spans. A typical WR life span is just a few million years, compared to the billions years or so for more calmer, more stable stars such as our Sun (which is about midway through its 10 billion year life span). When a WR star dies, it often undergoes a supernova detonation. Some of these supernovae are sufficiently energetic to classify as a hypernova. And some of these hypernovae are accompanied by a gamma-ray burst as the core undergoes an uneven gravitational collapse into a black hole, an object whose gravitational pull within a certain distance is so powerful nothing, not even light, can escape from that. Wolf-Rayet stars have been found in very different extragalactic environments: Giant H II regions, Blue Compact galaxies, generic emission line galaxies, IRAS galaxies, Seyfert galaxies in general, always in regions experiencing a strong episode of massive star formation (Crowther 2007).

## 1.2.2 Wolf-Rayet Galaxies

Discussing about the Wolf-Rayet galaxies, in short it is written as WR galaxies. These are a subset of starbursts galaxies. Wolf-Rayet stars (WR) are the descendants of the most massive stars. Although they live during a short time (Maeder & Conti 1994) these stars have been detected in young stellar systems, such as extragalactic H II regions (Kunth & Schild 1986) and the so-called WR galaxies (Conti 1991; Schaerer et al. 1999b). They are recognized by the presence of broad stellar emission lines at optical wavelengths, mainly at  $4680 \text{ \AA}$  (known as the blue WR bump) and at  $5808 \text{ \AA}$  (red WR bump) as shown in Fig. 1.5. WR galaxies are found among a large variety of morphological types as mentioned in introduction as well.

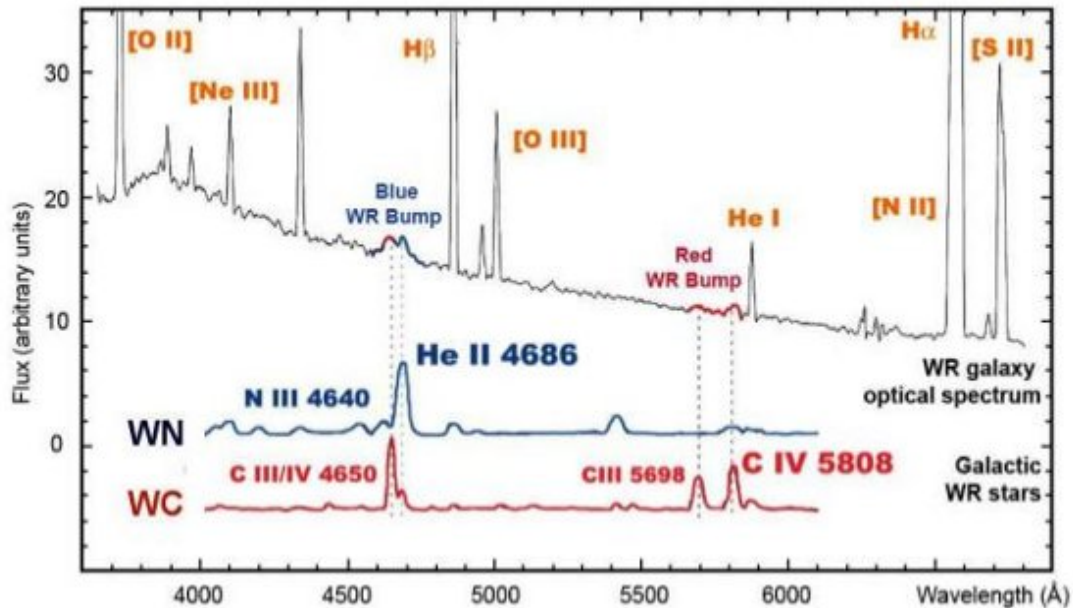


FIGURE 1.5: Observational evidence of the presence of hot and massive “Wolf-Rayet” stars in a metal-rich H II region (designated “-014+081”) in the spiral galaxy NGC 4254, a member of the Virgo cluster of galaxies at a distance of about 50 million light-years. Comparison spectra of two types of Wolf-Rayet stars (WC and WN) in the Milky Way galaxy are shown. The characteristic spectral features of ionized helium (He II) and double and triple ionized carbon (C III, C IV) are identical. (Image credit: Press release of ESO image Id: eso0223c, 15/02; & Lopez Sanchez Thesis 2006)

The blue bump is a blend of N V  $\lambda\lambda 4604, 4620$ , N III  $\lambda\lambda 4634, 4641$ , C III/IV  $\lambda\lambda 4650, 4658$  and He II  $\lambda 4686$  lines, that are produced in WR stars of the nitrogen (WN) and carbon (WC) sequences. In contrast, the red bump is formed only by C IV  $\lambda 5808$  and it is mainly produced by WC stars. The detection of these features in the integrated spectrum of a stellar system provides a powerful tool to date the onset of the burst, and it constitutes the best direct measure of the upper end of the initial mass function (IMF). Thus, if WR features are found in the spectra of star forming systems, stars more massive than  $M_{WR}$ , where  $M_{WR} \sim 25 M_{\odot}$  for solar metallicity, must be formed in the burst (Pindao et al 2002).

**Catalogues:** Kunth & Joubert (1985) searched for W-R emission in a sample of blue emission line galaxies. They found a positive detection in one galaxy and suspected W-R emission in 14 others and suggested that W-R stars are preferentially detected in low redshift galaxies. Following on from this study, Conti (1991) presented a catalogue of W-R galaxies, showing that W-R galaxies can be easily distinguished by their broad He II 4686 emission feature, or in some cases a broad line at 4640 Å due to [N III]. High resolution long-slit observations of a sample of Wolf-Rayet galaxies were carried out recently by Guseva, Izotov, & Thuan (2000). Nearly all the galaxies in their sample show broad W-R emission consisting of an unresolved blend of N III  $\lambda 4640$ , C III  $\lambda 4650$ , [Fe III]  $\lambda 4658$ , and He II 4686 emission lines. They also found weaker W-R emission lines N III  $\lambda 4512$  and Si III  $\lambda 4565$  in some galaxies. And another list of galaxies made by Brinchman et al. 2008, through SDSS survey where they found a total of 570 galaxies with significant Wolf-Rayet (WR) features and a further 1115 potential candidates too. For the present thesis the sample of galaxies is taken from the list of (D. Schaerer et al. 1999). In this list there are 139 known galaxies and 28 suspected galaxies. Among these, 57 objects show both broad He II 4686 Å and C IV 5808 Å features. These features represent presence of WN and WC stars respectively as we discussed. These objects are important to study the early phases of starbursts and to determine the burst properties like age, duration of burst and SFR (Star formation Rate) etc.

## 1.3 Star Forming Regions in a Galaxy

### 1.3.1 H II regions

There are several factors factors which initiate star burst in galaxies, such as **Nearby supernovae explosions**, **Neighboring episodes of star formation**(Massive O or B type), or **Collisions between two or more giant molecular clouds** (**Interaction and Merging of galaxies**), **Spiral arm shock in the galaxy** and also due to **Agn-Starburst activity**. These events cause density enhancements and temperature variations inside the cloud, leading to the gravitational accretion of matter into a massive body. Over time, the increasing temperature and pressure of the pre-stellar core becomes sufficient to initiate nuclear fusion, and a star is born. Regions of star formation are very bright because massive, newborn stars typically release a large amount of energy, particularly in the UV regime. This high-energy radiation illuminates the surrounding gas cloud to produce a glowing cloud of gas called an H II region. These bright beacons are targets for UV, optical, and infrared spectroscopy. Observations of H II region characteristics are extremely useful in studies of star formation.

These H II regions is nothing but the evidence of star forming regions. The spectrum of a Starburst Galaxy (Fig:1.6) looks much like that of an ionized hydrogen region because of the light from these galaxies is dominated by giant H II regions ionized by recently formed, massive, hot stars. Abundances are relatively easy to measure in star-forming dwarf galaxies because they contain gas clouds in which large numbers of hot stars are embedded. Their spectra are dominated by nebular emission lines similar to those of high-excitation giant H II regions in late type spiral galaxies. What is observed in the optical are narrow emission lines superimposed on a blue stellar continuum. They are identified as helium and hydrogen recombination lines and several forbidden lines.(Fig:1.6)

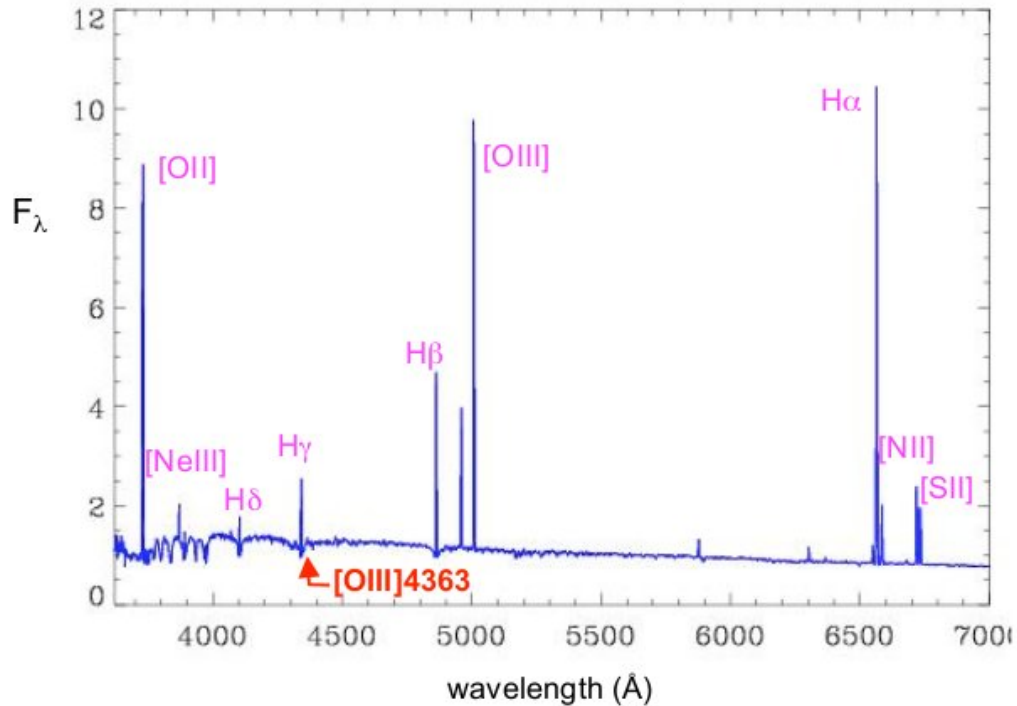


FIGURE 1.6: A typical H II Regions Spectra

### 1.3.2 Physical processes in H II region

When a newly born massive star process starts on, it begins to ionize the surrounding material. Stellar photons with energies greater than the ionization potential of hydrogen (13.6 eV) ionize hydrogen and other elements. The excess energy of each absorbed photon goes into kinetic energy of the ejected (thermal) electron. Collisions between electrons, and between electrons and ions, distribute the energy and maintain a Maxwellian velocity distribution with a temperature in the range from 5000 to 10000 K. Collisions between thermal electrons and ions excite the low-lying energy levels of the ions. Downwards radiation transitions from these excited levels have very small transition probabilities, but at the densities of these nebulae, collisional de-excitation is even less probable and hence, almost every excitation leads to emission of a photon, and the nebula emits a forbidden-line spectrum. Thermal electrons are recaptured by the ions,

and the degree of ionization at each point in the nebula is fixed by the equilibrium between photoionization and recombination.

In the recombination processes, recaptures occur to excited levels, and the resulting cascade downwards gives the recombination line spectrum. The star cannot ionize an infinitely large amount of surrounding gas. The volume of gas that the star can ionize is limited to that volume in which the total recombination rate is just equal to the rate at which the star emits ionizing photons. This volume of ionized gas is characterized by the Strömngren radius.

### 1.3.3 Formation of Forbidden lines

Forbidden line is an emission line in a spectrum that is emitted only by a low-density gas, as in interstellar regions and nebulae. Such a line is said to be forbidden because it does not occur under normal conditions on Earth, where gases are denser. A forbidden line arises when an electron in an excited (energized) atom jumps from a metastable state to a lower energy level. Under normal (Earth) circumstances, when particle densities are higher (greater than about  $10^8$  per  $cm^3$ ), such an electron would almost immediately be knocked out of its metastable state by collision and not be given time to emit a photon. However, in the low densities of interstellar space and the regions around hot stars, collisions are extremely rare and there is time for the spontaneous decay to occur.

Consequently, when ions such as  $O^+$ ,  $O^{2+}$  (singly and doubly ionized oxygen), or  $N^+$  (singly ionized nitrogen) go into metastable states by allowed transitions from higher states, they remain there undisturbed until they radiate spontaneously. A large fraction of the more highly excited ions eventually drop into these states and, in a nebular environment, practically every ion goes from them to the ground state by forbidden radiation. Forbidden lines are denoted by enclosing them in brackets. The strongest are two lines of doubly ionized oxygen [O III] at 4959 and 5007 Å. Besides forbidden lines of ionized oxygen, others of

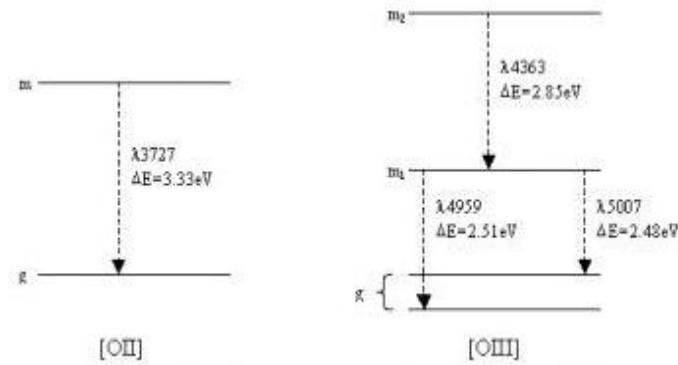


FIGURE 1.7: Different optical energy level transitions for [O II] and [O III]. “g” is the ground state and “m” is the metastable state(s). Splitting not to scale.

neon, nitrogen, and other relatively abundant elements are seen making up the light of nebulae, as well as the ordinary, permitted lines of hydrogen and helium (Further reading Osterbrock, 2006).

### 1.3.4 Solar abundances

These above mentioned Forbidden lines can be used to obtain relative abundances of two elements or elemental abundances relative to hydrogen . The abundance ratio of two ions can be obtained from the observed intensity ratio of lines emitted by these ions. To derive ionic abundances relative to hydrogen, one needs the  $H^+$  density, which can be obtained from hydrogen recombination lines or radio continuum measurements. The total abundance of a given element relative to hydrogen is given by the sum of abundances of all its ions (Fig. 1.8).

In Fig. 1.8 which represents the Solar System abundances against atomic number  $z$  for elements in the range  $1 \leq z \leq 83$ . These are observed in sun’s photosphere. The general trend is a steady decline from the very high abundances of the lightest elements, H and He, to the low abundances of the elements with  $z > 30$ , with a total range of  $\sim 12$  dex. Structure in the curve supports the paradigm that the heavy elements present in the Solar abundances are the products of nucleosynthesis within previous generations of stars The

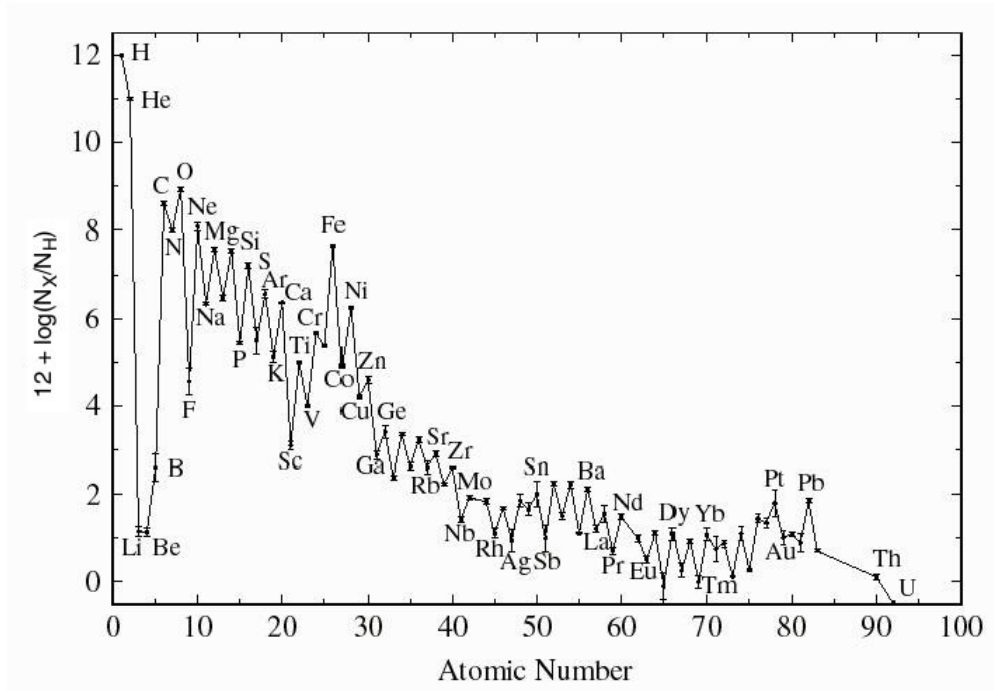


FIGURE 1.8: Plot of mean abundances by number in the Solar scale against atomic number

trough at  $z$ -values 3-5 (lithium group) reflects the intrinsic fragility of these elements. Peaks occur for nuclei composed of integral numbers of  $\alpha$ -particles ( $^{12}\text{C}$ ,  $^{16}\text{O}$ ,  $^{20}\text{Ne}$ ,  $^{24}\text{Mg}$ ,  $^{28}\text{Si}$ , etc) and the prominent iron (Fe) peak centered at  $z = 26$  represents the build-up of elements at the end-point of exothermic nucleosynthesis.

Astrophysical abundances are traditionally expressed on a logarithmic scale relative to  $N_H = 10^{12}$ , as in Fig. 1.8 for element  $X$ ,

$$\log A(X) = 12 + \log\left(\frac{N_X}{N_H}\right) \quad (1.1)$$

The arbitrary constant 12 in Eq. 1.1 is merely a mathematical convenience, as the logarithmic abundance is then a positive number for even the rarest chemical elements (see Fig. 1.8) (D C B Whittet, Dust in galactic environment). For further list of solar abundances is given in App. B

### 1.3.5 Metallicity

In terms of astronomy, "metals" are any elements other than hydrogen and helium. Metallicity is described as the overall metal abundance of a region as a ratio of metal to hydrogen. There are many notations to represent the metallicities:  $Z_i$ ,  $[Fe/H]$ ,  $\log(X/Y)$ ,  $12 + \log(Z_i/H)$ . Metals are found throughout the galaxies. They are synthesised in stars and liberated into the interstellar medium (ISM) when stars shed their outer gaseous envelopes towards the end of their lives, and in some cases also into the intergalactic medium (IGM) when the highest mass stars explode as supernovae. The amount of metals in the diffuse gas around galaxies also determines the rate at which it is able to cool and form stars. Metallicity is, therefore, one of the key physical properties of galaxies, and helps in understanding the processes that regulate the exchange of metals between stars, cold interstellar gas, and diffuse surrounding gas can help us understand the physical processes that govern galaxy evolution in general.

The metallicity of stars and gas in galaxies is known to correlate strongly with their luminosities, circular velocities and stellar masses (e.g. Lequeux et al. 1979; Garnett 2002; Tremonti et al. 2004; Gallazzi et al. 2005). However, the physical processes that drive these correlations are not yet fully understood. Mathews & Baker (1971) and Larson (1974) first suggested that interstellar gas can be driven out of galaxies by supernova explosions as galactic outflows. They predicted that galaxies of smaller mass have lower metal abundances because their lower escape velocities allow freshly enriched gas to be more efficiently removed. (Robert et al 2011). Generally, the expression for the metallicity is,

$$[X/H] = \log_{10} \left( \frac{N_x}{N_H} \right)_{star} - \log_{10} \left( \frac{N_x}{N_H} \right)_{sun} \quad (1.2)$$

Here X is any element other than hydrogen and Helium; In stars and as an general expression, the metallicity always explained with respect to the ratio

of iron to hydrogen i.e, if we replace the X as Fe in the above equation then, it becomes

$$[\text{Fe}/\text{H}] = \log_{10} \left( \frac{N_{\text{Fe}}}{N_{\text{H}}} \right)_{\text{star}} - \log_{10} \left( \frac{N_{\text{Fe}}}{N_{\text{H}}} \right)_{\text{sun}} \quad (1.3)$$

where  $N_{\text{Fe}}$  and  $N_{\text{H}}$  is the number of iron and hydrogen atoms per unit of volume respectively. In this the unit often used for metallicity is the "dex" which is a (now-deprecated) contraction of decimal exponent. By this formulation, stars with a higher metallicity than the Sun have a positive logarithmic value, while those with a lower metallicity than the Sun have a negative value. The logarithm is based on powers of ten: For example, if the metallicity  $[\text{Fe}/\text{H}] = -1$  then the abundance of heavy elements in the star is one tenth that found in the Sun; if  $[\text{Fe}/\text{H}] = +1$ , the heavy element abundance is 10 times the solar value. Measurements for thousands of stars have established that the range of values for  $[\text{Fe}/\text{H}]$  is from -4 (very metal-poor) to +1 (very metal-rich).

Now, in our context that is star forming regions(H II regions) , even though it contains a small number of oxygen atoms, the emission lines of ionized oxygen are among the strongest peaks found in an optical spectrum (see Fig. 1.8). The prominence of [O II] and [O III] emission makes oxygen a convenient source to determine a region's metallicity (Sec. 4.4). In general, mathematical models of metallicity are based on emission line observations of nearby H II regions where independent methods exist to determine metal abundance. Such analysis has led researchers to construct robust metallicity models that may be extended for use in the spectra of distant galaxies. The mathematical models of McGaugh (1991, 1994) and Kobulnicky (1999) are particularly useful to our research. These metallicity models provide a relationship between the observed spectral emission lines of oxygen and the metallicity of an H II region. This is a very convenient relationship because the spectral lines of oxygen are among the most intense in the spectra of star-forming regions. To understand this Oxygen dependent

metallicity equation, the same equation can be re-written with respect to oxygen as below,

$$[\text{O}/\text{H}] = \log_{10} \left( \frac{N_{\text{O}}}{N_{\text{H}}} \right)_{star} - \log_{10} \left( \frac{N_{\text{O}}}{N_{\text{H}}} \right)_{sun} \quad (1.4)$$

Thus from the above understanding of both the terms i.e, Oxygen abundances, Metallicity and its relation: Metallicity is estimated from the oxygen abundances from the relation  $Z = 0.02 * 10^{[\log(\text{O}/\text{H}) - \log(\text{O}/\text{H})_{\odot}]}$ , assuming  $12 + \log(\text{O}/\text{H})_{\odot} = 8.66$ , (Asplund et al. 2005).

## 1.4 Motivation

The morphological type of WR galaxies varies from the low-mass blue compact dwarf (BCD) irregular galaxies, to massive spirals and luminous merging galaxies. WR features are often found in starburst galaxies. The progenitors of the Wolf-Rayet stars are the most massive ( $M \gtrsim 25 M_{\odot}$ ), luminous ( $10^5$  to  $10^6 L_{\odot}$ ) and hot ( $\sim 50,000$  K) O stars, and they finalize their days exploding as type Ib/Ic supernovae (Meynet & Maeder 2005). Actually, the minimum stellar mass that an O star needs to reach the WR phase and its duration depends on the metallicity. In general, the WR phenomenon is short lived, it exists only for  $\leq 1$  Myr. Hence, the detection of WR features in the spectra of a galaxy constrains the properties of the star-formation processes. Because the first WR stars typically appear around 2 – 3 Myr after the starburst is initiated and disappear within some 5Myr (Meynet & Maeder 2005), their detection informs about both the youth and strength of the burst, offering the opportunity to study an approximately coeval sample of very young starbursts (Schaerer & Vacca 1998), but also to study the formation and impact of massive stars in starburst galaxies (Guseva et al. 2000; Fernandes et al. 2004; Buckalew et al. 2005; López-Sánchez & Esteban 2010a,b) and the role that interaction with or between dwarf galaxies and/or low

surface brightness objects plays in the triggering mechanism of the star-formation activity (López-Sánchez & Esteban 2008; López-Sánchez 2010). With the aim of getting a better understanding of the properties of these Wolf-Rayet (WR) galaxies, we have performed a detailed analysis of a sample of these objects using broad-band  $U, B, V, R, I$ , narrow-band  $H\alpha$  imaging and low-resolution optical spectroscopy.

### 1.4.1 Thesis Outline

A brief outline of the thesis is given below:

**Chapter1:** This chapter deals with the introduction of all basic concepts behind each problem taken in to thesis work. It also explains about the motivation of the present work.

**Chapter2:** This chapter deals with the description of telescopes, filter systems, detectors used for observations and data reduction techniques. *All these data reductions methods and commands are already well explained and published as a book through Lambert Academic Publishers (Chrisphin Karthick 2012).*

**Chapter3:** This chapter deals with the Narrow band photometry work of seven galaxies, observations and results of identified star forming regions in a galaxy, determination of  $H\alpha$  flux, Star formation rate, Photometry equivalent width of  $H\alpha$  and Age of the recent star forming regions are discussed. *The study discussed in chapters 3,4 and 5 are submitted for the publication in a referred journal(MNRAS) after getting inputs from experts of the same field.*

**Chapter4:** This chapter deals with the spectroscopy work of seven galaxies and calculation of oxygen abundances and reddening results.

**Chapter5:** This chapter deals with the Broad band photometry work of seven galaxies and results of age of the dominant stellar populations.

**Chapter6:** This chapter deals with the analysis of seven galaxies.

**Chapter7:** It is about the summary of the whole work and its conclusion. Also, about the brief out line of the future plans.



# Chapter 2

## Observations and Data Analysis

### 2.1 Introduction

This thesis consists of results obtained using (i) Narrow-band imaging ( $H\alpha$ ) (ii) Spectroscopy, and (iii) Broad-band ( $UBVRI$ ) imaging of a sample of Wolf-Rayet galaxies. These three modes of observations are very essential to identify and study the properties of the star forming regions in the Wolf-Rayet galaxies. The astronomical observations in the optical regions are usually done with a set of instruments, which consist of telescope, filters and detectors. A telescope collects and concentrates the radiation to the instrument at its focus. Light gathering power of a telescope is proportional to the diameter of its primary mirror. The function of filters is to pass only a limited spectral range of star light and block the remaining. Because of filters it could be possible to tell the colour of any object. Now-a-days, Charge Coupled Devices (CCDs) are used as detectors. <sup>1</sup>

---

<sup>1</sup>A book “ **Astronomer’s Data Reduction Guide; Author: Chrispin Karthick. M :ISBN:978-3-8473-3193-3; Lambert Academic Publishers, Germany** based on this chapter has been published. This book explains data reduction using Image Reduction and Analysis Facility (IRAF) package in detail.

## 2.2 Observations

### 2.2.1 Instruments Used

#### Telescopes



FIGURE 2.1: HCT 2-m Telescope

**Filters:** The filters used for observations are  $U, B, V, R, I$  and  $H\alpha$  filters.  $U, B, V, R,$  and  $I$  are broad-band filters, whereas  $H\alpha$  is the narrow-band filter. Each filter has a central wavelength and a band-pass which is allowed by that filter. Central wavelength and allowed band-pass of the filters used for this study are given in Table Table. 2.1. The filters  $U, B, V, R$  and  $I$  are abbreviation of *U*ltraviolet, *B*lue, *V*isible, *R*ed and *I*nfrared, respectively. Filters are used in astronomy for basically two purposes, either to reduce the overall intensity of light or to restrict the wavelength range of the incoming light. Since the modern day detectors invariably have a wider wavelength response and an improved sensitivity as compared to previous detectors, filters are important for the flux measurement of various astronomical objects at different wavelengths. The broad band filters

TABLE 2.1: System parameters of the telescope, filters and detectors used for observations

Telescope	Sampuranand Telescope (ST)	Himalayan Chandra Telescope ( HCT)
Place	ARIES, Naintal, India	IAO, Hanle, India
Longitude	79° 27' 24" E	78° 57' 51" E
Latitude	29 21' 42" N	32 46' 46" N
System	Ritchy-Chretien	Ritchy-Chretien
Focal ratio	Cassegrain:f/13	Cassegrain:f/9
Plate Scale	15" .5/mm	11" .5/mm
Diameter of primary mirror (m)	1.04	2.01
Altitude (m)	1955	4250
Filters/ $\lambda(\mu\text{m})$ / $\Delta(\mu\text{m})$	U/0.36/0.06 B/0.44/0.10 V/0.55/0.09 R/0.70/0.22 I/0.90/0.24 H $\alpha$ /0.65/0.01	U/0.36/0.06 B/0.44/0.09 V/0.55/0.09 R/0.64/0.16 I/0.80/0.15 H $\alpha$ /0.65/0.008
Saturation Limit(counts)	32768	65536
Chip dimation (pixel <sup>2</sup> )	2048×2048	2048×4096 central 2048×4096 used for imaging
Field of view (arcmin <sup>2</sup> )	~13×13	~10×10
Pixel size (arcsec/pixel)	0.37	0.29
Gain (e <sup>-</sup> /ADU)	10	1.22
Readout noise (e <sup>-</sup> )	5.3	4.8

used for the present study are Johnson UBV and Cousins RI with ST, Naintal and Bessell UBVRI filter system with HCT, Hanle. The filters used are a combination of coloured glasses of WG, GG (Sulpher and Cadmium sulfide) and OG (Cadmium selenide) which absorbs light quite sharply blueward of defined wavelengths. The UG (violet) and BG (blue) are made of ionic glasses.

**CCD:** This is an abbreviation of Charge Coupled Device (CCD), This is the widely used detector in almost all the back-end instruments of the telescopes. It is essentially made of pure silicon. This element is thus ultimately responsible for the response of the detector to various wavelengths of light. The CCD operation

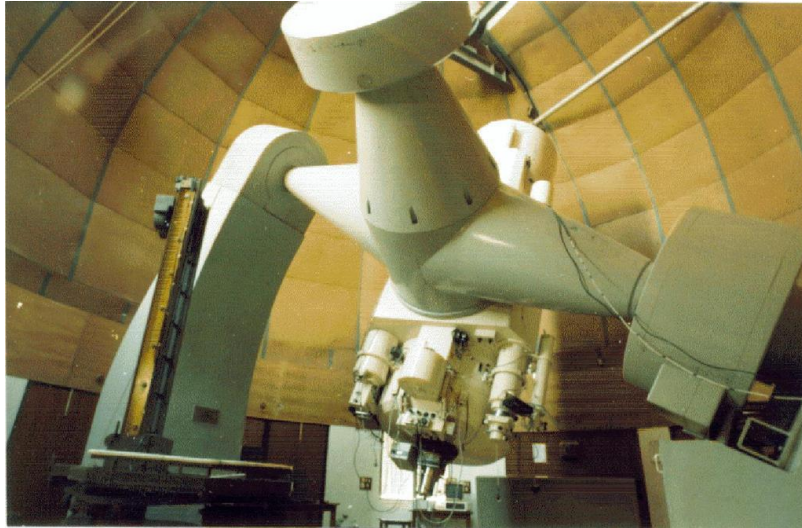


FIGURE 2.2: ARIES 1-m Telescope

is based on the photoelectric effect and can be described as follows. The photons which are coming from the source hit the silicon chip within a pixel and are easily absorbed. The photon absorption causes the silicon to give up a valence electron and move it into the conduction band. Once electrons have been freed to the conduction band, they are collected and held in place until readout occurs. When the exposure is over, CCD readout begins, such that the charge stored within each pixel is electronically shifted in a serial fashion along columns from one CCD pixel to another throughout the array. The charge collected within each pixel is measured as a voltage and converted into an output digital number within a device called an analog-to-digital converter. The output digital numbers are usually stored in computer memory. These CCD whole set up is kept in a very low temperature around  $-100^{\circ}\text{C}$  to  $-120^{\circ}\text{C}$

### 2.2.2 Scientific Objectives

- *Finding the star forming regions (knots) in the WR galaxies and derive the  $\text{H}\alpha$  flux and luminosity of star forming regions and determining Star Formation Rate (SFR) solar mass per year.* This work is done through photometry of star forming regions using the narrow-band  $\text{H}\alpha$  filter and

broad-band R filter (used for subtracting the continuum falling within the H $\alpha$  band-pass).

- *Finding the age of star forming regions* using H $\alpha$  equivalent width. *Determining the Oxygen abundances*  $12+\log(\text{O}/\text{H})$  and *reddening* in the knots from the emission line ratios. Spectroscopic observations of star forming regions is used to achieve this goal.
- *Estimating the ages of the stellar populations present in the knots.* This is done by comparing the observed broad-band colours of star forming regions and those predicted by Starburst99 model.

### 2.2.3 Sample Selection

The sample of Wolf-Rayet galaxies studied here are selected from the catalog of WR galaxies of Schaerer et al. (1999). The sample of Wolf-Rayet galaxies are chosen using the following criteria:

- The Declination limitation from +70 to  $-10$  degree.
- Observable magnitude limitation.
- Recession velocity less than 3000 km/sec (as in the objects with higher redshift H $\alpha$  emission will be shifted away from the available filter band-pass and the flux estimation will not be correct).
- The objects which are less studied are given higher priority.

TABLE 2.2: List of WR galaxies observed in our study<sup>a</sup>.

Object Name	NGC 1140	IRAS 07164+5301 <sup>d</sup>	NGC 3738	UM 311	NGC 6764	NGC 4861	NGC 3003
RA [ <i>J2000</i> ]	02 54 33	07 20 25	11 35 49	01 15 34	19 08 16	12 59 02	09 48 36
Dec [ <i>J2000</i> ]	-10 01 40	+52 55 32	+54 31 26	-00 51 46	+50 56 00	+34 51 34	+33 25 17
$m_V$ [ <i>mag</i> ]	12.8	14.13	12.13	17.9	12.56	12.9	12.33
$R_V$ [ $km\ s^{-1}$ ]	1501	12981	229	1675	2416	833	1478
Distance <sup>e</sup> [ <i>Mpc</i> ]	17.90	177	5.56	18.7	31.3	14.8	24.00
E(B-V) <sup>c</sup> [ <i>mag</i> ]	0.038	0.075	0.010	0.039	0.067	0.010	0.013
$M_V$ [ <i>mag</i> ]	-18.43	-22.03	-16.59	-13.42	-19.85	-17.94	-19.56
$Z^b$	0.010	0.014	0.014	0.0074	0.0195	0.0033	0.016
1'.2 (arc min)	6.1 kpc	60.96 kpc	1.9 kpc	6.4 kpc	10.6 kpc	5.1 kpc	8.16 kpc
Galaxy Morphology	IBm pec	-	Irregular	-	SBb	Irregular	SBbc

*a*: Data taken from NASA/Extragalactic Database (NED).

*b*:  $Z = 0.02 * 10^{\log(O/H) - \log(O/H)_\odot}$ , assuming  $12 + \log(O/H)_\odot = 8.66$ , Asplund et al. 2005

*c*: Foreground extinction from Schlegel et al (1998).

*d*: Calculated parameters.

*e*: Luminosity distance.

TABLE 2.3: List of Standards Observed

Galaxy Name	Landolt stand	Spec. std	H $\alpha$ std
NGC 1140	PG 0231+051	Feige 34	Feige 34
IRAS 07164+5301	PG 0231+051/Ru 149	Feige 34	-
NGC 3738	PG 0231+051/PG 1323	Feige 34	G19138
UM 311	Ru149	Feige 34	G 19138
NGC 6764	Ru149	Feige 110	Feige 34
NGC 4861	PG 1323-086	Bd+332642	Hz 44
NGC 3003	PG 1633+099b	Feige 34	Feige 34

## 2.3 Data Reductions

All preprocessing and data reduction was done in the standard manner using various tasks available with Image Reduction and Analysis Facility (IRAF). The CCD images received directly from the telescope are called raw images. These images need to be reduced (or Processed) to extract important information like position, luminosity and image shape of the objects that the frame contains. The reduction of the CCD data is necessary to remove the contamination due to atmosphere, telescope, the CCD itself and its associated electronics tend to degrade the image. Along with this the strong atmospheric turbulence, poor focusing, the presence of charge diffusion in the detector, different noises which are superimposed on the image also affect the quality of the image greatly. Extraction of useful information from this kind of environment is one of the main purposes of image reduction. Data reduction was carried out using IRAF software packages. DS9 is used as image displaying tool while data reduction.

**Photometric Observation:** Photometry is basically the measurement of light coming from astronomical sources at different wavelengths. Astronomically it is generally thought of in terms of measuring the brightness and colours of stars but it also includes the investigation of surface brightness in extended objects such as the moon, the planets, galaxies. The data reduction is done in three steps,

viz: 1) Pre-processing : Cleaning of the raw images. 2) Processing : Acquiring instrumental magnitude. 3) Post-processing : Acquiring standard magnitude.

### 2.3.1 Pre-Processing

The process of standard CCD image reduction makes use of a basic set of images that form the core of the calibration and reduction process (Gullixson, 1992). The types of images used are essentially the same in imaging, photometric, and spectroscopic application although generated by different sources. This basic set of images consists of calibration frames such as bias frames, flat frames and the object frames of the object(s) of interest. The software package IRAF (Image Reduction and Analysis) was used for the complete processing. The steps involved are:

### 2.3.2 Cleaning

**Bias Subtraction:** This is an image of exposure time of zero seconds. The shutter remains closed at the time of exposure and the CCD is simply read out. The purpose of a bias frame is to determine the underlying noise level within each object frame. The bias value in a CCD image is usually a low spatial frequency variation throughout the array, caused by the CCD on-chip amplifiers. This variation should remain constant with time. The rms value of the bias level is the CCD read noise. A bias frame contains both the DC offset level and the variations on that level. These bias variations for a given CCD are usually column-wise variations, but may also have small row-wise components as well. Thus, a 2-D, pixel-by-pixel subtraction is often required. Statically saying, a single bias frame will not sample these variations well, so an average bias image of 10 or more single bias frames is recommended. The task used is `zerocombine`. Then, with `ccdproc` one can subtract the bias level to remove the dc voltage from the images.

**Flat Fielding:** All the pixels in the CCD do not have the same sensitivity, though ideally that is the requirement. Thus the resulting images present spatial noise because adjacent pixels did not react in the same way to identical incident flux. Correction of non-uniform sensitivity is obtained by acquiring an image made on a uniform sky background like the twilight sky, or a projector lamp like halogen lamp in the case of spectroscopy an attempt to provide a high S/N, uniformly illuminated calibration image. Flat field calibration frames are needed for each color, wavelength region, or different instrumental setup used in which object frames are to be taken. And then flat field is carried out by dividing the object frame by this flat frame after normalization. By taking the median value of all the flat frames after subtracting bias and then normalized to make master flat. These master flats were then used to flat field the object images. Thus, mathematically the bias subtraction and flat fielding of image looks like this

$$\text{Final calibrated image}_{(Filter)} = (\text{Raw Object image} - \text{Master bias}) / \text{Flat field frame}_{(Filter)}$$

In this master bias is common for the all the filter, where in for flat fielding we have to use that respective filter image as mentioned above.

**Cosmic rays removal:** While observing the objects of our interest in the sky, there is a possibility that the cosmic rays may also hit the detector and get recorded with the objects in the CCD frames. These are easily visible by their streak or tiny spots in the frames. These bright spots are because of cosmic rays. Stellar intensity profile and cosmic ray intensity profile are different which is the underlying property used for the removal of cosmic rays from object frames. COSMICRAYS are removed using the MIDAS reduction package.

### 2.3.3 Aligning and Combining of sub exposure frames

Some time the object frames are observed with many sub exposures, later they are added up to improve the signal to noise ratio. Practically, it is difficult to get all the frames without the object of interest being misaligned. So, it is necessary

that all the frames should be aligned with respect to a reference image before combining them.

Image alignment is done by choosing a maximum possible number of stars from the reference frame and making a coordinate file. The same stars in the same order of selection should be identified in the other frame and using GEOMAP and GEOTRAN routines in IRAF we get the transformed image. GEOTRAN corrects an image for geometric distortion using the coordinate transformation determined by GEOMAP. The transformation is stored as the coefficients of a polynomial surface in record transforms, in the text file database . The coordinate surface is sampled at every xsample and ysample pixel in x and y. The transformed coordinates at intermediate pixel values are determined by bilinear interpolation in the coordinate surface. Only one image can be aligned at a time and hence the procedure is repeated for the rest of the frames. Later, in few cases, IRAF alignment scripts also used.

## 2.4 Processing

**Measuring Instrumental Magnitudes:** After the object frames have been corrected for instrumental effects, they can be used to measure instrumental magnitudes. The instrumental magnitudes of the program and standard or check stars can be measured using one of two classes of measuring techniques, namely aperture photometry or point- spread-function fitting.

### 2.4.1 Aperture photometry

The principle behind aperture photometry is the measuring of the starlight that falls within a defined circular region or aperture. The aperture has to be large enough to enclose the entire stellar image, therefore measuring all the light from the stellar image. The total flux is the added flux from the separate pixels inside

the defined aperture. The flux from the background sky is measured using a similar aperture technique with the aperture defined over a region free of stars. The difference between the two flux values gives the true apparent flux from the star. The instrumental magnitude thus measured is

$$m_{inst} = A - 2.5 \log \left( \frac{(\sum_{i=1}^n C_i) - nC_{sky}}{t} \right) \quad (2.1)$$

Here  $A$  is an arbitrary constant,  $C_i$  is the  $i$ th pixel count inside the aperture,  $C_{sky}$  is the average pixel count for the sky background,  $n$  is the number of pixels in the aperture, and  $t$  is the exposure time for the object frame. The exposure time component is used to normalize object frames with different exposure times. The sky background can be measured using a variety of different techniques. One is to use a defined aperture to measure a neighbouring region of blank sky, while the more preferred method is to use an annulus that surrounds the original aperture. The resulting counts corresponding to a particular star are converted into magnitude scale. For such kind of work routine PHOT in IRAF may be also used to do aperture photometry with equivalent results.

## 2.4.2 Calibrating Instrumental Magnitudes

After the instrumental magnitudes have been measured for all the stars of interest in all the different object frames and for all the different filters, the instrumental magnitudes need to be calibrated. The calibration needs to be applied to convert the measured instrumental magnitudes to a standard photometric system. There are two effects that have to be corrected for, namely the discrepancies between the instrumental and target standard system, and the effect of atmospheric extinction. The extent of the calibration will depend upon the photometric research requirements. Thus, for differential photometry only corrections for atmospheric extinction have to be considered, whereas for absolute photometry both effects have to be considered.

### 2.4.3 Determination of Extinction Coefficients

Atmospheric extinction is used to describe absorption and scattering of electromagnetic radiation emitted by the celestial objects by matter (dust and gas) between the emitting object and the observer. For earth bound telescopes it arises both from the interstellar medium and the earth's atmosphere and it may also arise due to circumstellar dust around and observed object. Since blue light is much more strongly attenuated than red light in the optical wavelength regions, it results in an object which is much redder than expected.

The amount of atmospheric extinction depends on the altitude of an object, being lowest at the zenith and at a maximum near the horizon. It is calculated by multiplying the standard atmospheric extinction curve by the mean airmass ( $X$ ) calculated over the duration of the observation. When the zenith angle is small to moderate, a good approximation is given by assuming a homogeneous plane-parallel atmosphere (i.e., one in which density is constant and Earth's curvature is ignored). The airmass  $X$  then is simply the secant of the zenith angle  $z$ : At a zenith angle of  $60^\circ$ , the airmass is approximately 2. By definition, airmass is the optical path length through Earth's atmosphere for light from a celestial source and it is 1 at zenith and rises to larger values with increasing  $z$ . To measure the extinction coefficients, the aperture photometry of the 30 standard stars of the Landolt (1992) field taken at different airmasses have been performed. From the plots of  $u$ ,  $b$ ,  $v$ ,  $r$ ,  $i$  magnitudes of the same stars in all the frames against airmass, the atmospheric extinction coefficient  $k_u$ ,  $k_b$ ,  $k_v$ ,  $k_r$ ,  $k_i$ , respectively were determined from the slope of the straight line. The atmospheric extinction correction were applied to the observed instrumental magnitudes, using the following relations.

$$u_0 = u - k_u \times X$$

$$b_0 = b - k_b \times X$$

$$v_0 = v - k_v \times X$$

$$r_0 = r - kr \times X$$

$$i_0 = i - ki \times X$$

where  $u$ ,  $b$ ,  $v$ ,  $r$  and  $i$  are the instrumental magnitudes and  $u_0$ ,  $b_0$ ,  $v_0$ ,  $r_0$  and  $i_0$  are the extinction corrected magnitudes.

## 2.5 Post-Processing

**Transformation to the standard System :** Instrumental spectral characteristics which are set by the combination of the detector and the filters, cannot exactly match the reference photometric system. Consequently, when observing the standard stars whose magnitudes and colour indices are defined in the reference system, the difference between the values in the catalogue and those measured is always found. However, they are related by the following equations:

$$(U - B) = a_1 \times (u_0 - b_0) + a_2$$

$$(B - V) = b_1 \times (b_0 - v_0) + b_2$$

$$(V - I) = c_1 \times (v_0 - i_0) + c_2$$

$$(V - R) = d_1 \times (v_0 - r_0) + d_2$$

$$(R - I) = e_1 \times (r_0 - i_0) + e_2$$

$$V - v_0 = f_1 \times (B - V) + f_2$$

$$V - v_0 = g_1 \times (V - R) + g_2$$

Where  $(U-B)$ ,  $(B-V)$ ,... and  $(V-I)$ ,  $V$  are values of standard stars taken from Landolt (1992) and  $u_0$ ,  $b_0$ ,  $v_0$ ,  $r_0$  and  $i_0$  are the extinction corrected instrumental magnitudes. For calibration purpose, we observed standard fields of Landolt (1992). The stars used for calibrations cover a wide range in brightness as well as colour.

Here  $a_1$ ,  $a_2$ ,  $b_1$ ,  $b_2$ ,  $c_1$ ,  $c_2$ ... etc are the transformation coefficients and UBVR I are the standard magnitudes. First, we have to use this set of equations for the known Landolt standard (Landolt 1992) for finding the coefficients and then apply this to get the knots magnitude. After rearranging the last two equations we can get the final std V mag. Apply this V mag, in the above set of combined equations then we can get the alternate other magnitudes of U, B, V, R and I by applying in to those equations. Thus, we could derive the standard magnitudes of all the knots.

## 2.6 Spectroscopic Reduction

### 2.6.1 Introduction

Spectroscopy is one of the fundamental tools that allows one to determine the chemical compositions, physical properties, and radial velocities of astronomical objects. The spectroscopy of an astronomical object is done with an instrument called spectrograph, which contains these essential elements: a slit on to which the light from the telescope would be focused; a collimator, which would take the diverging light beam and turn it into parallel light; a disperser (usually a reflection grating); and a camera that would then focus the spectrum onto the detector. The slit sits in the focal plane, and usually has an adjustable width. The image of the astronomical objects is focused onto the slit. The diverging beam continues to the collimator. In most of the astronomical spectrographs, the disperser is a grating, and is ruled with a certain number of grooves per mm. Spectroscopic data reduction is done using the software package IRAF. The pre-processing steps like bias subtraction, flat fielding, dark correction and cosmic ray removal are similar to those discussed in the case of photometric data reduction. Main steps involved in this are:

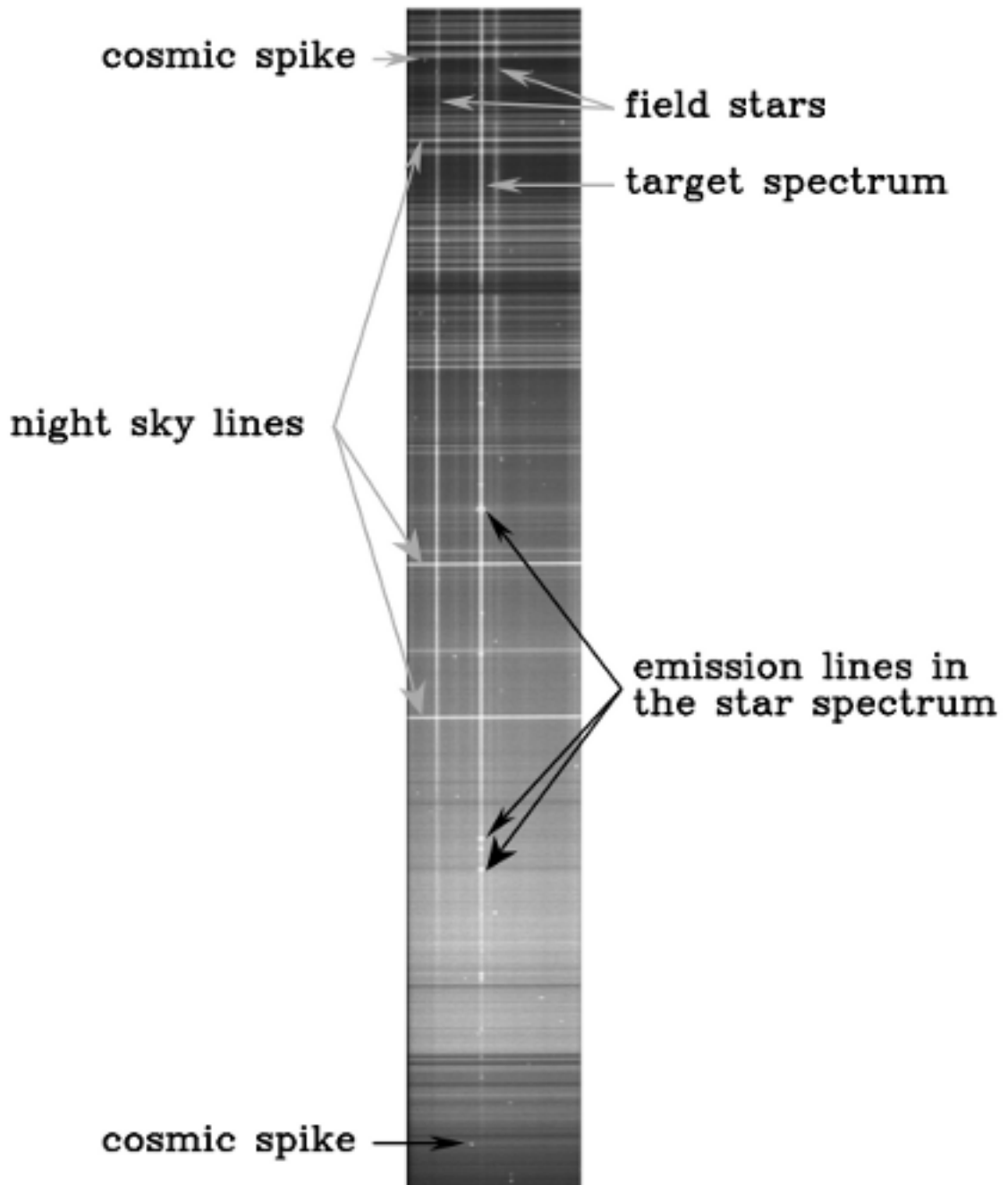


FIGURE 2.3: Typical Star spectra (WIP graphics courtesy T.Tomov)

1. Basic data reduction (Bias subtraction and Flat fielding)
2. Spectrum extraction
3. Wavelength calibration
4. Flux calibration.

## 2.6.2 Observations

Optical spectra are obtained in the form of two-dimensional CCD images (Fig. 2.3). The long slit spectroscopic data consists of bias frames, flat frames, calibration frames and object frames. These frames are acquired for each observing night. The object frames contains the image of the star focused at a slit. This image is made to disperse on the CCD frame along a particular direction known as dispersion axis, which is parallel to the slit width direction when the CCD axis is properly aligned with the slit axis. In order to avoid any degradation of resolution as well as the sky background contribution, the slit widths are usually kept equal to the FWHM of the stars seeing limited image. As a result the spatial profile of the star is governed by the seeing. Hence, the pixels along the dispersion axis are measured in wavelength units, while the pixels along the spatial axis in counts of flux units. In order to convert these pixels and counts in wavelength and flux respectively, calibration frames are required. Arc frames and standard star frames are required for wavelength and flux calibration respectively.

## 2.6.3 Instruments Used

Optical spectra of the galaxy in their nuclear and some star forming regions were obtained with the Himalaya Faint Object Spectrograph and Camera (HFOSC) of 2.01 m HCT. The disperser Grism 7 which has a wavelength range of 3500 - 7600Å in combination with a slit of 11' length and 1."92 width (i.e., slit 1671) is used for the observations. Further details on the 2.01 m HCT and the instrument can be found at the IIA site.<sup>2</sup> During observations, a series of calibration spectra using iron-argon lamp and flat frames using the halogen lamp were also taken. Flat fields and arc lamps were taken immediately following each target object. The standard flux calibrator stars from Oke et al. (1990) and Massey et al. (1988) were also observed during the nights, whenever required.

---

<sup>2</sup><http://www.iiap.res.in/iao/hfosc.html>

## 2.7 Data reduction

**Cleaning** : Cleaning of raw image is almost similar to that of photometry. Here, we summarize the process that involved to remove the artifacts using the IRAF tasks. The corrections for bias were made using the frames obtained with no exposure. A composite flat field was created for each day of observations by combining the individual flat field calibration lamps. The flat field was normalized using the median value of the central dispersion row. The response of the flat field for each strip was calculated using the IRAF routine, RESPONSE, and applied to each arc lamp and on-source exposure. Unlike a traditional flat field, the response function calculates a polynomial fit to the average flat field along the dispersion axis and then returns the deviation from this fit at each pixel. The response for the flux calibrator was calculated in the same manner, therefore, applying the flux calibration will remove the overall spectral shape of the flat field.

Cosmic rays removal was done through the `apall` task itself which does well, instead of using other tasks. Provided its RON(Read out noise) and  $e^-/ADU$  parameters as well as wide-enough median-type extraction of the background are set properly in `apall`. Also, in some of the cases MIDAS is used for cosmic removal.

### 2.7.1 Aperture Extraction

The one dimensional spectra are extracted using APALL task, which is based on the extraction algorithm by Horne (1986) which is actually a collection of many tasks. After determining the aperture (objects part of the tracing) and background (which sky regions will be used for subtraction) it traces the spectrum (finds its path in the direction of dispersion) and sums it up in a mono-dimensional line. This task eliminates the sky noise, delivers maximum possible

signal-to-noise ratio and takes care of the effects of moderate geometric distortion and cosmic ray hits. The one dimensional spectrum is in the form of intensity versus pixel number.

In order to calibrate the pixel-number in terms of wavelength, it is necessary to take spectra of a laboratory standard source (e.g. Fe-Ar arc-lamp). For such a standard source wavelength of different spectral features such as emission are known. The wavelength calibration is done using IDENTIFY, HEDIT and DISPCOR task of IRAF. Usually a high order polynomial is employed to fit the identified pixels against wavelength. Flux calibration is performed using the tasks STANDARD, SENSFUNC (used to fit a polynomial to the observed magnitude as a function of wavelength after applying extinction correction in the standard and object star spectra) and calibrated.

## 2.7.2 Wavelength Calibration

To calculate the pixel-to-wavelength solution, we extracted a 1-D spectrum from the arc lamp exposure for each slit using the slit tracing. The above procedure provides the one dimensional spectrum as a function of the pixel number. The wavelength calibration was made using comparison spectra (spectra of arc lamps) obtained by the same setup of the spectrograph as applied to the object. The laboratory wavelengths of individual arc spectral lines were known. Here the relation between the wavelength and the CCD pixel number was made using the lamp spectra. Individual arc lines within the spectrum were marked through the IRAF task, IDENTIFY. The wavelength solution was determined by fitting a polynomial to these line identifications. The wavelength solution was applied to each program spectra using the IRAF tasks, REFSPEC and DISPCOR. Then the spectral shift is corrected using the task SPECSHIFT by taking the reference lines as standard atmospheric lines like 5577Å, 6300Å and 6364Å. And if there are multiple sub exposures for the object frames, then they are combined using the task scombine to increase the signal to noise ratio.

### 2.7.3 Flux Calibration

For flux calibration of wavelength calibrated spectra, spectrophotometric standards from the list of Massey et al. (1988) were observed. The expected flux from these standards are listed in the National Optical Astronomy Observatory (NOAO) "onedstds" mostly from 'spce50cal'. At a given airmass of the flux calibrator observations, a predicted template spectrum was generated for each flux calibrator. This predicted template spectrum was divided by the observed flux calibrator spectrum normalized by the exposure time to derive a sensitivity function using the task SENSFUN. Each exposure of a star spectrum was divided by the sensitivity function to calculate a flux-calibrated spectrum. A final flux-calibrated spectrum can be produced for each star by averaging over the flux-calibrated spectra extracted from each individual exposure, whenever necessary.

To make the normalized spectra, we trimmed the spectra at the edges where the count level is very low at the edges of spectra. The trimming was done by the task IMCOPY. The normalization was carried out by the task CONTINUUM, where we fit a function to the spectrum, and the absorption lines were excluded from the fitting. Fluxes and equivalent widths of the emission lines were measured using the Gaussian profile fitting option in the IRAF task SPLOT. Then the redshift is corrected for the galaxy through the DOPCOR, this is corrected through the velocity parameter. Finally, It is corrected for the foreground reddening correction using the task DEREDDEN.

Now, this calibrated spectra is ready for the scientific work like determining oxygen abundances and intrinsic galactic extinction through balmer line fluxes ratio and in some case finding the unknown velocity parameter. For example here for the galaxy IRAS 07164+5301, the velocity is determined in this way.



# Chapter 3

## Star Formation Rate

### 3.1 Introduction

The first quantitative studies of star formation in nearby galaxies was done by Tinsley (1968), who derived the star formation rates (SFR) from evolutionary synthesis models of galaxy colors. And further modelling by Larson & Tinsley (1978) showed that evolution of low-mass galaxies and interacting galaxies are strongly influenced by a burst mode of star formation. SFRs in galaxies show a large range from basically zero in gas-poor ellipticals, S0 and dwarf galaxies to  $\sim 20 M_{\odot}\text{year}^{-1}$  in gas rich spirals (see Kennicutt 1998,review). Also, star formation takes place in two distinct physical environments: in the discs of spiral and irregular galaxies and in compact, dense gas discs in the centers of galaxies (Kennicutt 1998). To determine the star formation rates, mainly, four basic and widely used methods are used from integrated observations (Kennicutt 1998a): 1) UV continuum methods, 2) Far-IR and radio continuum methods(1.4GHz), 3) analysis based on recombination lines,(H $\alpha$ ) and 4) forbidden lines [O II] 3727Å. Among Some of the methods like through FIR and radio continuum luminosities are considered as best. since these are extinction-free. The SFR estimated from FIR and 1.4GHz radio continuum are found to be highly correlated over many

orders of magnitude. Measurements of the star-formation rate (SFR) usually apply strictly only to OB stars and it may be extrapolated to all masses, since less massive ones can not be distinguished from the older background population. In this study the  $H\alpha$  luminosity method has been taken to determine the star formation rate (i.e, how much amount of gas within galaxies is converted in to stars) through  $H\alpha$  observations (Narrow band photometry).

## 3.2 Observations

TABLE 3.1:  $H\alpha$  Observations

Galaxy Name .	Date [dd/mm/yy]	$H\alpha$ [Sec]	R [Sec]	Telescope
NGC 1140	17/12/2006	2100	900	HCT
IRAS 07164+5301	16/02/2010	4x900	3x180	HCT
NGC 3738	12/03/2008	1200	300	HCT
UM 311	31/10/2008	4200	360	HCT
NGC 6764	31/10/2008	2x900	900	HCT
NGC 4861	26/01/2011	1210	120	HCT
NGC 3003	17/12/2006	2x600	300	HCT

For this nature of work the observations made through using HCT 2m Telescope and through HFOSC imaging of  $H\alpha$  and R (as continuum) filters. HFOSC is equipped with a 2k×4k SITe CCD chip. The central 2k×2k region with plate scale of 0.296"/pixel,(Pixel size of 15× 15 micron) provides 10×10 arcmin field of view.

## 3.3 Identifying Star forming Regions

The star forming regions are scientifically known as knots. Filters with a narrow passband tuned to an atomic emission line are widely used for imaging faint emission nebula. By only transmitting light corresponding an emission line, these filters suppress the relative contribution from sources that emit over a wide

range of wavelengths. Since stars also emit over a wide wavelength interval they, too, are suppressed relative to a nebula. This is especially useful for bringing out faint nebulosity in a rich field of stars. If the nebula is extremely faint then even the stellar contribution can submerge it. In such case another CCD image can be made through a so-called ‘continuum filter’, designed to transmit a band of wavelengths close to but not overlapping with the nebula emission line. By subtracting this ‘continuum image’ from the narrowband image the stars can in principle be made to vanish altogether. Though it seems simple in principle, the process of subtraction is a bit more complicated in practice.

Generally, the images look as nebulosity and added with stellar continuum on one image and only stellar continuum on the other image(R). However, assume that the stellar point spread function (PSF) has a FWHM of  $\sim 2.0$  pixels on the narrowband image and  $\sim 1.5$  pixels on the continuum image. When subtracting the stellar continuum under such conditions bright or dark halo artifacts will then arise at each star position. The stellar FWHM varies from roughly 1.5-3 pixels and it does so differently on each image. Differences in FWHM can arise due changes in seeing, focussing and lens mounting and these are all very hard to eliminate completely. The FWHM distributions are now very similar and the continuum subtraction will result in fewer halo artifacts. If the subtraction is still seems not yet perfect, then it is mainly due to the fact that it is assumed as circular PSF’s. In reality the PSF is often slightly elongated and this too, varies in magnitude and direction across both fields of view. In general it is nearly impossible to do a perfect continuum subtraction to vanish all (especially) bright stars from the frame completely. This effect can be achieved by subtracting a scaled version of the continuum image.

## 3.4 Continuum Subtraction

### 3.4.1 Methodology

Narrow-band H $\alpha$  line image was obtained following the standard procedure by Waller (1990). *R* band image is used for continuum subtraction. Both the *R* band and H $\alpha$  band frames are all sky subtracted and made it unit time exposure or normalized with respect to exposure time. A scale factor between the H $\alpha$  and *R* band image was determined using the non-saturated field stars in the galaxy field, after taking care of the difference in FWHM of the stellar profile. The *R* band continuum image was scaled to the H $\alpha$  image and subtracted from H $\alpha$  image to get the H $\alpha$  line image of the galaxy.

$$H\alpha = H\alpha^* - R_{\text{continuum}} \times \eta$$

where  $H\alpha^*$  is the reduced H $\alpha$  frame containing the continuum,  $R_{\text{continuum}}$  is the frame containing only continuum and  $\eta$  is the scaling constant.  $\eta$  was obtained from the mean ratio of the total flux in point sources in the H and R bands which had identical point spread functions. Using the R filter as continuum is not ideal because it is too broad and contains not only the H $\alpha$  line itself but also additional lines, thus making the estimation of the continuum level inaccurate. In order to calibrate the continuum-subtracted H $\alpha$  frames, we also reduced the images of the spectrophotometric standards oke (1990) in each H $\alpha$  filter. Then we convolved the flux-calibrated spectrum of the standard star with the filter transmission and thus obtained the total flux in each filter in units of  $erg\ cm^{-2}\ s^{-1}$ . The filter transmission and the spectrum did not have the same step size, so we interpolated the missing values. Next, we measured the total flux in units of counts  $s^{-1}$  by doing aperture photometry on the reduced images of the standard stars. This gave us a conversion factor between  $erg\ cm^{-2}\ s^{-1}$  and counts  $s^{-1}$  which we used to calibrate our H $\alpha$  frames.

Thus obtained H $\alpha$  line images are used to identify the star forming regions or H II regions within the galaxy. The total counts from each of the H II regions are obtained through aperture photometry for which the sky is taken just about five pixels beyond the best aperture. The best aperture or the boundary of the H II regions is set where the counts are about 6 sigma above the local background. (Same aperture is used in the broad band photometry also for the identified star forming regions). The obtained total counts of the galaxy in this way are converted into flux using the standard procedure (Waller 1990),

From the spectrophotometry standard star's observation,

$$\text{Conversion factor} = \frac{\text{Theoretically calculated Std.star.Flux (flux)}}{\text{Observed counts from standard.star. image (counts/s)}} \quad (3.1)$$

Then multiplying this conversion factor with the knots counts which is observed from the galaxy gives the knot flux.

Hence, (Conversion factor) \* (knot counts/s) = Knot flux.

(i.e.....Unit wise.....(flux/Counts/s)\* (counts/s) = Flux.

Here the flux unit is  $erg\ cm^{-2}\ s^{-1}$ . Thus, calibrating H $\alpha$  images involves calculating conversion factor. As said above, this is done by comparing the theoretically calculated flux within the band as computed by integrating the stellar spectrum within the bandpass (Mayya & Prabhu 1996) with the observed counts for the spectrophotometric standard stars from Oke (1990).

H $\alpha$  equivalent widths are also calculated by using the equation (Waller 1990). The emission line equivalent width is defined as the ratio of the line flux by the continuum flux density at the central wavelength of the line,

$$EW(line) = f(line)/f_{\lambda}(cont) \quad (3.2)$$

$F_0$  is the zero point flux,  $R$  is the  $R$  magnitude corrected for extinction.  $\lambda$  corresponds to  $H\alpha$  line wavelength and  $c$  is the speed of light.

### 3.4.2 Continuum Subtracted Images of WR Galaxies

The knots (star forming regions) are identified after continuum subtraction. All observed images directions are represented in the figure as North is up and South is down. The  $R$ -band and the continuum-subtracted  $H\alpha$  images of all galaxies are shown in Figures 3.1 to 3.14. We used the continuum-subtracted  $H\alpha$  images to identify the star-forming regions (knots) within each galaxy. The knots were identified by visual inspection, but also through a threshold of 4-6 times sigma of background was also taken as the identification criteria. The corresponding identity number for each star-forming region is included in Fig. 3.1 to 3.14. Since, NGC 3003 has almost 25 star forming regions, to infer the variation within the cross-over galaxy, a plot Fig. 3.15 is made between the Knot region IDs Vs  $H\alpha$  equivalent width.

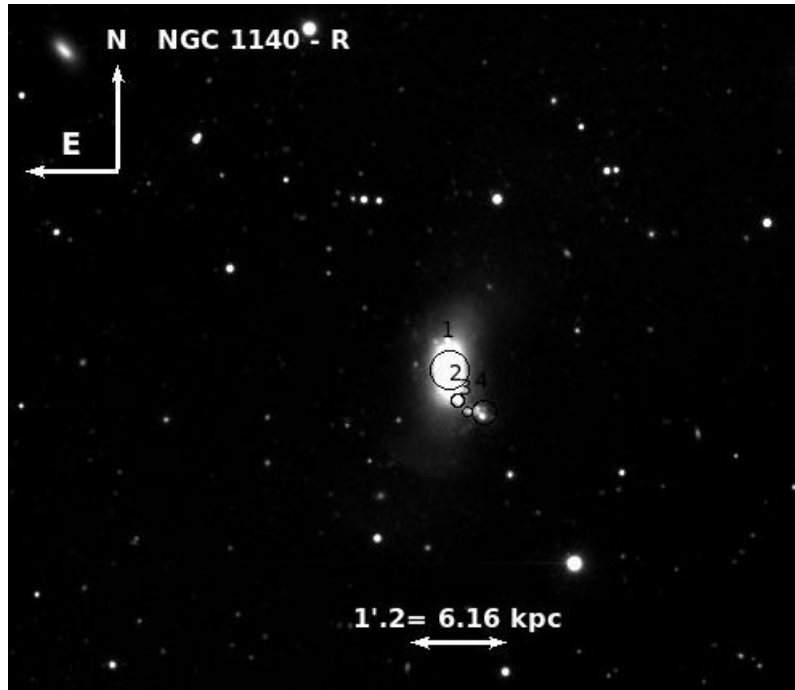
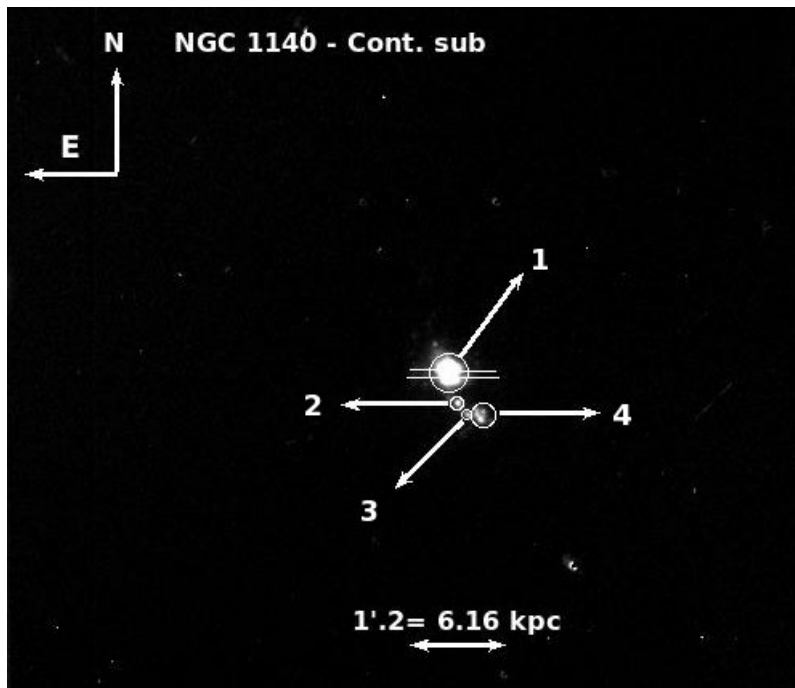


FIGURE 3.1: Broad-band R filter image of NGC 1140.

FIGURE 3.2: Continuum subtracted H $\alpha$  image of NGC 1140.

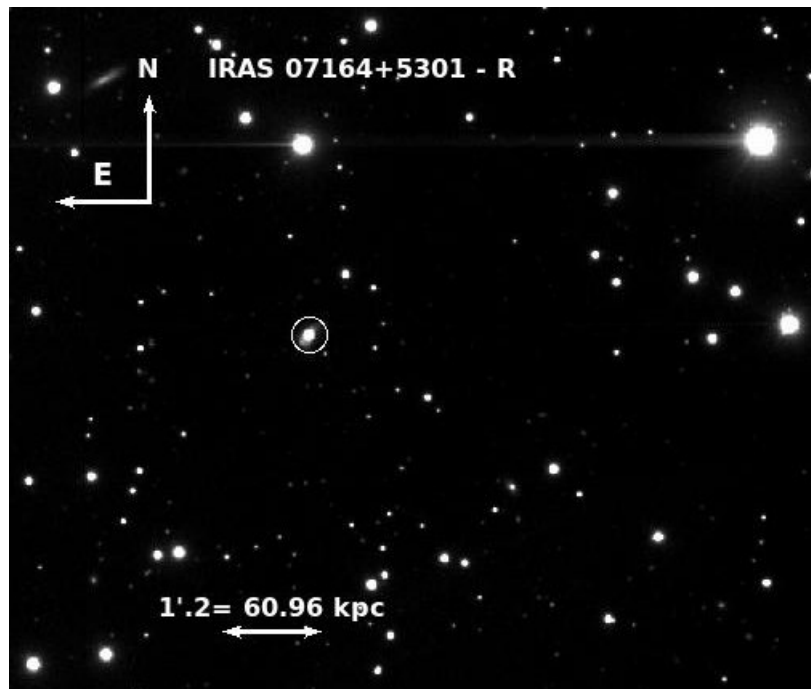
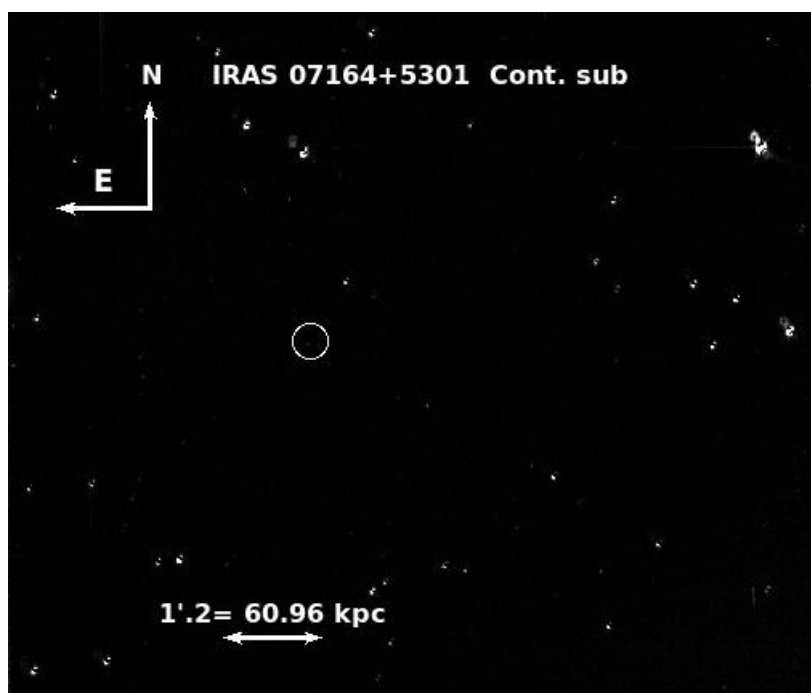


FIGURE 3.3: Broad-band R filter image of IRAS 07164+5301

FIGURE 3.4: continuum subtracted H $\alpha$  image of IRAS 07164+5301

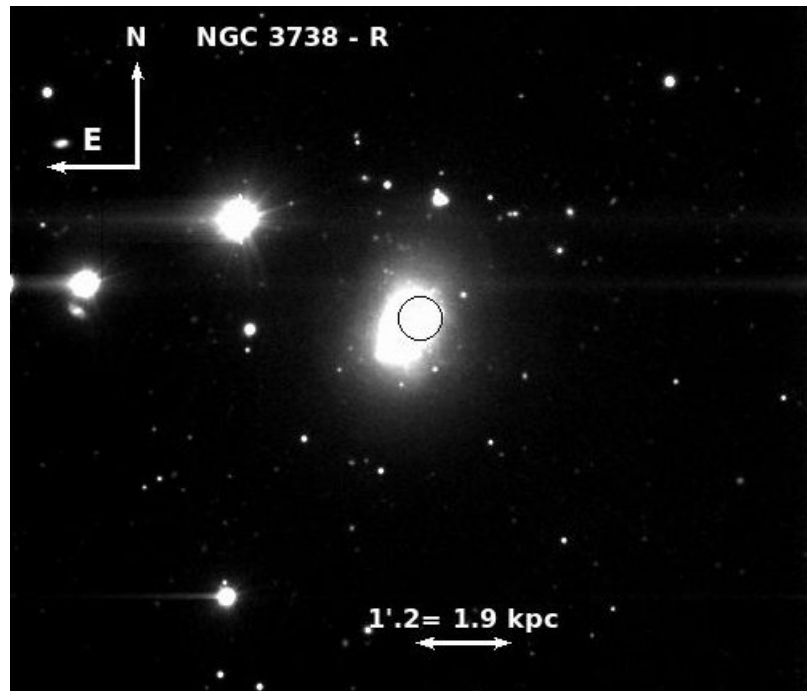


FIGURE 3.5: Broad-band R filter image of NGC 3738

FIGURE 3.6: Continuum subtracted H  $\alpha$  image of NGC 3738

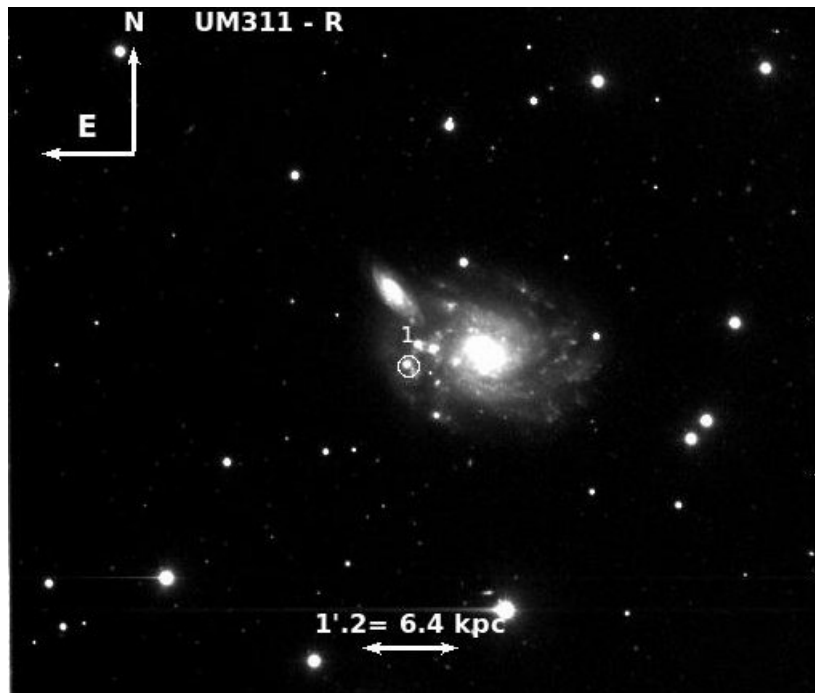
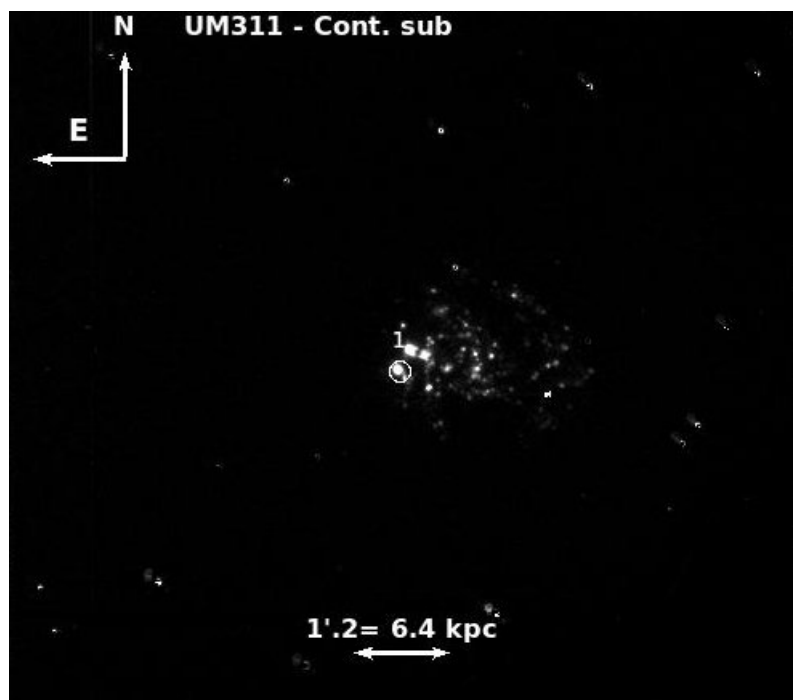


FIGURE 3.7: Broad-band R filter image of UM 311

FIGURE 3.8: Continuum subtracted H  $\alpha$  image of UM 311

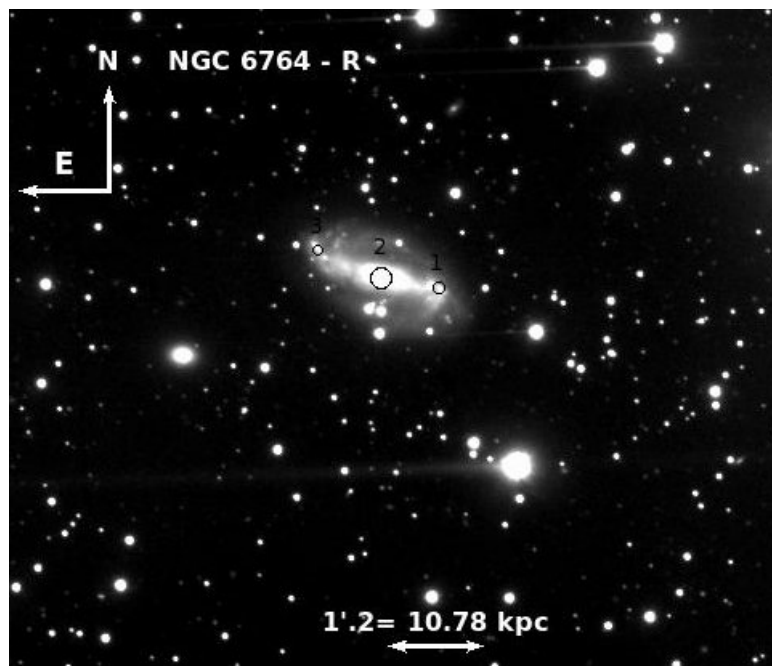
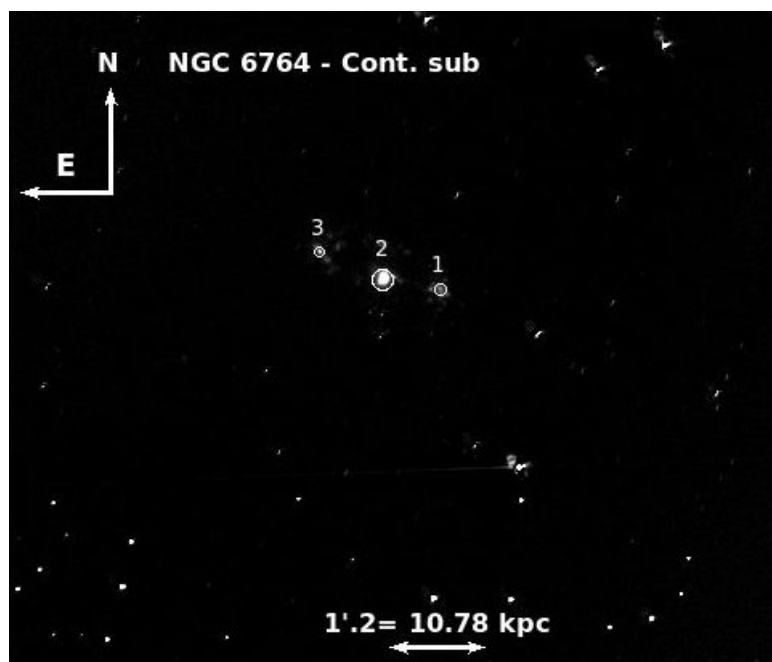


FIGURE 3.9: Broad-band R filter image of NGC 6764

FIGURE 3.10: Continuum subtracted H  $\alpha$  image of NGC 6764

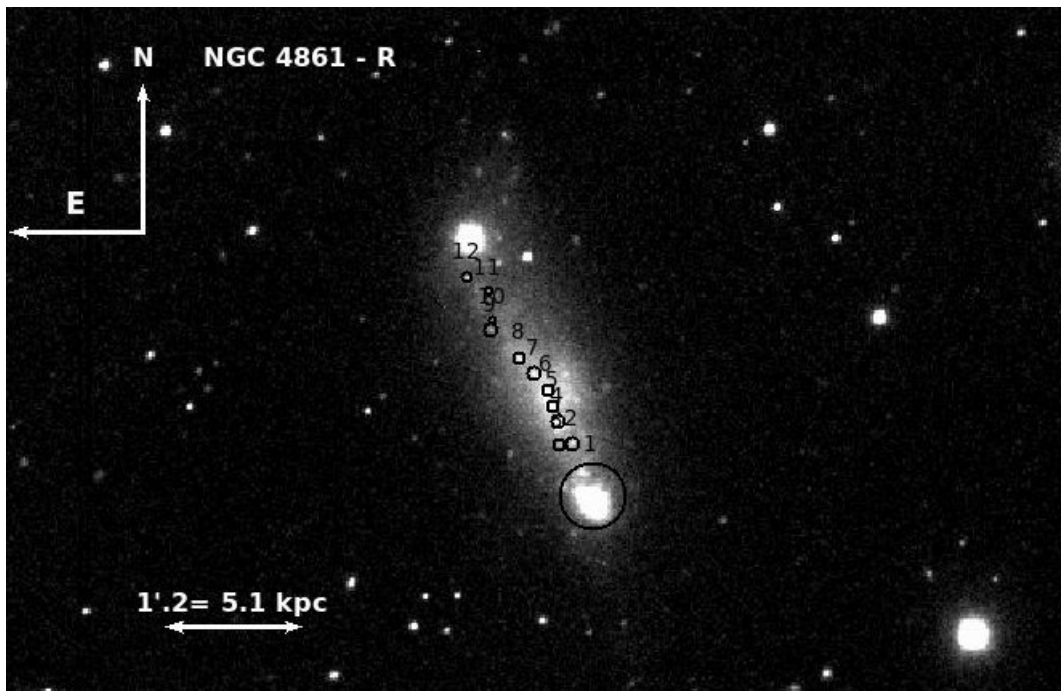


FIGURE 3.11: Broad-band R filter and continuum subtracted  $H \alpha$  image of NGC 4861

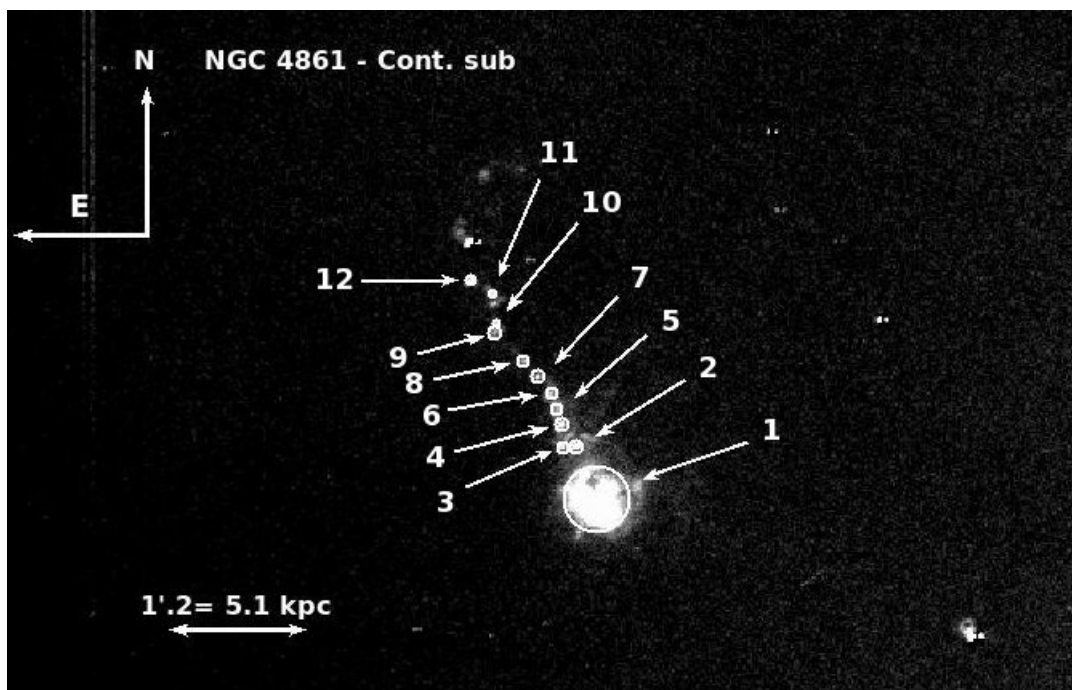


FIGURE 3.12: Broad-band R filter and continuum subtracted  $H \alpha$  image of NGC 4861

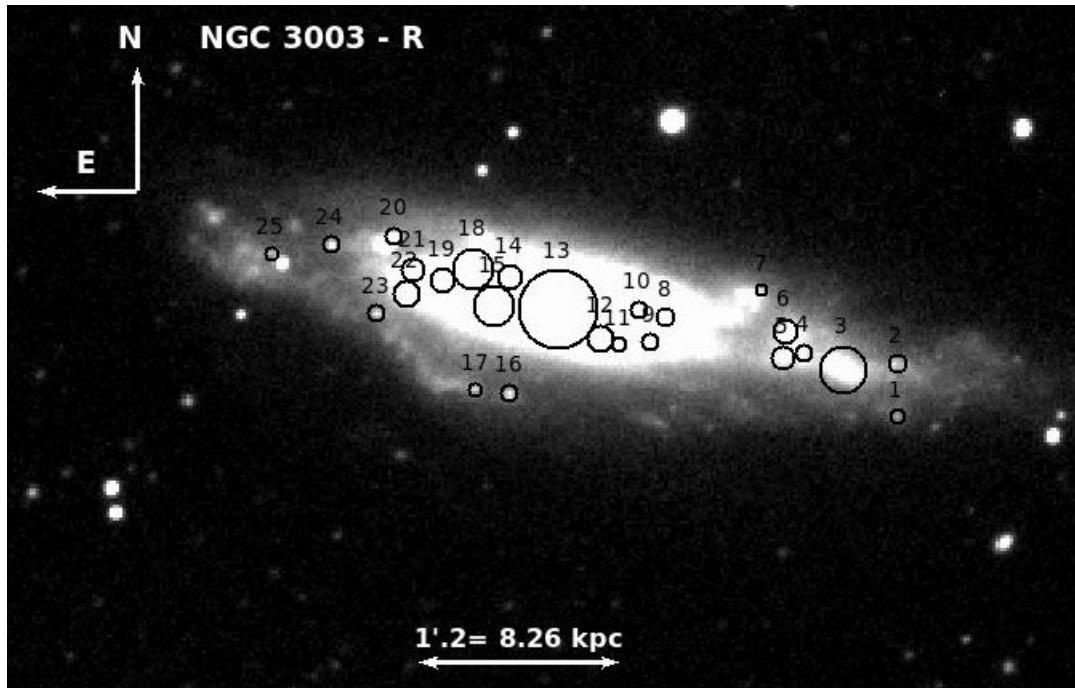


FIGURE 3.13: Broad-band R filter image of NGC 3003

FIGURE 3.14: Continuum subtracted H  $\alpha$  image of NGC 3003

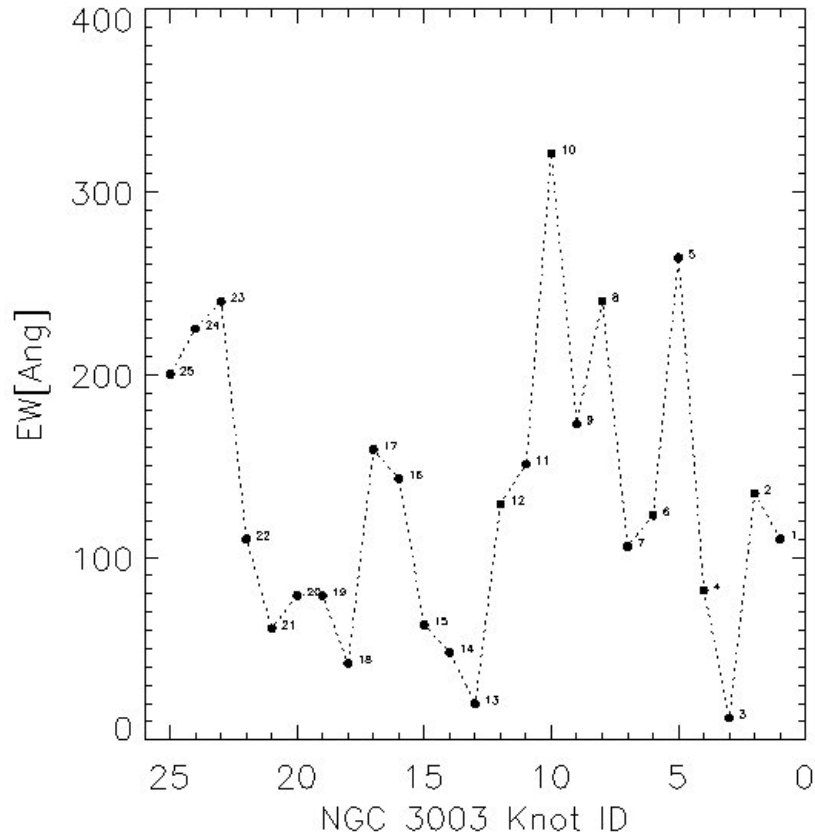


FIGURE 3.15: Plot of knots ID Vs equivalent width of NGC 3003

### 3.4.3 Arc distance

To Visualize the size of the galaxy or knots size, the calculated parsec scale is drawn in the figure for the 1.2 arc minute scale length. The scale length which is shown in the figure (double sided arrow mark) covers 240 pixels in the observed frame. As it is previously discussed the pixel scale for the HCT as  $0.296''/\text{pixel}$ , the scale length is as  $240 \text{ pixel} \times 0.296''/\text{pixel} = 71.04''$  that is  $\sim 1.2$  arc minute. As we know from the basic parallax relations, At a distance of one parsec, one astronomical unit subtends an angle of one arc second.

Since  $\Theta$  is small,  $\tan(\Theta) \simeq \Theta(\text{rad})$ , which is the value of  $\Theta$ , measured in radians.  $\tan(\Theta) \simeq \Theta = s/\text{Distance of the galaxy}$  ( arc sec= parsec/parsec) i.e.,

$$\Theta = s/r \quad (3.3)$$

It is not very convenient measuring such small angles in radians, so we convert to arc seconds, so converting radian in to arc sec. As we know that, there are  $2\pi$  radians in a complete circle, so that there are  $360 \text{ deg} / 2\pi \text{ radian} = 57.295 \text{ degree per radian}$ ,

or

$$(360 \times 60 \times 60) \text{ arc sec} / (2 \times 3.14159265) \text{ radian}$$

$$= 1,296,000 / 2\pi = 206,264.8 \text{ arcsec} / \text{radian}.$$

$$1 \text{ rad} = 206,265''$$

Applying the all above relations we can simplify the equation as,

$$\frac{71.04'' \times \text{Distance of galaxy (in parsec)}}{206264.8''/\text{radian}} = \text{Size in parsec} \quad (3.4)$$

For some of the galaxy like IRAS 07164+5301 the distance parameter is calculated from the relation  $H = v/d$ ; (Where H is Hubble constant which is taken as  $H=73 \text{ km/s/Mpc}$ ); Also where v can be calculated from the spectroscopic observations from the  $v=d\lambda/\lambda$ ; Applying these we could get the distance of the galaxy IRAS 07164+5301; where this particular galaxy distance information is not available in the literature.

### 3.5 Calculation of flux in IRAS 07164+5301

Since this galaxy is highly red shifted, the continuum subtraction results with null. In this case, we have calculated  $H\alpha$  luminosity through the spectroscopy method. As we have mentioned already in Sec. 4.2 the spectroscopic observations

made through the slit width of ( $1.''92 \times 11'$ ).

Step 1:

$H\alpha$  flux = 279 ( from the table)

$$=(279/100) \times F(H\beta)$$

$$=(279/100) \times 1.273 \times 10^{-14}$$

$$=3.55167 \times 10^{-14} \text{ergs}^{-1} \text{sec}^{-1} \text{cm}^{-1}$$

Step 2:

5.2" is the aperture size which is used for the spectrum extraction for the galaxy IRAS 07164+5301.

Hence, area covered by the spectra is =  $5.2'' \times 1.''92$

$$= 9,984 \text{ arc sec}^2$$

Step 3:

IRAS 07164+5301 galaxy frame is taken to determine the completely covered aperture radius That is taken as 41 pixel.

So, the area covered by the aperture for the whole galaxy is

$$= \pi \times r^2$$

$$= \pi \times 41^2 (\text{pixel})^2$$

$$= 3.14 \times 41^2 \times (0.296)^2 (\text{pixel})^2 \times (\text{arcsec}/\text{pixel})^2$$

$$= 462.467 \text{ arcsec}^2$$

So, from the above relations, by knowing the slit width area we know the  $H\alpha$  flux from the spectrum then by knowing total area of galaxy, what will be the flux ; It can be calculated as,

$$= \sim (3.55 \times 10^{-14}(\text{flux unit})/9.984(\text{arcsec}^2)) \times 462.47 \text{ arcsec}^2$$

$$= \sim 164.44 \times 10^{-14} \text{ergs}^{-1} \text{sec}^{-1} \text{cm}^{-1}$$

Then the luminosity can be calculated as,

$$L = 4\pi r^2 \times F$$

$$= 6.138 \times 10^{42}$$

### 3.6 SFR relation

To calculate the SFRs in the knots the calculated flux has to be converted in to  $H\alpha$  luminosity, using the relation

$$L_{H\alpha} = 4\pi R^2 \times F \quad (3.5)$$

where  $R$  is the luminosity distance taken from NASA/Extra galactic data base and  $F$  is the Flux of the knots. The calibration for starbursts is that derived by Kennicutt(1988). We have used this calibration to estimate the SFR for the listed galaxies from  $H\alpha$  image. In this way, the SFR is calculated for the all above mentioned galaxies using the expression: [Calzetti et al. \(2007\)](#)

$$\text{SFR}_{H\alpha} [\text{M}_{\odot} \text{yr}^{-1}] = 5.3 \times 10^{-42} L_{H\alpha} [\text{erg s}^{-1}]. \quad (3.6)$$

The above mentioned SFR expressions are valid for  $T_e=10^4$  and case B recombination, i.e., all the ionizing photons are processed by gas. The Luminosity of  $H\alpha$  has been corrected for underlying stellar absorption and interstellar dust attenuation (Kennicutt et al.1994). This transformation has been computed for solar metallicity and the saltpeter(1995) IMF with the lower and upper mass

cutoffs of 0.1 and 100  $M_{\odot}$  respectively. The equation also assumes that no Lyman-continuum photons are absorbed by dust. This conversion factor between ionizing flux and the SFR is usually computed using an evolutionary synthesis model. The  $H\alpha$  luminosity of the star forming knots was estimated using the measured  $H\alpha$  flux after correcting it for underlying stellar absorption and reddening.

### 3.7 Narrow band $H\alpha$ photometry

The R-band and the continuum-subtracted  $H\alpha$  images of all galaxies are shown in Figures 1 to 7. We used the continuum-subtracted  $H\alpha$  images to identify the star-forming (SF) regions (knots) within each galaxy. The knots were identified by visual inspection, but a threshold of 4-5 times sigma of background was also taken as the identification criteria. The corresponding identity number for each SF region is included in Fig. 1 to 7. We used the continuum-subtracted  $H\alpha$  image (Fig.1 to 7) to estimate the  $H\alpha$  flux of each SF knot for each galaxy. We used the continuum-subtracted  $H\alpha$  image (right panels in Fig. 3.1 to 3.14) to estimate the  $H\alpha$  flux of each SF knot for each galaxy.  $H\alpha$  fluxes have been corrected for extinction assuming:

$$A_{H\alpha} = 1.758/0.692E(B - V) = 2.54E(B - V) \quad (3.7)$$

following López-Sánchez & Esteban (2008). Here  $E(B - V)$  is the intrinsic and foreground extinction, as listed in Table 2.2 (Galactic extinction) and Table 5.3 (intrinsic extinction). The measured  $H\alpha$  flux is contaminated by flux of [N II]  $\lambda\lambda$  6548,6584 emission. The estimation of the [N II] contribution was derived using our spectroscopic values, just applying

$$F_{H\alpha,cor} = F_{H\alpha} \times \frac{H\alpha_{sp}}{[NII] 6548_{sp} + H\alpha_{sp} + [NII] 6583_{sp}}. \quad (3.8)$$

We didn't consider the transmittance of the narrow-band filter in the position of the [N II] lines –as it is explained in LSE08– because of the relatively large FWHM ( $\gtrsim 100 \text{ \AA}$ ) of the narrow-band filter used. The corresponding [N II] contribution was found between the 3% (NGC 4861) and 36% (NGC 3003). The final  $H\alpha$  fluxes corrected for both extinction and [N II] contribution derived for each SF region with all our sample galaxies are compiled in Table 3.2. Using the  $H\alpha$  fluxes and considering the distance to the galaxies listed in Table 2.2, we derived the total  $H\alpha$  luminosity for the analyzed SF regions within our WR galaxy sample. The results are also listed in Table 3.2.

The  $H\alpha$  luminosity can be used as a good tracer of star formation activity in galaxies (e.g., Kennicutt 1998; Calzetti et al. 2007). The radiation from the young stars ionizes the surrounding hydrogen gas, giving rise to  $H\alpha$  emission by recombination. Since the  $H\alpha$  luminosity is proportional to the number of ionizing photons produced by the hot stars (which is also proportional to their birth rate), the SFR can be easily derived from the  $H\alpha$  luminosity. Only stars with masses  $> 10 M_{\odot}$  and life time  $< 20 \text{ Myr}$  contribute significantly to the integrated ionizing flux, so the emission lines provide a nearly instantaneous measure of the SFR, independent of the previous star formation history.

Following the multi-wavelength analysis of the SFR within WR galaxies presented by López-Sánchez (2010), we used the conversion relation between the SFR and  $H\alpha$  luminosity given by Calzetti et al. (2007), (see Eq. 3.6) We also compile the  $H\alpha$ -based SFR values for star-forming knots observed in our WR galaxy sample in Table 3.2. Since this galaxy IRAS 07164+5301 has a larger redshift than the other objects (it has a radial velocity of  $12,981 \text{ km s}^{-1}$ , which means a redshift of  $z \sim 0.0433$ ), the continuum subtraction results with null. In this case, we estimated its  $H\alpha$  luminosity through our spectroscopy data. Considering the size and width of the slit used to get the spectrum of this galaxy ( $1.92' \times 5.2'$ , see Table 4.2) and the corresponding angular size of the galaxy, we

estimate a flux of  $\sim 1.64 \times 10^{-12} \text{ erg s}^{-1} \text{ cm}^{-2}$ , which is the value tabulated in Table 3.2. Hence, its total SFR is  $\text{SFR}_{\text{H}\alpha} \sim 7.76 M_{\odot} \text{ yr}^{-1}$ .

### 3.8 Ages of the most recent star-forming event

We estimated the age of the most-recent star forming event by using the  $\text{H}\alpha$  equivalent width,  $W(\text{H}\alpha)$ , of the star-forming knots. We used the predictions provided by the Starburst99 code (Leitherer et al. 1999), which are AGB phase corrected. We considered an instantaneous burst with Salpeter initial mass function (IMF) of 2.35. The lower and upper mass range was taken from 1 to 100. We assumed a total mass of  $10^6$ , and a metallicity of  $Z/Z_{\odot} = 0.2, 0.4$  and 1 which was chosen depending on the oxygen abundance of the galaxy derived from our spectroscopic data. The advantage of using  $W(\text{H}\alpha)$  for deriving the age of the most recent starburst event is that they provide a very small error, only between 0.1 and 0.5 Myr (López-Sánchez & Esteban 2008). Table 3.2 compiles our results. Following our  $W(\text{H}\alpha)$  data, the majority of the analyzed regions have experienced a strong star-formation event between 5 and 7 Myr ago. These values are in agreement with the presence of stars in the WR phase in them.

TABLE 3.2: H $\alpha$  flux, H $\alpha$  luminosity (corrected for extinction and [NII]) and derived star-formation rate for the knots of the WR galaxies analyzed in this work.

Knot ID	Metallicity $z(z_{\odot})$	Flux $10^{-14}$ erg s $^{-1}$ cm $^{-2}$	Luminosity $10^{38}$ erg s $^{-1}$	Log SFR $[M_{\odot}/\text{yr}]$	EW(H $\alpha$ ) [Å]	Age [Myr]	[NII] contribution
<b>NGC 1140</b>	0.008						13%
# 1.		203.36	776.38	-0.39	48	8.0 $\pm$ 1	
# 2.		2.81	10.72	-2.25	53	7.8 $\pm$ 1	
# 3.		1.18	4.52	-2.62	110	6.2	
# 4.		8.59	32.78	-1.76	122	6.1	
<b>IRAS 07164+5301</b>	0.008						30%
# 1.		164.44	14602.81	0.89	247	5.6	
<b>NGC 3738</b>	0.008						18%
# 1.		117.81	43.39	-1.64	62	7.4 $\pm$ 1	
<b>UM 311</b>	0.008						9%
# 1.		19.64	81.82	-1.36	64	7.3 $\pm$ 1	
<b>NGC 6764</b>	0.02						32%
# 1.		11.10	129.58	-1.16	6	12.5	
# 2.		243.24	2839.31	0.18	18	8.4 $\pm$ 1	
# 3.		9.10	106.17	-1.25	12	9.9	
<b>NGC 4861</b>	0.004						3%
# 1.		223.24	582.63	-0.51	312	6.0	
# 2.		1.12	2.93	-2.81	525	5.4 $\pm$ 1	
# 3.		0.37	0.97	-3.29	75	8.5 $\pm$ 1	
# 4.		1.15	3.01	-2.80	1065	4.7 $\pm$ 1	
# 5.		0.40	1.04	-3.26	81	8.3 $\pm$ 1	
# 6.		0.35	0.90	-3.32	99	7.8 $\pm$ 1	
# 7.		0.81	2.11	-2.95	216	6.4	
# 8.		0.64	1.68	-3.05	178	6.6 $\pm$ 1	
# 9.		0.44	1.15	-3.21	206	6.4	
# 10.		0.24	0.62	-3.48	247	6.3	
# 11.		0.31	0.82	-3.36	228	6.3	
# 12.		1.10	2.87	-2.82	476	5.6	
<b>NGC 3003</b>	0.02						36%
# 1.		0.23	1.58	-3.08	110	6.3	
# 2.		0.31	2.12	-2.95	135	6.1	
# 3.		10.52	72.18	-1.42	12	1.3	
# 4.		0.17	1.17	-3.21	82	6.5	
# 5.		0.90	6.20	-2.48	264	5.5	
# 6.		0.77	5.28	-2.55	123	6.2	
# 7.		0.16	1.13	-3.22	106	6.3	
# 8.		0.33	2.25	-2.92	240	5.6	
# 9.		0.47	3.21	-2.77	173	5.9	
# 10.		0.38	2.63	-2.86	321	5.4	
# 11.		0.36	2.45	-2.89	151	6.0	
# 12.		1.30	8.91	-2.33	129	6.2	
# 13.		14.66	100.59	-1.27	20	1.1	
# 14.		0.45	3.08	-2.79	48	8.1 $\pm$ 1	
# 15.		2.89	19.80	-1.98	63	7.4	
# 16.		0.54	3.72	-2.71	143	6.1	
# 17.		0.24	1.67	-3.05	159	6.0	
# 18.		3.23	22.18	-1.93	42	8.6	
# 19.		0.66	4.54	-2.62	79	6.5 $\pm$ 1	
# 20.		0.45	3.07	-2.79	79	6.5 $\pm$ 1	
# 21.		0.73	5.01	-2.58	61	7.4 $\pm$ 1	
# 22.		1.83	12.56	-2.18	110	6.3	
# 23.		0.57	3.94	-2.68	240	5.6	
# 24.		0.86	5.88	-2.51	225	5.7	
# 25.		0.25	1.71	-3.04	200	5.8	



# Chapter 4

## Oxygen abundances

### 4.1 Introduction

The Oxygen abundances is estimated through the help of spectroscopic observations of the star forming galaxies. These abundances are relatively easy to measure in star-forming galaxies because they contain gas clouds in which large numbers of hot stars are embedded. Their spectra are dominated by nebular emission lines similar to those of high-excitation giant H II regions in late type spiral galaxies. Abundance gradients in disk galaxies are the result of the formation of many generations of stars which are gradually deplete the gas fraction of the disk while at the same time chemically enriching the ISM by ejecting their nucleosynthetic products at the end of their lives (Kunth & Östlin 2000). Metallicity of a galaxy is determined by its oxygen abundance. The preferred method for determining oxygen abundance in H II regions of galaxies is through electron temperature sensitive lines such as the [O III]  $\lambda$  4363 line (the so called Te method Pilyguin 2003, Kennicutt et al. 2003). However, in absence of [O III]  $\lambda$  4363 line, the alternative empirical relations, such as R23 method (McGaugh 1991, hereafter M91), N2 method, O3N2 method (Pettini & Pagel 2004, hereafter PP04), N2O2 method (Kewley & Dopita 2002, hereafter KD02), which uses the

strong emission lines (recombination and forbidden), to determining the oxygen abundance. As the brightest metallic lines observed in spectra of H II regions are those involving oxygen, this element has been extensively used to get a suitable empirical calibration.

The strength of forbidden emission lines varies according to the electron temperature within the H II region. Metal ions of oxygen, sulfur, and nitrogen act as coolants that reduce the mean kinetic energy (temperature) of the electron gas by removing energy from the region. Metal ions such as [O II] and [O III] effectively cool an H II region because the excitation potentials of their low-lying levels are on the order of  $kT$ , leaving them susceptible to collisional excitation. Some time after being collisionally excited, an ion de-excites and emits a photon. This photon then escapes the H II region, carrying away its kinetic energy and reducing the overall electron temperature of the gas. In this way, metal ions make a significant contribution to radiative cooling despite their low abundances (Osterbrock & Ferland 2006).

## 4.2 Observations

Spectroscopic observation of the galaxies are obtained with a combination of slit 1671 (slit width  $1''.92 \times 11'$ ) and Grism 7, covering a wavelength range 3500 Å–7500 Å. This slit and grism combination gives a dispersion of  $1.5 \text{ \AA}/\text{pixel}$  and a spectral resolution of  $\sim 11 \text{ \AA}$ . As we used the HFOSC instrument at the 2m HCT for the majority of our spectroscopic observations, the spatial scale is  $0.296''/\text{pixel}$ . The star-forming regions were identified using short exposures through the H $\alpha$  filter and it was centered through the slit. Spectrophotometric standard star is observed through Grism 7 with broad slit 1340 ( $15''.41 \times 11'$ ), for flux calibration of the spectrum. A log of our observations is given as below.

TABLE 4.1: Low Resolution Spectroscopic Observations

Galaxy Name	Date	Spectrum [Sec]	Telescope
NGC 1140	05/12/2007	1900	HCT
IRAS 07164+53010	15/02/2010	900	HCT
NGC 3738	15/02/2010	1500	HCT
UM 311	16/02/2010	1800	HCT
NGC 6764	11/07/2011 <sup>a</sup>	1200	HCT
NGC 6764(knot#1)	31/10/2008 <sup>b</sup>	3000	HCT
NGC 4861	01/02/2011	1800	HCT
NGC 3003	20/01/2012	2×1200	HCT

<sup>a</sup>: The spectrum was taken in nuclear region and shows a clear AGN feature.

<sup>b</sup>: The spectrum was taken in region #1 (see Fig. 3.9).

The spectroscopic data analysis was also done using standard routines of the IRAF software. For each two-dimensional spectra, we extracted an one-dimensional spectrum integrating a particular region, usually centered on the brightest point of the galaxy, along the spatial direction. We carefully checked that the one-dimensional spectrum obtained for each object had the optimal signal-to-noise. Each 1-D spectrum is then wavelength calibrated using a FeAr arc spectrum. The absolute flux calibration of the spectra was achieved by observing spectrophotometry standard stars chosen from Oke (1990). We also corrected the spectra for foreground extinction using the Galactic  $E(B - V)$  values listed in Table 2.2.

### 4.3 Reddening Correction

In the visible part of the spectrum the dust is generally evidenced by its blocking of light which is coming from the stars and galaxies. The blocking arises from two processes, scattering and absorption. In scattering, the incoming photon is not destroyed, but its direction is changed. In absorption, the incoming photon is destroyed, with its energy remaining in the dust grain. The combined effects

of scattering and absorption are called interstellar extinction. The observed extra galactic spectrum is extinguished because of two effects foreground extinction (interstellar extinction) and intrinsic extinction (because of dusty regions within the host galaxy). These reddening can be corrected C(C(H $\beta$ )) method. It is described as follows:

### 4.3.1 C(H $\beta$ ) through reddening Correction

The reddening coefficient,  $c(H\beta)$ , was derived from the Balmer decrement. However, in extragalactic objects the fluxes of nebular Balmer lines may be affected by absorption produced by the underlying stellar population (mainly B and A stars). We performed a procedure to derive simultaneously the reddening coefficient and the equivalent widths of the absorption in the hydrogen lines,  $W_{abs}$ , to correct the observed line intensities for both effects. It is assumed that  $W_{abs}$  is the same for all the Balmer lines and used the relation given by Mazzarella & Boronson (1993) to perform the absorption correction

$$c(H\beta) = \frac{1}{f(\lambda)} \log \left[ \frac{\frac{I(\lambda)}{I(H\beta)} \times \left( 1 + \frac{W_{abs}}{WH\beta} \right)}{\frac{F(\lambda)}{F(H\beta)} \times \left( 1 + \frac{W_{abs}}{W\lambda} \right)} \right] \quad (4.1)$$

for each detected hydrogen Balmer line, where  $F(\lambda)$  and  $I(\lambda)$  are the observed and the theoretical fluxes (unaffected by reddening or absorption),  $W_{abs}$ ,  $W\lambda$ , and  $WH\beta$  are the equivalent widths of the underlying stellar absorption, the considered Balmer line and  $H\beta$ , respectively, and  $f(\lambda)$  is the reddening curve normalized to  $H\beta$  using the Cardelli et al. (1989) law. We always considered the theoretical ratios of these pairs of H I Balmer lines expected for case B recombination given by Storey & Hummer (1995) as suming the electron temperature and density computed independently for each region. Using three different Balmer lines (i.e.,  $H\alpha$ ,  $H\beta$ , and  $H\gamma$ ), a unique value for  $c(H\beta)$  and  $W_{abs}$  is computed.

However, in the case of the use of four or more Balmer lines, several solutions are derived, so we considered the values that provide the closest match between the corrected and the theoretical Balmer line ratios as representative of the region (López-Sánchez & Esteban 2009).

## 4.4 R23 indicator

In this analysis, we use the forbidden line fluxes for [O II] and [O III] to determine the metallicity of a star-forming region, as proposed by McGaugh (1991). There are several steps in this process. First, we must determine the theoretical oxygen abundance of each region using the observed oxygen emission lines [O II] and [O III]. We then use our calculations of model oxygen abundance to derive the overall metallicity of each region. We use the metallicity indicator R23 to calculate the relative strength of oxygen emission to H $\beta$  emission. The R23 expression is given by

$$\text{R23} = ([\text{O II}] + [\text{O III}]) / \text{H}\beta$$

where [O II], [O III] and H $\beta$  are the extinction corrected line fluxes for wavelengths 3727Å, 4959Å and 5007Å, and 4861Å, respectively. Fig. 4.1 shows the model relationship between the oxygen abundance, log(O/H), and R23, as proposed by McGaugh (1991, 94) and Kobulnicky (1999). The upper branch in Figure represents conditions in the most metal-rich H II regions. R23 is a minimum where the model oxygen abundance is greatest, [12+log(O/H)]  $\sim$ 9.1. Here, the high metal abundance produces efficient cooling in the H II region, reducing the electron temperature and suppressing further collision events. As a result, the [O II] and [O III] emission lines are absent from the spectrum, or weak, at best. Further toward the right, R23 reaches its maximum as the oxygen abundance decreases to [12+log(O/H)]  $\sim$ 8.4. Here, fewer metals are available to cool the region, and collisions occur more frequently, leading to strong, observable emission lines of [O II] and [O III].

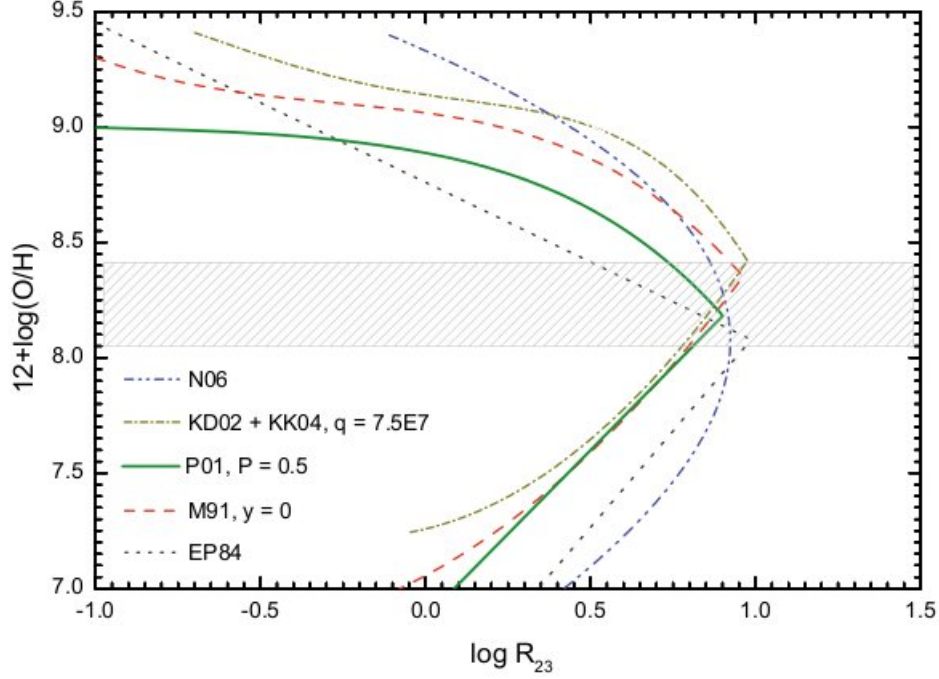


FIGURE 4.1: Image credit: Lopez 2010 et al. Empirical calibrations of oxygen abundance using the R23 parameter. Note that they are bi-valuated. The dashed zone indicates the region with higher uncertainties in O/H. The empirical calibrations plotted in the figure are: EP94: Edmunds & Pagel (1984); M91: McGaugh (1991) using  $y = 0$  ( $R2 = R3$ ); P01: Pilyugin (2001) using  $P = 0.5$  ( $R2 = R3$ ); (KD02+KK04): Kewley & Dopita (2002) using the formulation of Kobulnicky & Kewley (2004) assuming  $q = 7.5 \times 10^7 \text{ cm s}^{-1}$ ; N06: Nagao et al. (2006) using their cubic fit to R23. (See Appendix.C for more )

The maximum value for R23 also represents a turnaround in the model relationship. R23 steadily decreases as smaller numbers of metal ions are present in the region. This trend in R23 continues to zero as the diminishing population of metal ions produce weaker, less observable emission lines. In abundance calculations, using the polynomial equations for the curves in Fig. 4.1 shown (Kobulnicky 1999):

LOWER BRANCH:

$$12 + \log(O/H)_{\text{lower}} = 12 - 4.944 + 0.767x + 0.602x^2 - y(0.29 + 0.332x - 0.331x^2) \quad (4.2)$$

UPPER BRANCH:

$$12 + \log(O/H)_{upper} = 12 - 2.939 - 0.2x - 0.237x^2 - 0.305x^3 - 0.0283x^4 \\ - y(0.0047 - 0.0221x - 0.102x^2 - 0.0817x^3 - 0.00717x^4) \quad (4.3)$$

where

$$x = \log(R23) \quad (4.4)$$

and

$$y = \log(O32) = \log(O \text{ III}4959,5007)/O \text{ II}3727$$

The ionization parameter,  $\log(O32)$ , describes the relative number of  $[O \text{ III}]$  to  $[O \text{ II}]$  ions within the region. It is also a measure of the number density of ionizing photons. The O32 parameter has a different effect on each branch of the model. In the upper branch, a smaller O32 ratio slightly reduces the model oxygen abundance for a given R23. The O32 ratio has a greater and more uniform effect on the lower branch, where a smaller ratio indicates a higher model oxygen abundance of about 1% for any value of R23. To determine the oxygen abundance for each region in galaxies, we must know beforehand which model branch (lower or upper) to use in our calculations. The lower and upper model branches correspond to Eq. 4.2 and Eq. 4.3, respectively. Here, we use the ratio  $[N \text{ II}]/O \text{ II}$  to indicate the appropriate branch. H II regions in high surface-brightness galaxies generally have  $\log([N \text{ II}]/O \text{ II})^3 > 1$ . These bright H II regions are metal rich, while H II regions in low surface-brightness galaxies are usually metal poor (McGaugh 1991). The other empirical relations used to derive the oxygen abundances are listed in Appendix:C

## 4.5 Optical Spectra of analyzed WR Galaxies

The spectrum of galaxies are as follows:

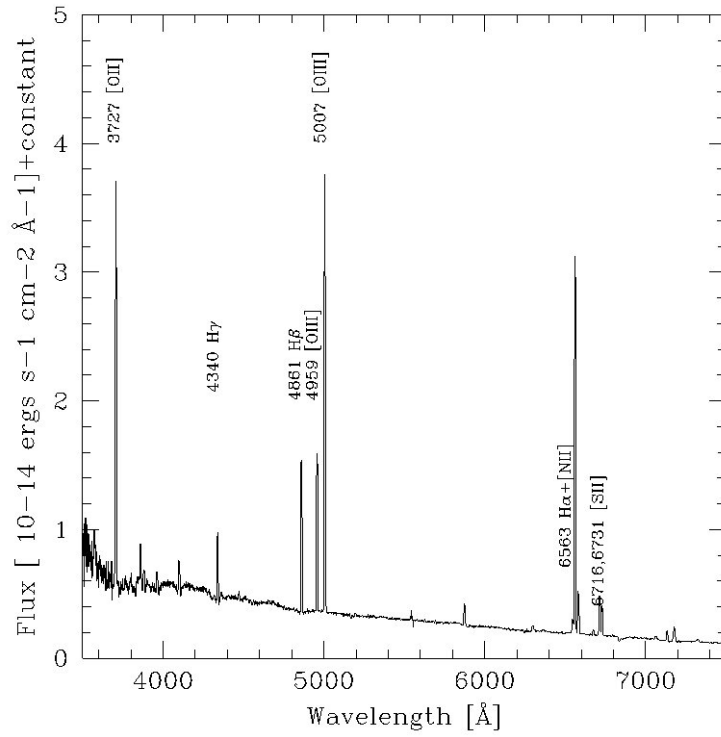


FIGURE 4.2: Spectrum of the galaxy NGC 1140

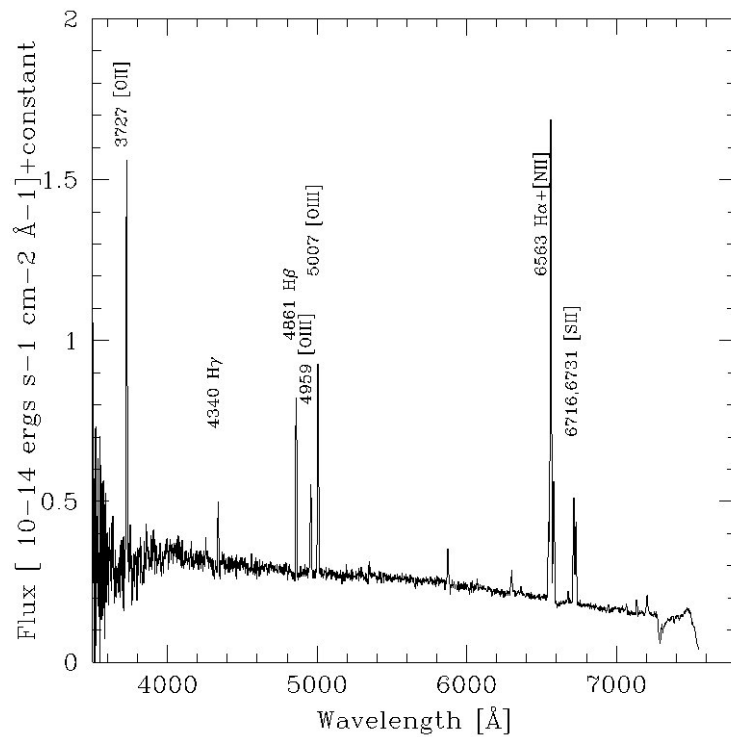


FIGURE 4.3: Spectrum of the galaxy IRAS 07164+5301

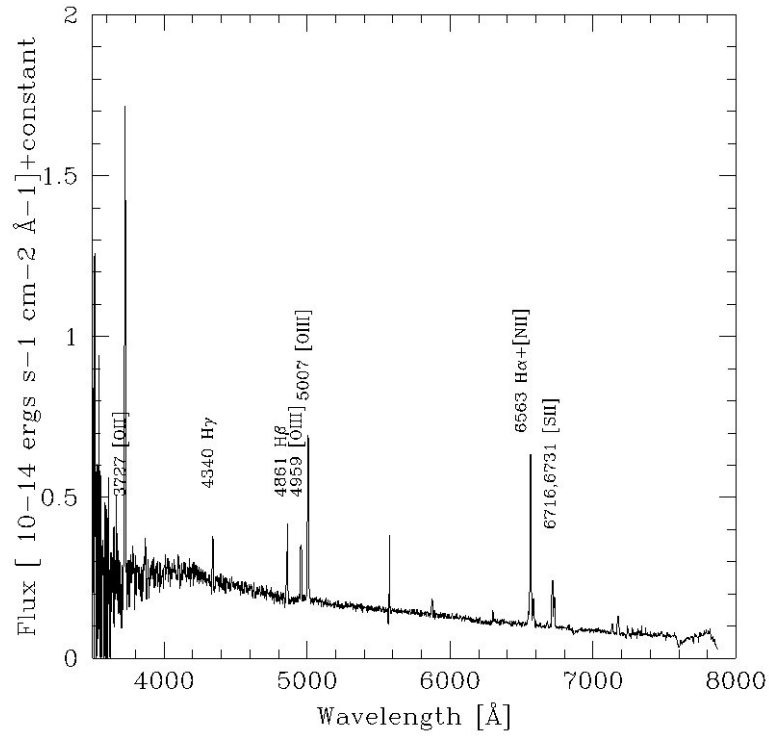


FIGURE 4.4: Spectrum of the galaxy NGC 3738

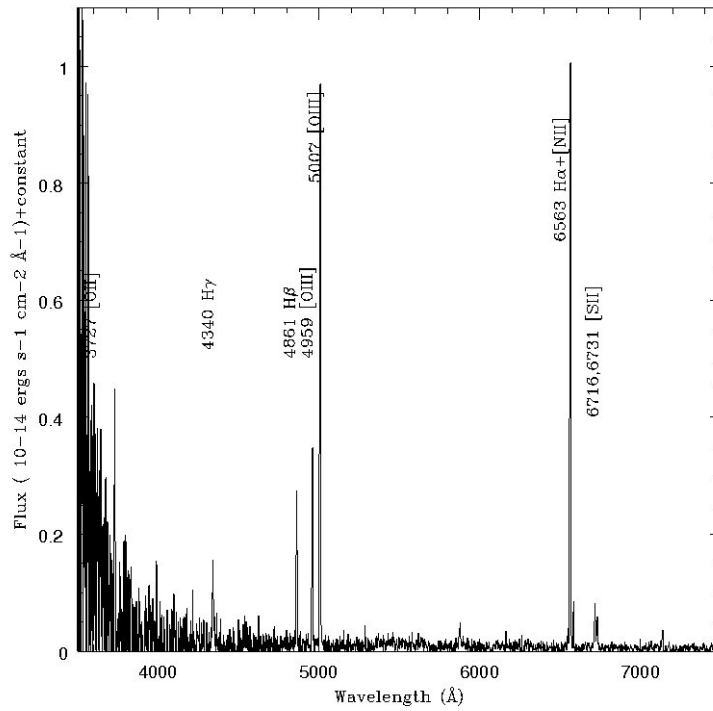


FIGURE 4.5: Spectrum of the galaxy UM 311

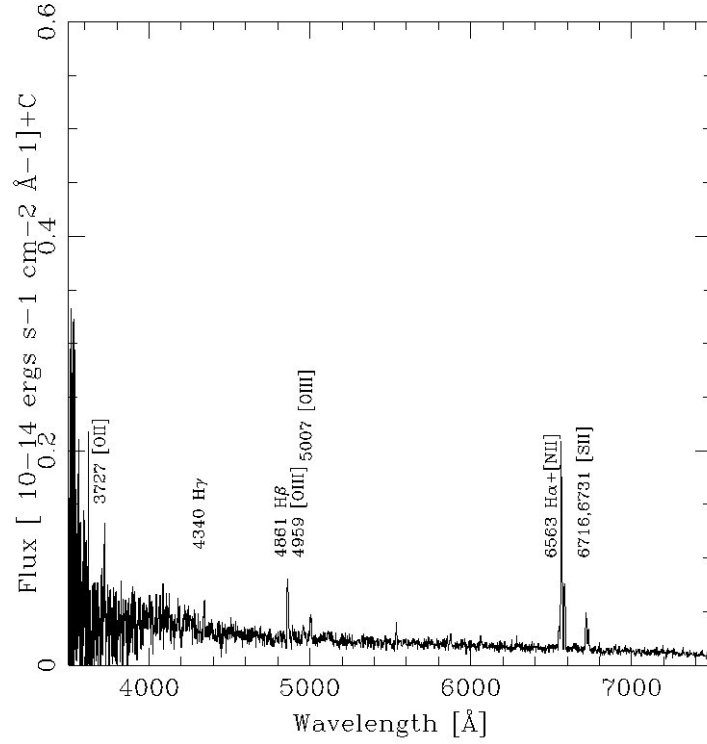


FIGURE 4.6: Spectrum of knot region ID:1 of the galaxy NGC 6764

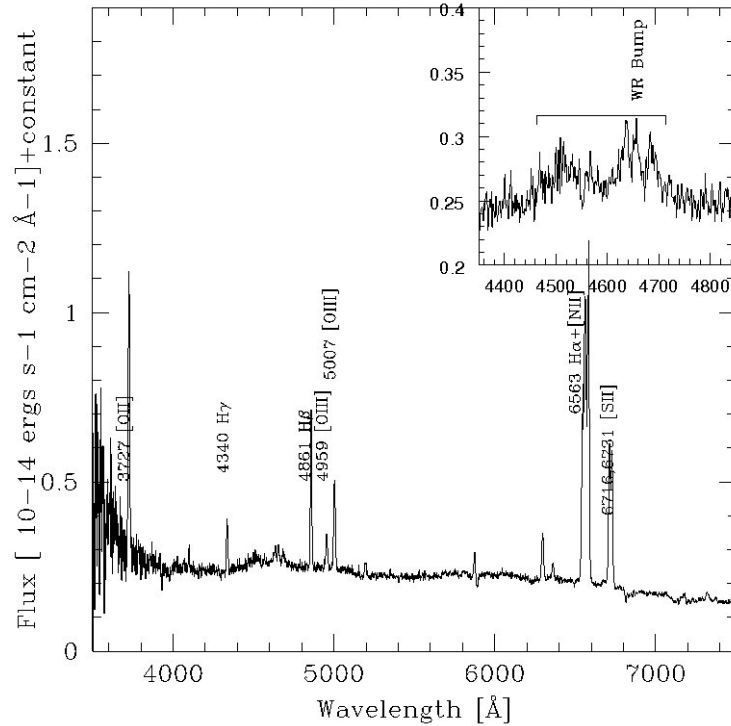


FIGURE 4.7: Spectrum of central region of the galaxy NGC 6764

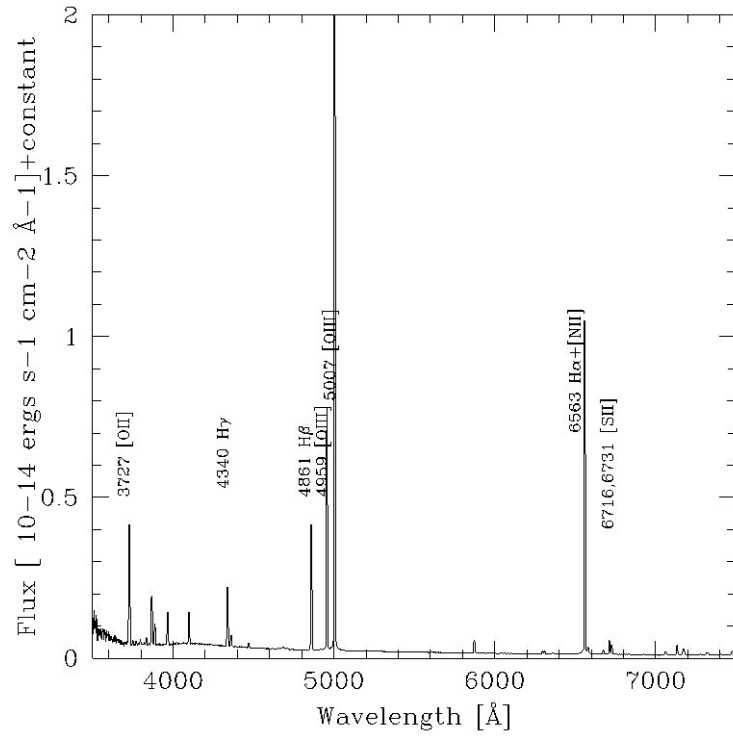


FIGURE 4.8: Spectrum of the galaxy NGC 4861

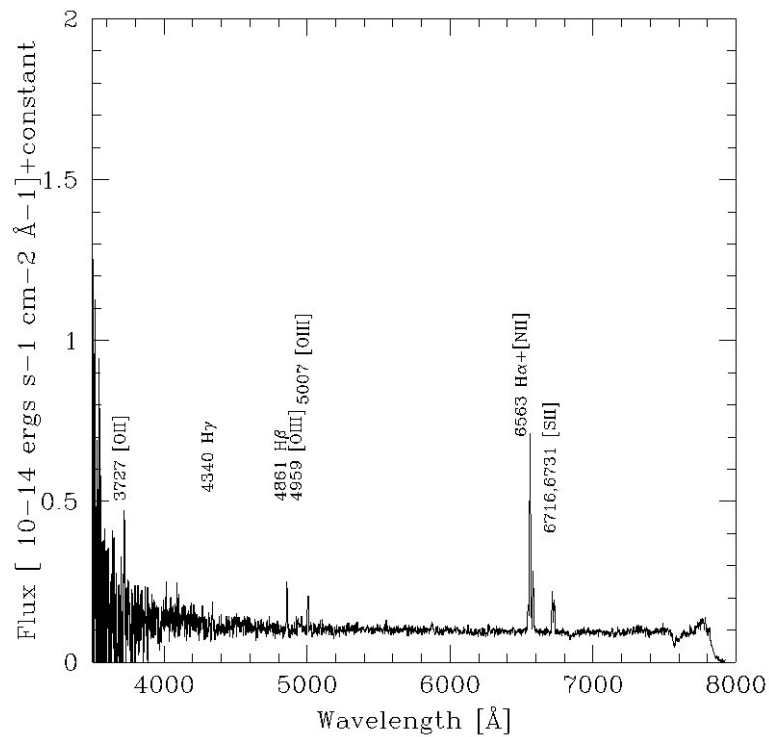


FIGURE 4.9: Spectrum of the galaxy NGC 3003

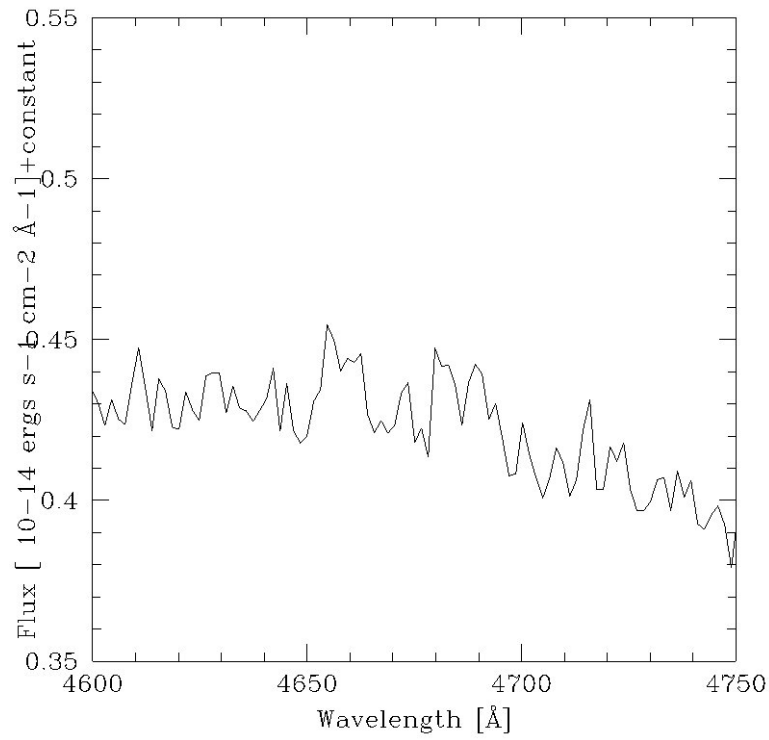


FIGURE 4.10: WR Blue bump spectrum of the galaxy NGC 1140

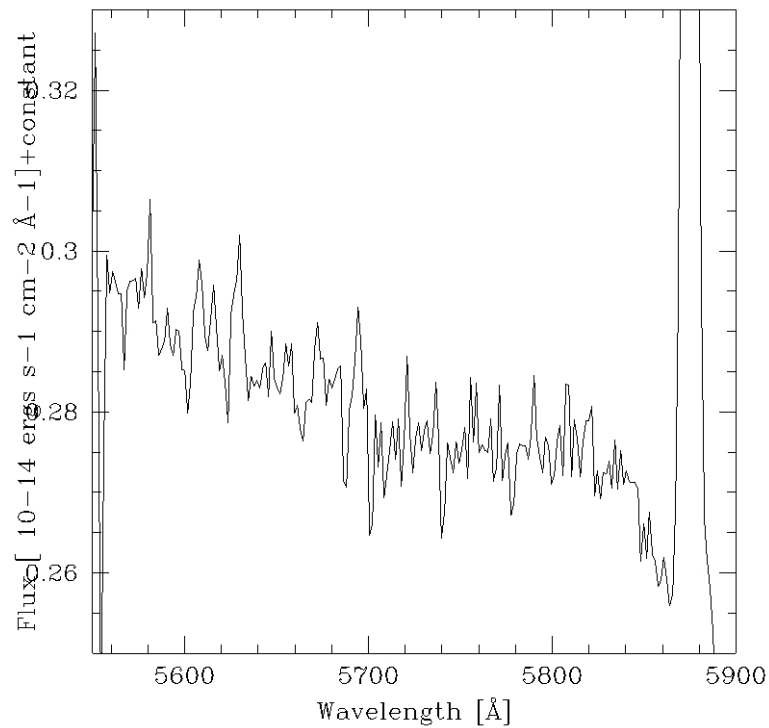


FIGURE 4.11: WR red bump spectrum of the galaxy NGC 1140

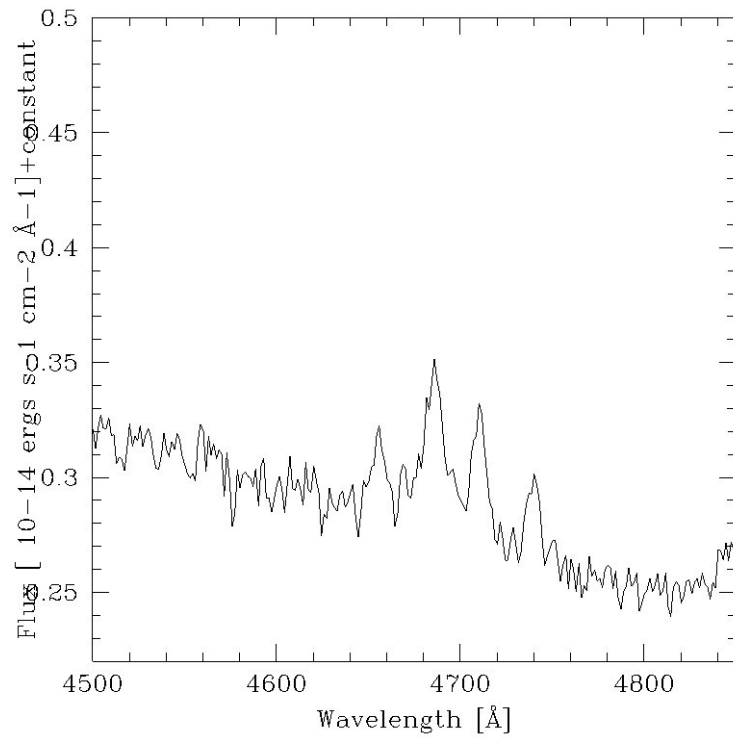


FIGURE 4.12: WR Blue bump spectrum of the galaxy NGC 4861

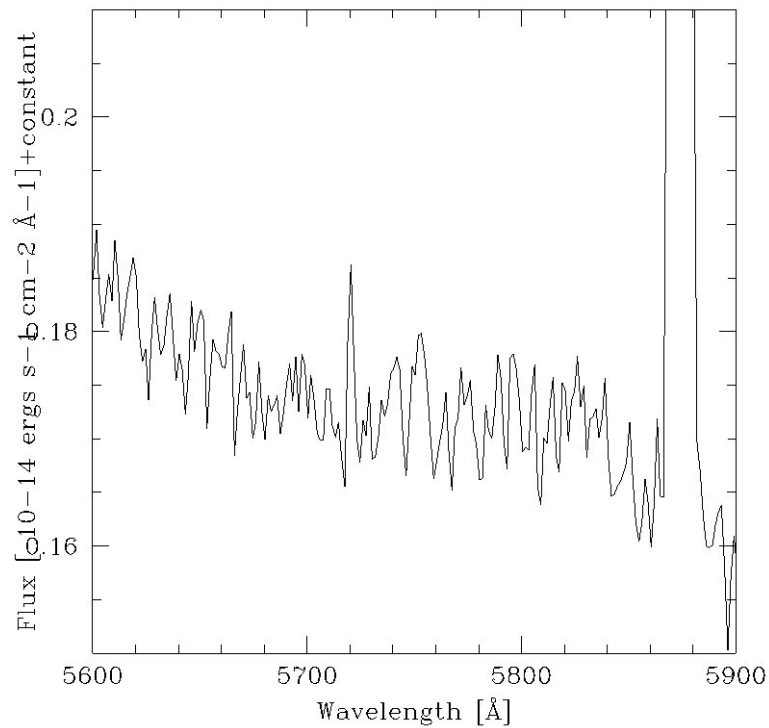


FIGURE 4.13: WR Red bump spectrum of the galaxy NGC 4861

## 4.6 Results from optical spectroscopy

The one-dimensional spectra obtained for our WR galaxy sample are plotted in Figs. 4.2 to 4.9. The prominent lines have been identified and marked in the spectra. These are emission lines from the hydrogen and helium Balmer series, and forbidden emission lines due to oxygen, nitrogen and sulphur. These spectra have been corrected for foreground (Galactic) extinction using the corresponding  $E(B - V)$  values extracted from Schlegel et al. (1998) (see Table 2.2) and by making use of the IRAF deredden task.

Line intensities and equivalent widths were measured by integrating all the flux in the line between two given limits and over a local continuum estimated by eye. In the cases of line blending (usually, in the  $H\alpha + [N II]$  region), a multiple Gaussian profile plotting procedure was applied to obtain the line flux of each individual line. We used the standard assumption, i.e., that  $I(H\beta) = 100$ , to compute the line intensity ratios.

The results obtained for each galaxy are compiled in Table 4.2. These data have been corrected for both internal reddening and underlying stellar absorption following the method described in López-Sánchez & Esteban (2009). The reddening curve normalized to  $H\beta$ ,  $f(\lambda)$ , shown in Table 4.2 considers the Cardelli, Clayton & Mathis (1989) extinction law. We always considered the theoretical ratios of the pairs of H I Balmer lines expected for case B recombination given by Storey & Hummer (1995) assuming the derived electron temperature (in the case of NGC 1140 and NGC 4861) or using the derived oxygen abundance (see below) and the expected electron temperature for these values, following Tables 2 and 3 in López-Sánchez & Esteban (2010b).

TABLE 4.2: Dereddened line intensity ratios with respect to  $I(\text{H}\beta)=100$  for the galaxies analyzed in this work. We also compile the  $\text{H}\beta$  flux, the size of the extracted area, the reddening coefficient,  $c(\text{H}\beta)$ , and the equivalent widths of the absorption in the hydrogen lines,  $W_{abs}$ , used to correct the spectra for internal reddening, and the equivalent widths of the emission H I Balmer lines.

Line	$f(\lambda)$	NGC1140	IRAS07164+5301	NGC 3738	UM 311	NGC 6764	NGC 4861	NGC 3003
[O II] 3728	0.322	241±17	238±28	680±110	257±90	142±44	88.3±5.8	209±65
[Ne III] 3869	0.291	21.9±3.9		41:			37.0±2.5	
[Ne III] 3969+H7	0.267	10.2±1.1					26.5±2.1	
H $\delta$ 4101	0.230	26.2±2.1		27:			26.0±1.7	
H $\gamma$ 4340	0.157	47.0±3.1	43.9±7.4	49±13	35±11	50±14	47.2±2.5	47±17
[O III] 4363	0.150	1.53±0.49					9.79±0.77	
He I 4471	0.116	3.63±0.64					3.28±0.35	
[Fe II] 4658	0.059						0.93±0.26	
Broad He II 4686	0.049	3.3±1.4					2.62±0.78	
[Ar IV] 4711	0.043						1.09±0.23	
[Ar IV] 4740	0.034						0.56±0.20	
H $\beta$ 4861	0.000	100.0±3.8	100.0±5.5	100±10	100±11	100±12	100.0±3.3	100±14
[O III] 4959	-0.025	107.4±5.7	50.2±5.3	96±14	107±13	18.2±3.1	197.7±9.1	21.8±4.1
[O III] 5007	-0.037	27.4±1.3	120.2±9.8	257±31	270±16	38.6±4.6	596±26	58.2±6.5
Broad C IV 5808	-0.191	3.34±0.35					1.23±0.37	
He I 5876	-0.203	16.8±1.3	43.9±4.8	28.0±5.2	16.1±5.6	13.8:	10.28±0.59	12.8:
[O I] 6300	-0.262	4.48±0.41	11.0±1.9	12.4±3.5			1.78±0.15	
[S III] 6312	-0.264						2.13±0.15	
[N II] 6548	-0.295	10.5±1.1	43.9±4.8	15.5±4.9	5.5:	33.8±3.9	2.55±0.32	5.2±1.1
H $\alpha$ 6563	-0.297	282±14	279±19	281±31	281±25	284±23	282±13	281±29
[N II] 6583	-0.300	30.6±1.8	75.4±6.0	44.2±6.5	28.1±2.6	102±9	7.06±0.41	103±12
He I 6678	-0.312	3.49±0.46	4.2±1.4	4.5:			3.23±0.24	
[S II] 6716	-0.318	29.2±1.7	62.0±5.1	59.2±8.4	35.9±3.9	60.2±8.5	9.90±0.53	69±11
[S II] 6731	-0.319	21.0±1.3	46.0±4.0	38.3±7.1	22.0±3.0	37.9±7.8	7.33±0.42	53±10
He I 7065	-0.364	2.44±0.60			1.7:		2.32±0.31	
[Ar III] 7135	-0.373	7.44±0.58	7.4±1.5	14.6±3.1	10.8±2.4		7.20±0.41	5.8:
$F_{\text{H}\beta}$ [ $10^{-14}$ erg cm $^{-2}$ s $^{-1}$ ]		10.01±0.39	1.273±0.072	2.08±0.22	1.89±0.15	0.655±0.055	33.8±1.1	1.31±0.16
-W(H $\alpha$ ) [Å]		172±10	76.7±4.1	53.6±4.4	814±75	109±11	757 ± 35	51±5
-W(H $\beta$ ) [Å]		85.9±7.5	9.1±0.8	13.1±1.4	376±19	22.8±2.9	136 ± 15	14.0±1.6
-W(H $\gamma$ ) [Å]		11.9±1.2	6.9±0.6	4.8±0.6	58±13	7.6±2.2	45.5 ± 2.8	5.1±2.8
-W(H $\delta$ ) [Å]		4.8±0.5		2.2:			19.1 ± 1.6	
Aperture size [arcsec]		1.92×8.18	1.92×5.2	1.92×12.3	1.92×3.4	1.92×17.6	1.92×6.2	1.92×4.1
$c(\text{H}\beta)_{\text{internal}}$		0	0.06±0.02	0	0.17±0.03	0.02±0.01	0.04±0.01	0.04±0.0
$W_{abs}$ [Å]		2.2	1.6±0.2	0	1.1±0.2	1.2±0.2	0.5±0.1	0.5±0.2

As we already corrected the spectra for foreground reddening, the obtained values of  $c(\text{H}\beta)_{\text{internal}}$  represent the intrinsic extinction within each galaxy. The values derived for the reddening coefficient,  $c(\text{H}\beta)$ , and the equivalent widths of the absorption in the hydrogen lines,  $W_{\text{abs}}$ , as well as the equivalent widths of the emission H I Balmer lines, are also listed in Table 4.2. We note that for two galaxies, NGC 1140 and NGC 3738, we assumed  $c(\text{H}\beta)_{\text{internal}}=0$  because the method gave slightly negative values for the reddening correction.

### 4.6.1 Physical conditions of the ionized gas

We first analyzed the nature of the ionization using the so-called diagnostic diagrams, as firstly proposed by Baldwin, Phillips & Terlevich (1981) and Veilleux & Osterbrock (1987). These diagnostic diagrams plot two different excitation line ratios for classifying the excitation mechanism of ionized nebulae. H II regions (or H II or star- burst galaxies) lie within a narrow band within these diagrams, but when the gas is ionized by shocks, accretion disks, or cooling flows (in the case of AGNs or LINERs) its position in the diagram is away from the locus of H II regions.

Figure 4.14 plots the typical  $[\text{O III}] \lambda 5007/\text{H}\beta$  versus  $[\text{N II}] \lambda 6583/\text{H}\alpha$  and  $[\text{O II}] \lambda 5007/\text{H}\beta$  versus  $([\text{S II}] \lambda 6716 + \lambda 6731)/\text{H}\alpha$  diagrams. We used the analytic relations given by Dopita et al. (2000) and Kewley et al. (2001) between different line ratios to check the nature of the excitation mechanism of the ionized gas within the bursts. Actually, the dividing line given by the Kewley et al. (2001) models represents an upper envelope of positions of star-forming galaxies. The left panel of Fig. 4.14 includes the empirical relation between the  $[\text{O III}] \lambda 5007/\text{H}\beta$  and the  $[\text{N II}] \lambda 6583/\text{H}\alpha$  provided by Kauffmann et al. (2003) analyzing a large data sample of star-forming galaxies from the SDSS (York et al. 2000). As we see, all analyzed regions lie below the Kewley et al. (2001) theoretical line. This clearly indicates that photoionization is the main excitation mechanism of the

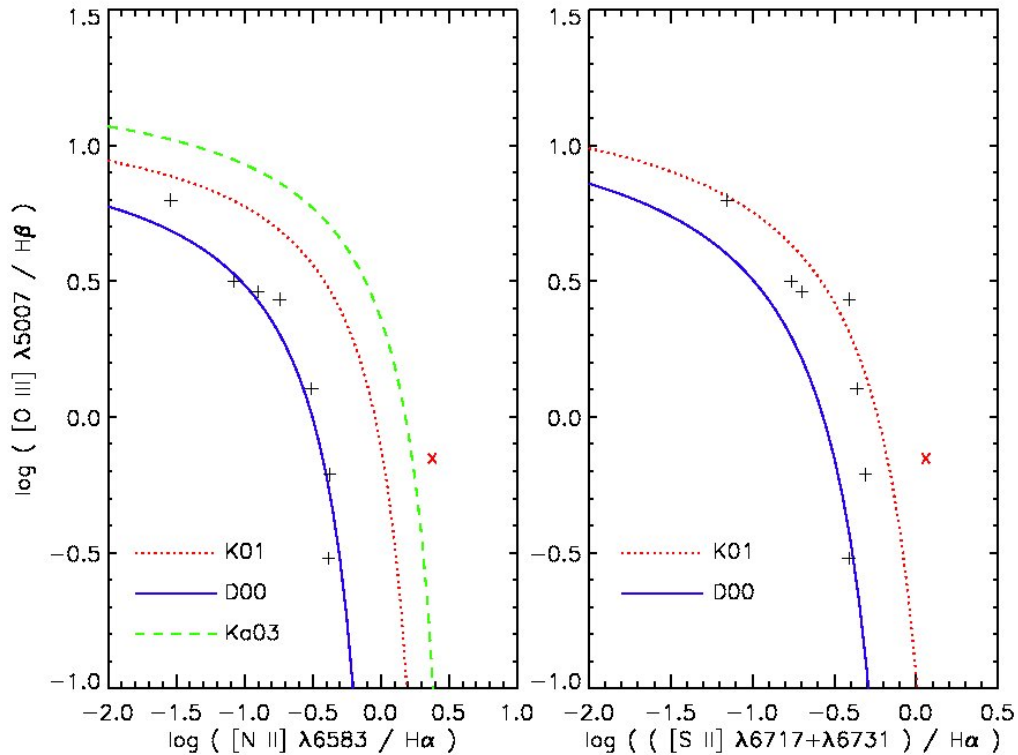


FIGURE 4.14: Comparison of some observational flux ratios obtained for all analyzed WR galaxies (black crosses) with the diagnostic diagrams proposed by Dopita et al. (2000), blue continuous line (D00), and Kewley et al. (2001), red discontinuous line (K01). The left panel also shows the empirical relation provided by Kauffmann et al. (2003) with a dotted-dashed dark yellow line (Ka03). We also plot the observed flux ratios for the center of NGC 6764 (red x), which is classified as a LINER.

gas and that there is very little evidence for a significant contribution from shock excitation. However, this is not satisfied in the case of the center of NGC 6764 (red cross in Fig. 4.14), which lies in the region occupied for LINERs. Indeed, this starburst galaxy has been classified as a classical LINER galaxy in the past (Alonso-Herrero et al. 2000).

The electron density of the ionized gas,  $n_e$ , was computed via the [S II]  $\lambda\lambda 6716, 6731$  doublet by making use of the five-level program for the analysis of emission-line nebulae included in IRAF NEBULAR task (Shaw & Dufour 1995). All regions were found in the low-density limit,  $n_e < 100 \text{ cm}^{-3}$ , and hence we adopt  $n_e = 100 \text{ cm}^{-3}$ .

TABLE 4.3: Physical conditions and chemical abundances of the ionized gas of the regions analyzed in NGC 1140 and NGC 4861.

	NGC 1140	NGC 4861
$T_e[\text{O III}]$ [K]	9500±900	14000±600
$T_e[\text{O II}]$ [K]	9700±700	12800±500
$n_e$ [cm <sup>-3</sup> ]	<100	<100
12+log(O <sup>+</sup> /H <sup>+</sup> )	8.06±0.12	7.14±0.08
12+log(O <sup>++</sup> /H <sup>+</sup> )	8.09±0.09	7.87±0.04
<b>12+log(O/H)</b>	<b>8.38±0.10</b>	<b>7.95±0.05</b>
log(O <sup>++</sup> /O <sup>+</sup> )	0.03±0.14	0.73±0.09
12+log(N <sup>+</sup> /H <sup>+</sup> )	6.82±0.06	5.90±0.05
12+log(N/H)	7.13±0.10	6.70±0.09
log(N/O)	-1.24±0.07	-1.25±0.08
12+log(S <sup>+</sup> /H <sup>+</sup> )	6.10±0.06	5.36±0.04
12+log(S <sup>++</sup> /H <sup>+</sup> )		6.16±0.09
12+log(S/H)		6.35±0.08
log(S/O)		-1.59±0.12
12+log(Ne <sup>++</sup> /H <sup>+</sup> )	7.48±0.15	7.01±0.06
12+log(Ne/H)	7.16±0.19	7.09±0.10
log(Ne/O)	-0.61±0.16	-0.86±0.06
12+log(Ar <sup>++</sup> /H <sup>+</sup> )	5.89±0.10	5.52±0.06
12+log(Ar <sup>+3</sup> /H <sup>+</sup> )		4.78±0.11
12+log(Ar/H)	5.73±0.18	5.60±0.06
log(Ar/O)	-2.65±0.21	-2.35±0.11

The electron temperature of the ionized gas was computed for only two galaxies: NGC 1140 and NGC 4861, as only in these two cases we detect the faint auroral [O III]  $\lambda$ 4363 emission line. We therefore inferred  $T_e([\text{O III}])$  from the [O III] ( $\lambda$ 4959+ $\lambda$ 5507)/ $\lambda$ 4363 ratio by making use of the IRAF NEBULAR task. As we assumed a two-zone approximation to define the temperature structure of the nebula, we used  $T_e([\text{O III}])$  as representative of high-ionization potential ions. The electron temperature assumed for the low-ionization potential ions was derived from the linear relation between  $T_e([\text{O III}])$  and  $T_e([\text{O II}])$  provided by Garnett (1992). The results are listed in Table 4.3.

#### 4.6.2 Estimation of the chemical abundances

The preferred method for determining oxygen abundances in galaxies using H II regions is through electron temperature sensitive lines such as the [O III]  $\lambda$ 4363 line, the so-called  $T_e$  method (Peimbert & Costero 1969; Stasińska 1978; Esteban et al. 2004). However, in absence of [O III]  $\lambda$ 4363 line, the alternative empirical relations, such as  $R_{23}$  method (McGaugh 1991, hereafter M91),  $R_{23} - P$  method

(Pilyugin 2001a,b; Pilyugin & Thuan 2005; Pilyugin et al. 2010),  $N_2O_2$  method (Kewley & Dopita 2002, hereafter KD02), which use the strong emission lines, can be used for determining oxygen abundance. However, the use of these empirical methods must be done carefully; see recent reviews by López-Sánchez & Esteban (2010b) and López-Sánchez et al. (2012).

In our case, we can only derive the oxygen abundances of the ionized gas following the  $T_e$  method for two galaxies: NGC 1140 and NGC 4861. We followed the prescriptions explained in López-Sánchez & Esteban (2009) to compute the O, N, S, Ar and Ne abundances, and the N/O, S/O, Ar/O and Ne/O ratios, for the ionized gas within these two galaxies. The results are compiled in Table 4.3. We note that we used an updated atomic dataset for  $O^+$ ,  $S^+$ , and  $S^{+2}$  for NEBULAR. The references are indicated in Table 4 of García-Rojas et al. (2005).

We derive oxygen abundances –in units of  $12+\log(O/H)$ – of  $8.38\pm 0.10$  and  $7.95\pm 0.05$  for NGC 1140 and NGC 4861, respectively, being their associated N/O ratios –in units of  $\log(N/O)$ –  $-1.24\pm 0.07$  and  $-1.25\pm 0.08$ , respectively. The N/O ratio computed in NGC 1140 agrees with that expected for its O/H (e.g., Izotov & Thuan 1999; Izotov et al. 2004; López-Sánchez & Esteban 2010b). However, the N/O ratio derived in NGC 4861 is clearly higher than that expected for its oxygen abundance. We estimate this excess in the N/O ratio in NGC 4861 on  $\sim 0.3$ – $0.4$  dex. The fact that WR stars are clearly detected in this galaxy suggests that the excess of nitrogen has been released by the ejecta of these massive stars (Kobulnicky et al. 1997; Pustilnik et al. 2004; Brinchmann et al. 2008; López-Sánchez & Esteban 2010b). However, only few observations confirming the localized N enrichment are nowadays available (Kobulnicky et al. 1997; López-Sánchez et al. 2007; James et al. 2009; Monreal-Ibero et al. 2010; López-Sánchez et al. 2011), and in some cases the chemical pollution produced by the WR stars detected are not able to explain the observed N excess (Pérez-Montero et al. 2011; Amorín et al. 2012).

TABLE 4.4: Parameters used to derive the oxygen abundance following the strong emission-line methods.

Galaxy Name	$N_2$	$N_2O_2$	$O_3N_2$	$R_{23}$	$P$	$y$
NGC 1140	-0.971	-0.897	1.409	6.23	0.613	0.200
UM 311	-1.002	-0.962	1.433	6.34	0.593	0.164
NGC 3738	-0.810	-1.19	1.220	10.33	0.342	-0.285
IRAS 07164+5301	-0.580	-0.499	0.659	4.08	0.418	-0.144
NGC 6764	-0.446	-0.141	0.0332	1.985	0.286	-0.397
NGC 4861	-1.602	-1.10	2.37	8.82	0.900	0.953
NGC 3003	-0.444	-0.308	0.209	2.89	0.277	-0.417

The definition of the parameters are:

$$N_2 = \log([\text{N II}] \lambda 6583 / \text{H}\alpha),$$

$$O_3N_2 = \log \left( \frac{[\text{O III}] \lambda 5007 / \text{H}\beta}{[\text{N II}] \lambda 6583 / \text{H}\alpha} \right),$$

$$N_2O_2 = \log([\text{N II}] \lambda 6583 / [\text{O II}] \lambda 3727),$$

$$R_{23} = \log \left[ \left( [\text{O II}] \lambda 3727 + [\text{O III}] \lambda 4959 + [\text{O III}] \lambda 5007 \right) / \text{H}\beta \right],$$

$$P = ([\text{O III}] \lambda 4959 + [\text{O III}] \lambda 5007) / R_{23},$$

$$y = \log \left[ \left( [\text{O III}] \lambda 4959 + [\text{O III}] \lambda 5007 \right) / [\text{O II}] \lambda 3727 \right].$$

For all galaxies (even those two for which we have a direct estimation of  $T_e$ ) we estimate their oxygen abundances using the most-common empirical calibrations. Table 4.4 compiles all parameters (and their definitions) used for computing the oxygen abundances following these strong-line methods, while Table 4.5 lists the results. For more information about this methods and their equations, see Appendix A in López-Sánchez & Esteban (2010b). The KD02 method using the  $N_2O_2$  parameter can only be used for objects with  $12 + \log(\text{O}/\text{H}) \gtrsim 8.60$ , and hence Table 4.5 only gives its value for such objects.

TABLE 4.5: Oxygen abundances derived for our WR galaxy sample using the most commonly used strong emission-line methods. Last two columns compile the adopted oxygen abundance and the branch (lower, medium or upper) used. The third column also lists previous estimations of the O/H ratio in the literature. The strong emission-line calibrations are: M91: [McGaugh \(1991\)](#); KD02: [Kewley & Dopita \(2002\)](#); PT05: [Pilyugin & Thuan \(2005\)](#); P01: [Pilyugin \(2001a,b\)](#); PP04a: [Pettini & Pagel \(2004\)](#), using a linear fit to the  $N_2$  parameter; PP04c: [Pettini & Pagel \(2004\)](#), using the  $O_3N_2$  parameter.

Galaxy Name	$T_e$	Lit.	M91		KD02		PT05		P01		PP04a		PP04c		Adopted <sup>a</sup>	Branch
			$R_{23, y}$	$y$	$R_{23, y}$	$N_2O_2$	$R_{23, P}$	$P$	$R_{23, P}$	$P$	$N_2$	$N_2O_3$	$N_2$	$N_2O_3$		
NGC 1140	$8.38 \pm 0.10$	$8.29 \pm 0.09^b$	8.61	8.40	8.66	8.66	8.36	8.42	8.42	8.35	8.30	8.30	8.30	<b>8.41</b>	Upper	
IRAS 07164+5301		$8.96^c$	8.77	8.99	8.91	8.91	8.42	8.50	8.50	8.57	8.52	8.52	8.52	<b>8.50<sup>d</sup></b>	Upper	
NGC 3738		$8.23^f$	8.53	8.57	8.37	8.37	8.65	8.63	8.63	8.44	8.35	8.35	8.35	<b>8.51</b>	Upper	
UM 311		$8.31 \pm 0.04^e$	8.31	8.43			8.12	8.15	8.15	8.33	8.28	8.28	8.28	<b>8.27</b>	Med	
NGC 6764			8.97	9.12	9.07	9.07	8.53	8.68	8.68	8.65	8.72	8.72	8.72	<b>8.65<sup>d</sup></b>	Upper	
NGC 4861	$7.95 \pm 0.05$	$8.05 \pm 0.04^g$	8.03	8.22			7.77	7.83	7.83	7.99	7.97	7.97	7.97	<b>7.88<sup>d</sup></b>	Lower	
NGC 3003			8.87	9.06	9.00	9.00	8.41	8.56	8.56	8.65	8.66	8.66	8.66	<b>8.57<sup>d</sup></b>	Upper	

<sup>a</sup>: Average abundance value using all the empirical methods, the  $T_e$  method is not considered here. The KD02 method using the  $N_2O_2$  parameter is only considered for objects with  $12 + \log(O/H) \gtrsim 8.60$  dex (NGC 3738, NGC 6764 and NGC 3003).

<sup>b</sup>: [Moll et al. \(2007\)](#) through the  $T_e$  method.

<sup>c</sup>: Taken from the literature ([Huang et al. 1996](#)) through  $T_e$  method, although we consider this value is too high, see text.

<sup>d</sup>: Average abundance value using only P01, PT05 and PP04a,c empirical calibrations, as M91 and KD02 give values which we consider are too high.

<sup>e</sup>: [Izotov & Thuan \(1998\)](#).

<sup>f</sup>: [Martin \(1997\)](#).

<sup>g</sup>: [Esteban et al. \(2009\)](#).

The final adopted value for the oxygen abundance in each galaxy has been computed by averaging all the results provided by these calibrations, and it is compiled in Table 4.5. As it has been already noticed by several authors (Peimbert et al. 2007; Bresolin et al. 2009; López-Sánchez & Esteban 2010b; Moustakas et al. 2010; Rosales-Ortega et al. 2011; López-Sánchez et al. 2012), those empirical calibrations that are based on strong emission-lines techniques that are based on photoionization models (McGaugh 1991; Kewley & Dopita 2002) tend to overpredict the observed oxygen abundances derived using the  $T_e$  method and the empirical calibrations based on it (Pilyugin 2001a,b; Pilyugin & Thuan 2005; Pettini & Pagel 2004; Pilyugin et al. 2010) by 0.2–0.4 dex. Here we also observe that behavior in the majority of the analyzed regions. We therefore do not consider the values given by the McGaugh (1991) and Kewley & Dopita (2002) techniques when deriving the average oxygen abundance in these cases.

The adopted oxygen abundance following the empirical calibrations for the two galaxies for which we have a direct estimation of  $T_e$  agrees well within the errors, so we consider that the oxygen abundances derived for the rest of the objects are reliable besides the uncertainties. Assuming that the solar abundance is  $12+\log(\text{O}/\text{H})_{\odot}=8.66$  (Asplund et al. 2005), we finally derived the metallicity,  $Z$ , for each galaxy. These values have been compiled in Table 2.2.

### 4.6.3 Analysis of the WR features

A magnified view of the spectrum of NGC 1140 around 4650 Å is presented in Fig. 4.10. The blue WR bump at around 4686 Å, which was previously reported by Guseva, Izotov & Thuan (2000), is clearly identified in this spectrum. We also identify the red WR bump around C IV  $\lambda$ 5808, as it is seen in Fig. 4.11. We also identify both WR features in the spectrum of the low-metallicity galaxy NGC 4861. In this case, both the broad and the narrow He II  $\lambda$ 4686 emission lines are observed (see Figs 4.12 to 4.13).

We followed the procedure described in [López-Sánchez & Esteban \(2010a\)](#) to derive the number of WR stars and the WR/(WR+O) ratio in NGC 1140. Using the values for the flux of the broad He II  $\lambda 4686$  and C IV  $\lambda 5808$  emission lines tabulated in Table 4.2 and considering the metallicity-dependence of the WR luminosities –Eqs. 7 and 8 in [López-Sánchez & Esteban \(2010a\)](#)–, we derive  $WNL = 92$  and  $WCE = 59$ . From the total luminosity of the  $H\beta$  line and considering their Eq. 10, we find that the total number of O stars in the burst is 1553. For this, we also assumed  $\eta_0(t) \sim 0.25$  following the WR models provided by [Schaerer & Vacca \(1998\)](#). We then derive a WR/(WR+O) ratio of 0.089 and a WCE/WNL ratio of 0.64. Both values agree well with the ratios expected for an object with the oxygen abundance of NGC 1140.

We repeat this procedure for NGC 4861, a low-metallicity galaxy also showing both the broad He II  $\lambda 4686$  and C IV  $\lambda 5808$  emission lines. Note that for this object we subtracted the flux of the nebular, narrow He II  $\lambda 4686$  emission line to get a proper estimation of the flux of the broad He II  $\lambda 4686$  emission line. In this case, we derive  $WNL = 225$ ,  $WCE = 67$  and  $O = 4336$ , assuming  $\eta_0(t) \sim 0.25$  and the appropriate oxygen abundance for the WR luminosities. Hence, we estimate that the WR/(WR+O) and the WCE/WNL ratios for NGC 4861 are 0.062 and 0.30, respectively. Both the values are also in agreement with the WR ratios expected for this galaxy.



# Chapter 5

## Stellar Populations

### 5.1 Introduction

The light of galaxies (from the ultraviolet to the near infrared region of the spectrum) comes largely from the photospheres of the stars constituting them. Stars are the building blocks of galaxies. Research on stellar populations is the study of the different generations of stars which make up a galaxy. This is the principal way in which we determine the life history of galaxies. Astronomers use the term “stellar population” to refer to a single generation of stars characterized by a common age and chemical composition. A galaxy can be composed of a large number of individual populations. We can analyze stellar populations in two main ways: Either studying the individual stars in a galaxy but this is limited only to nearby galaxies where we can resolve the stars or by studying the integrated spectrum (combined light output) of the stars in a galaxy. Here, we have used the broad-band photometry of the star forming regions to analyze the dominating young stellar populations and underlying older stellar populations through the U, B, V, R and I filters. As we have previously discussed in chap.2, these star forming regions were already identified through our narrow band photometry.

## 5.2 Observations

TABLE 5.1: Details of optical broad-band observations

Galaxy Name	Date [dd/mm/yyyy]	U [s]	B [s]	V [s]	R [s]	I [s]	Teles.
NGC 1140	14/12/2007	3900	3600	2700	3000	3300	ARIES
IRAS 07164+5301	16/02/2010	7x900	5x600	5x300	5x240	5x240	HCT
NGC 3738	17/02/2010	6x720	7x480	7x300	6x240	5x240	HCT
UM 311	31/10/2008	3000	1200	900	360	260	HCT
NGC 6764	31/10/2008	3200	650	360	200	200	HCT
NGC 4861	03/05/2011	2x600	2x450	2x300	3x150	3x150	HCT
NGC 3003	26/03/2009	2700	1450	1300	960	940	HCT

Broad-band photometric observations of NGC 1140 were obtained in *UBVRI* bands using ARIES 1m telescope with  $2k \times 2k$  CCD. The plate scale is  $0.37''/\text{pixel}$ , covering an area of  $12'.6 \times 12'.6$ . Observations were done under photometric sky condition. To improve the signal to noise ratio (S/N) on chip  $2 \times 2$  binning mode was used. Apart from the galaxy frames, calibration frames e.g. bias, flats were also taken, for pre-processing of the object(science) frames. Photometric standard stars from the list of Landolt (1992) were observed for photometric calibration. Apart from NGC 1140, other galaxies observations of the star-forming regions within our WR galaxy sample were obtained using HFOSC (*Hanle Faint Object Spectrograph Camera*) mounted on the 2m Himalayan Chandra Telescope (HCT), of the Indian Astronomical Observatory (IAO). HFOSC is equipped with a  $2k \times 4k$  SITe CCD chip. The central  $2k \times 2k$  region with plate scale of  $0.296''/\text{pixel}$ , provides  $10 \times 10$  arcmin field of view.

## 5.3 Model Starburst99

This model was developed at Space Telescope Science Institute(STsci) by Claus Leitherer, Daniel Schaerer, Jeff Goldader, Rosa Gonzalez-Delgado, Carmelle Robert, Denis Foo Kune, Duilia de Mello, Daniel Devost, Timothy M. Heckman, Alessandra Aloisi, Lucimara Martins, and Gerardo Vazquez. A description of the input physics is in Leitherer et al(1999), Vazquez & Leitherer (2005) and

Leitherer et al(2010). It is a web based software and data package designed to model spectrophotometric and related properties of star-forming galaxies. Models have been developed and widely used over the past few decades to rationalize the observed characteristics of star-forming regions of particular interest to these type research are the Starburst99 (SB99) models which is developed by Leitherer et al. (1999). The SB99 models combine spectra of individual stars to predict the spectral appearance of a large number of stars as a function of time. Specifically, they predict the luminosity of a star-forming region as a function of wavelength and age, based on the number and variety of stars present in active star-forming regions.

Observations of starbursts galaxies can give complete insights of the processes and spectral characteristics of massive star formation regions. In such regions the physical conditions are similar to those that existed at the time of collapse and formation of galaxies in the early universe, and they can also provide an understanding of early galaxy evolution. The Infrared Astronomical Satellite (IRAS) made the key discovery of large numbers of infrared luminous galaxies, similar to those found by Rieke & Low (1972a). Many of these are dominated by intense star formation (Lutz et al., 1996, 1998; Genzel et al., 1998; Veilleux et al., 1995; Veilleux, Sanders, & Kim, 1999) in which the luminosity of the young hot stars heats the surrounding dust, producing large amounts of infrared radiation. The theoretical tools required to interpret the spectra of such galaxies are now available. For example, detailed stellar population synthesis models have been developed for both instantaneous and continuous starbursts and using these models, one is able to derive parameters such as the starburst age and metallicity from the continuous spectrum. Like this, there are several different models available for various environmental conditions. In such models, the stellar initial mass function (IMF), star formation rate (SFR) and stellar atmosphere formulations are all adjustable initial parameters. Each model depends on three main parameters: 1) Initial Mass Function, 2) Metallicity, and 3) Star Formation

Process. Each parameter is described below.

**Initial Mass Function:** The IMF approximates the stars' mass distribution during a burst of star formation. In a given region, stars are present with a range of masses between 0.1 and approximately  $100 M_{\odot}$ . Essentially, the IMF is a probability function that represents the likelihood that a star will form with a mass between  $M$  and  $M+dM$ . Generally it has been proven that the Salpeter IMF is appropriate for modeling star-forming regions. Therefore in this context we have used the Salpeter IMF as a parameter for our analysis:  $F(M) = M^{-2.35}$ .

**Metallicity:** All the heavy elements observed in the universe have been synthesized by nuclear reactions in the interiors of stars and by reactions that immediately follow supernovae explosions. Supernovae distribute heavy elements to the interstellar medium, thereby enriching the raw material that will form the next generation of stars. As a result, successive generations of newborn stars contain a greater mixture of heavy elements, and the overall metal abundance of a galaxy increases with time.

**Star Formation Process:** SB99 models are available for two different star formation processes, instantaneous and continuous. The instantaneous process describes a single burst of star formation, and while the stars evolve, no further starbursts occur. The continuous process allows for successive generations of starbirth within a given region. By consequence, there are always young stars present, even if the region is very old. For our analysis, we adapt the instantaneous star formation process because our observed star-forming regions are relatively small in terms of volume. In this case, we can reasonably expect that star-formation occurs in a single burst.

TABLE 5.2: Results of the analysis of the broad-band photometry in the detected star-forming regions within our WR galaxy sample.

Object	Knot ID	$m_V$ [mag]	$U - B$	$B - V$	$V - R$	$V - I$	$R - I$
NGC 1140	# 1	12.10±0.03	-0.64±0.03	0.01±0.02	0.15±0.03	0.28±0.03	0.12±0.03
	# 2	16.99±0.14	-0.55±0.09	0.16±0.10	0.27±0.11	0.57±0.15	0.30±0.15
	# 3	18.67±0.06	-1.07±0.06	-0.15±0.05	0.22±0.05	0.04±0.04	-0.18±0.04
	# 4	16.54±0.06	-1.12±0.06	-0.16±0.04	0.15±0.05	0.11±0.06	-0.04±0.07
IRAS 07164+5301	# 1	14.06±0.03	-0.47±0.05	0.06±0.02	0.16±0.02	0.30±0.02	0.15±0.03
NGC3738	# 1	13.01±0.07	-0.54±0.04	0.20±0.05	0.19±0.06	0.56±0.06	0.37±0.06
UM 311	# 3	16.93±0.03	-1.12±0.02	0.07±0.02	1.67±0.03	0.16±0.03	-1.51±0.03
NGC 6764	# 1	12.66±0.04	-1.17±0.06	-0.15±0.03	-0.10±0.03	0.60±0.03	0.71±0.03
	# 2	10.68±0.03	-1.06±0.05	-0.19±0.03	0.01±0.03	0.30±0.02	0.29±0.03
	# 3	13.74±0.05	-1.20±0.07	-0.18±0.04	-0.06±0.04	0.63±0.03	0.70±0.04
NGC 4861	# 1	13.83±0.05	-0.96±0.06	0.33±0.02	-0.06±0.04	-0.31±0.04	-0.26±0.05
	# 2	19.92±0.09	-1.11±0.09	0.64±0.07	-0.27±0.08	-1.01±0.35	-0.75±0.35
	# 3	21.67±0.29	-0.87±0.12	-0.52±0.20	0.73±0.22	0.31±0.35	-0.42±0.32
	# 4	19.27±0.08	-1.07±0.06	-0.17±0.06	-0.01±0.07	-1.01±0.27	-1.01±0.27
	# 5	20.49±0.14	-1.03±0.10	-0.08±0.12	1.21±0.10	0.08±0.27	-1.13±0.25
	# 6	19.92±0.07	-0.78±0.05	-0.32±0.05	0.28±0.06	-0.64±0.21	-0.93±0.21
	# 7	19.74±0.11	-1.25±0.08	-0.03±0.08	0.16±0.09	-3.83±4.18	-4.01±4.19
	# 8	19.28±0.07	-1.14±0.05	-0.11±0.05	-0.35±0.06	-0.13±0.11	0.22±0.11
	# 9	20.48±0.14	-0.53±0.11	-0.03±0.09	0.29±0.12	-0.41±0.23	-0.70±0.23
	#10	21.20±0.13	-0.99±0.22	1.02±0.11	0.15±0.11	-1.57±0.70	-1.74±0.70
	#11	21.12±0.20	-0.86±0.13	-0.12±0.14	0.43±0.16	-0.64±0.36	-1.08±0.36
	#12	20.18±0.07	-1.21±0.05	0.20±0.05	0.07±0.06	0.11±0.15	0.03±0.15
NGC 3003	# 1	20.82±0.08	-1.36±0.06	0.23±0.06	0.59±0.07	-0.42±0.22	-1.02±0.22
	# 2	20.44±0.13	-1.13±0.09	0.07±0.10	0.33±0.10	0.14±0.18	-0.19±0.18
	# 3	16.94±0.02	-0.91±0.02	0.30±0.02	3.32±0.02	0.34±0.03	-2.98±0.03
	# 4	20.52±0.23	-1.05±0.12	-0.11±0.13	0.29±0.20	0.90±0.14	0.61±0.20
	# 5	20.88±0.27	-1.66±0.16	0.10±0.21	1.20±0.21	1.45±0.21	0.26±0.17
	# 6	19.18±0.11	-0.77±0.06	-0.06±0.06	0.16±0.09	0.25±0.09	0.09±0.11
	# 7	20.46±0.22	-0.39±0.18	0.23±0.15	-0.11±0.19	0.63±0.15	0.74±0.20
	# 8	20.85±0.24	-1.37±0.09	-0.16±0.14	0.18±0.21	0.52±0.24	0.34±0.27
	# 9	19.89±0.24	-0.54±0.17	0.58±0.18	-0.04±0.21	0.88±0.17	0.92±0.21
	#10	22.27±0.71	-1.40±0.23	-0.58±0.50	1.44±0.54	1.20±0.63	-0.23±0.51
	#11	22.20±0.49	-1.18±0.27	-0.98±0.96	2.09±0.95	1.66±1.04	-0.42±0.52
	#12	18.39±0.22	-1.08±0.08	0.21±0.12	-0.12±0.20	0.55±0.18	0.67±0.23
	#13	14.45±0.02	-0.21±0.02	0.65±0.02	0.59±0.01	1.11±0.01	0.53±0.01
	#14	19.14±0.13	-0.76±0.06	-0.33±0.09	0.56±0.10	0.29±0.14	-0.28±0.14
	#15	17.34±0.11	-0.73±0.07	0.29±0.08	0.48±0.09	0.94±0.09	0.47±0.09
	#16	19.82±0.06	-1.16±0.04	0.18±0.03	0.24±0.05	0.35±0.05	0.11±0.06
	#17	20.53±0.11	-0.55±0.08	0.08±0.07	-0.04±0.10	0.45±0.09	0.49±0.12
	#18	16.71±0.04	-0.61±0.04	0.20±0.03	0.41±0.04	0.75±0.04	0.34±0.04
	#19	19.56±0.19	-0.87±0.08	-0.45±0.14	0.85±0.14	0.68±0.18	-0.17±0.15
	#20	19.38±0.05	-0.95±0.03	0.12±0.03	0.25±0.05	0.61±0.04	0.36±0.04
	#21	18.57±0.13	-0.46±0.10	0.20±0.10	0.25±0.10	0.91±0.09	0.66±0.09
	#22	18.10±0.05	-0.83±0.03	0.28±0.03	0.14±0.04	0.38±0.05	0.25±0.06
	#23	20.49±0.12	-1.31±0.05	-0.00±0.07	0.41±0.10	-0.24±0.19	-0.65±0.20
	#24	20.00±0.06	-1.28±0.04	0.11±0.04	0.44±0.05	0.21±0.07	-0.24±0.07
	#25	21.05±0.15	-1.43±0.13	0.48±0.13	0.28±0.13	0.21±0.15	-0.07±0.16

## 5.4 Broad-band Photometry results

The broad band photometry of all seven galaxies  $U - B$  vs.  $B - V$  diagrams are plotted by comparing the predictions given by evolutionary synthesis models provided by the Starburst 99 code (Leitherer et al. 1999) with the colors obtained from the star-forming regions within the WR galaxies of our sample. The metallicity of each model is also shown, and it is  $Z = 0.008$  for the galaxies NGC 1140, IRAS 07164+5301, NGC 3738 and UM 311;  $Z = 0.02$  for NGC 6764;  $Z = 0.004$  for NGC 4861; and  $Z = 0.02$  for NGC 3003. In these figures (Ex: Fig. 5.1) the solid line represents the model track and Myr values are all over plotted as 1, 3, 4, 5...15, 50 Myr up to 1Gyr and 5 Gyr to identify the data points in a model track. Aperture photometry of the star-forming regions was carried out within the apertures drawn in Figures 3.1 to 3.14. We then computed the apparent  $V$ -magnitude,  $m_V$ , and the colors  $U - B$ ,  $B - V$ ,  $V - R$ , and  $V - I$ , of all SF regions. Broad-band colours were corrected for foreground extinction (i.e., Galactic extinction) using the  $E(B - V)$  data provided by Schlegel, Finkbeiner & Davis (1998), all values are compiled in Table 2.2. The internal extinction has been corrected using the comparison of broad-band color-color diagrams with the predictions given by Starburst99 (Leitherer et al. 1999) evolutionary synthesis models (see Fig. 5.5 to Fig. 5.11 and Sect. 5.5 for details). No correction for emission lines from the ionized gas has been considered, although it may be somewhat important in some bright, star-forming knots (see Appendix A in López-Sánchez & Esteban 2008). Table 5.2 compiles the results of this analysis. Uncertainties quoted in Table 5.2 consider only the photometric error.

## 5.5 Ages of the dominant stellar populations

We have also used the same Starburst99 models to estimate the age of the dominant stellar population underlying each H II region. We compared Starburst99

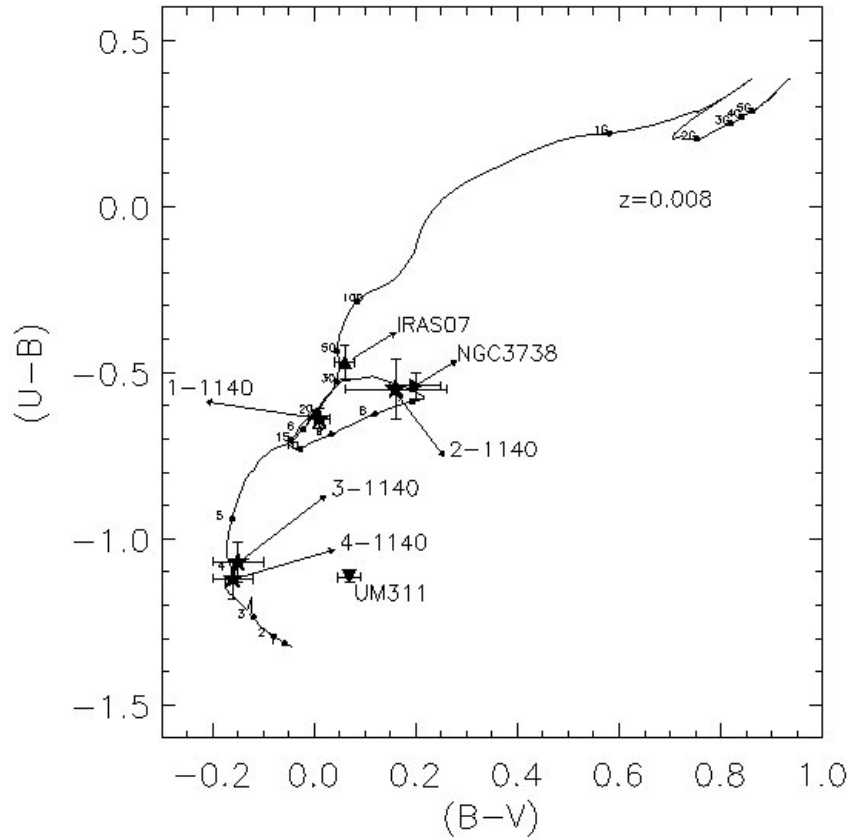


FIGURE 5.1: SB99 model plot of NGC 1140 (Knot IDs 1, 2, 3 and 4), IRAS 07164+5301, UM 311 and NGC 3738 for the metallicity  $z=0.008$

model tracks for various colours and metallicities with the colors we derived in each star-forming region and determine the age which best fits the observing data with the predictions given by the models. Although the ages derived using this method have larger uncertainties (typically, between 2 and 5 Myr for young stellar populations) than the ages determined from the  $H\alpha$  equivalent widths, this exercise is useful for discriminating between young ( $\lesssim 25$  Myr), intermediate (100–300 Myr), and old ( $> 500$  Myr) stellar populations (see [López-Sánchez, Esteban & García-Rojas 2006](#), for details of the method).

We should expect some disagreement between the models and the observational data as the star-forming regions would actually host a mixed stellar populations, with stars that have been created in the last starburst event on top

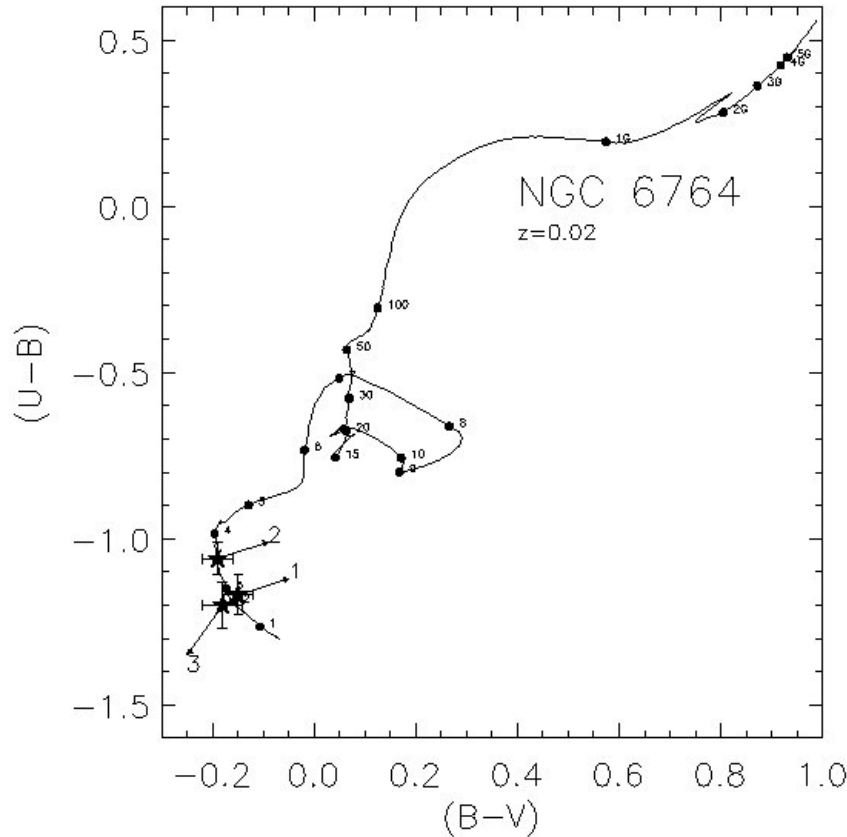


FIGURE 5.2: SB99 model plot of NGC 6764 for the metallicity  $z=0.008$

of an older stellar population. Indeed, in the case of having a bright or very recent star-formation event in a region which has an important old underlying population we will get high  $W(\text{H}\alpha)$  values, low  $U - B$  colours but higher  $B - V$  or  $V - R$  colours than those expected using the models. That is because the old, reddish stellar population is not affecting much the emission in the  $U$  filter and in  $\text{H}\alpha$ , but it considerably affects  $B$ ,  $V$ ,  $R$  and  $I$  data, being specially important in the infrared filters. Indeed,  $NIR$  data are usually needed to disentangle the effect of the mixed (young/old) stellar populations in strong star-forming galaxies (e.g. [Noeske et al. 2003](#); [López-Sánchez & Esteban 2008](#)).

Figures 5.1 to 5.4 plots the Starburst99 model tracks for the  $U - B$  vs.  $B - V$  color-color diagram; the estimated colours of the star-forming knots are overlaid onto these model tracks. However, we have the effect of reddening, which is also

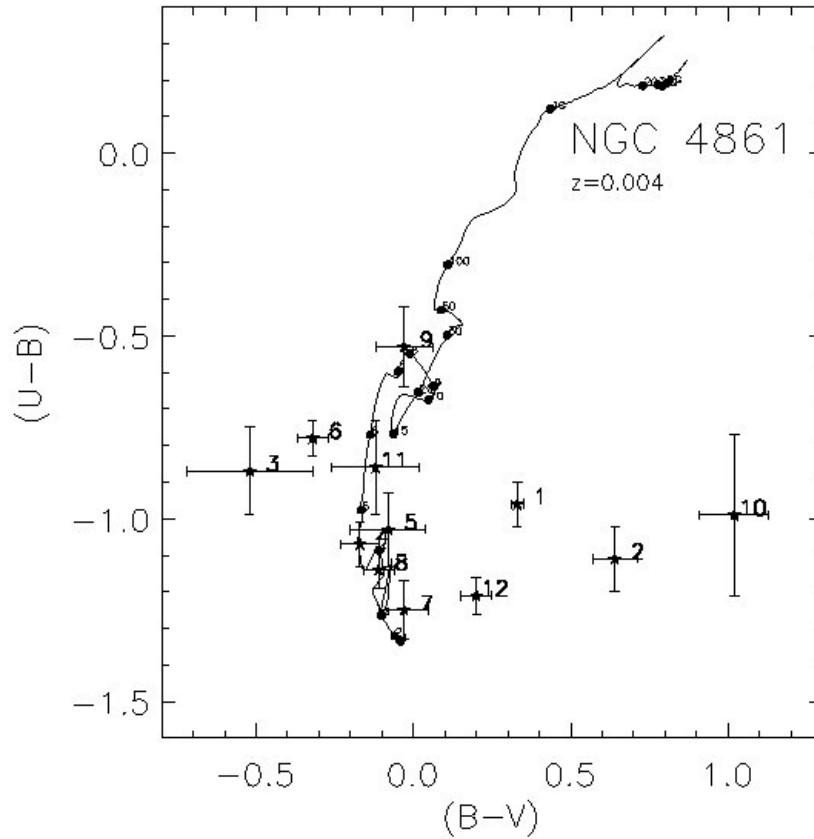


FIGURE 5.3: SB99 model plot of NGC 3738 and UM 311 for the metallicity  $z=0.008$

modifying the position of our observational data on the color-color diagrams. As explained in Sect. 5.4, we considered the Galactic values for reddening using the Schlegel et al. (1998) data. The intrinsic extinction can be determined from the  $c(H\beta)$  derived from spectroscopy (López-Sánchez & Esteban 2009), however here we have used a different method to estimate the intrinsic extinction for the analyzed star-forming regions.

In our case, we derived the internal extinction in regions for which we found a good match between the  $B - V$  vs.  $V - R$  color-color diagram and the observational values (see Figures 5.5 to 5.11). In these case, we considered the  $E(B - V)_{intrinsic}$  value that makes matching the  $U - B$  vs.  $B - V$  color-color model track with that observed in that region. The calculated intrinsic

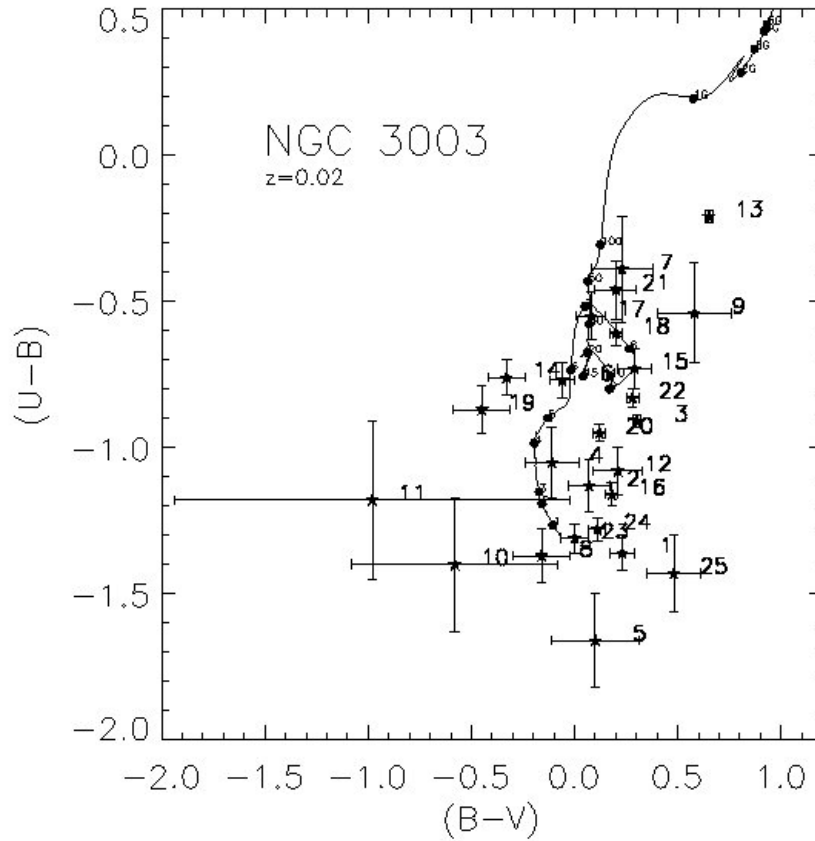


FIGURE 5.4: SB99 model plot of NGC 3003 for the metallicity  $z=0.02$

extinction values for those points in NGC 1140, NGC 3738 and NGC 6764 (which is rather reddened) are all matching with the existing literature extinction values, and hence we consider this method is also giving good values for the internal extinction in IRAS 07164+5301 and some regions in NGC 4861. However, in the case of UM 311, which we see through a foreground galaxy, this method seems not to be valid. The derived  $E(B - V)_{intrinsic}$  values are listed in Table 5.3. Once the intrinsic reddening is determined, we estimate the age of the young stellar population from the  $U - B$  vs.  $B - V$  diagram and compared with that derived from the  $W(H\alpha)$ . Later, we use the rest of color-color diagrams to get an estimate of the age of the old stellar population. All these age estimates are compiled in Table 5.3.

TABLE 5.3: Estimation of the age of the young and old stellar populations using the broad-band colors.

Galaxy	$Z$ [ $Z_{\odot}$ ]	Knot	$E(B - V)_{intrinsic}$ [mag]	Ages estimated from broad-band colors				Age Adopted	
				$U - B$ [Myr]	$B - V$ [Myr]	$V - R$ [Myr]	$V - I$ [Myr]	YOUNG [Myr]	OLD [Myr]
NGC 1140	0.008	1	0.26	6.2 - 21	9.4 - 25	200 - 300	400 - 500	6.2	500
		2	0.16	6.4 - 8.0	80 - 100	200 - 300	400 - 500	6.5	500
		3	0.10	3.6 - 4.7	3.6 - 4.7	100 - 200	5 - 100	3.6	200
		4	0.22	3.7	3.7	50 - 100	10 - 100	3.7	100
IRAS 07164+5301	0.008	1	0.40	7	40 - 55	500 - 800	500 - 800	7	800
NGC 3738	0.008	1	0.10	6.5	100	100 - 300	400 - 500	6.5	500
UM 311	0.008	3	0.2	3 - 4	300	400 - 500	400 - 500	3	500
NGC 6764	0.02	1	0.95	30	600 - 800	>1000	>1000	30	>1000
		2	0.95	50	600 - 800	>1000	>1000	50	>1000
		3	0.87	20	600 - 800	>1000	>1000	20	>1000
NGC 4861	0.004	1	0.2	8 - 9	700	500		8	700
		2	0.2	5 - 6	600	800 - 1000		5	1000
		3	0.2	4 - 15	300	500	500	4	500
		4	0.2	4.0 - 4.8	4 - 20	100	100 - 200	4	200
		5	0.2	3.1 - 5.3	5 - 30	>1000	500	3.1	>1000
		6	0.2	5.5 - 6.5		100	500	5.5	500
		7	0.2	1.7 - 3.5	30 - 100	200 - 300	500	1.7	500
		8	0.2	3.1 - 4.2	100		100	3.1	100
		9	0.2	6.5 - 9	10 - 50	200	300 - 500	6.5	500
		10	0.2	3 - 6	>1000	500	500 - 1000	3	>1000
		11	0.2	4.9 - 6.2	10 - 200	>1000		5	>1000
		12	0.2	2 - 3	40 - 100	50 - 200	5 - 100	2	200
NGC 3003	0.02	1		1 - 2	20 - 100	>1000		1	>1000
		2		1 - 1.3	9 - 11	500	500 - 800	1	800
		3		3 - 10	800 - 1000	>1000		3	1000
		4		2.3 - 4.7	100	100 - 200	500 - 1000	2.3	1000
		5		1	10 - 100	100 - 200	100 - 200	1	200
		6		5.8 - 6.2	10 - 50	100 - 200	100 - 200	5.8	200
		7		40 - 100	60 - 120	200	200 - 400	40	400
		8		1	10 - 20	10 - 50	50 - 200	1	200
		9		7.8 - 50	400 - 800	20 - 100	1000	7.8	1000
		10		1 - 2.2		>1000	>1000	1	>1000
		11		1 - 5	5 - 10	>1000	>1000	1	>1000
		12		3 - 5	20 - 100	100	100 - 200	3	200
		13		20 - 40	>1000	>1000	>1000	20	>1000
		14		5.5 - 7		>1000	1000	5.5	>1000
		15		8.0 - 8.7	>1000	>1000	500 - 800	8	>1000
		16		3 - 6	20 - 80	>1000	100 - 200	3	>1000
		17		6.9 - 7.4	20 - 40		50 - 200	5.9	200
		18		7.5 - 7.8	30 - 60	>1000	100 - 200	7.5	>1000
		19		4.5 - 7		>1000	200 - 500	4.5	>1000
		20		3 - 5	20 - 80	>1000	200 - 500	3	>1000
		21		10 - 60	40 - 100	>1000	>1000	10	>1000
		22		5 - 6	200 - 300	>1000	>1000	5	>1000
		23		1 - 3	5 - 15	200 - 500		1	500
		24		1 - 3	10 - 30	>1000	100 - 200	1	>1000
		25		1 - 2	400 - 800	400 - 600	100 - 200	1	800

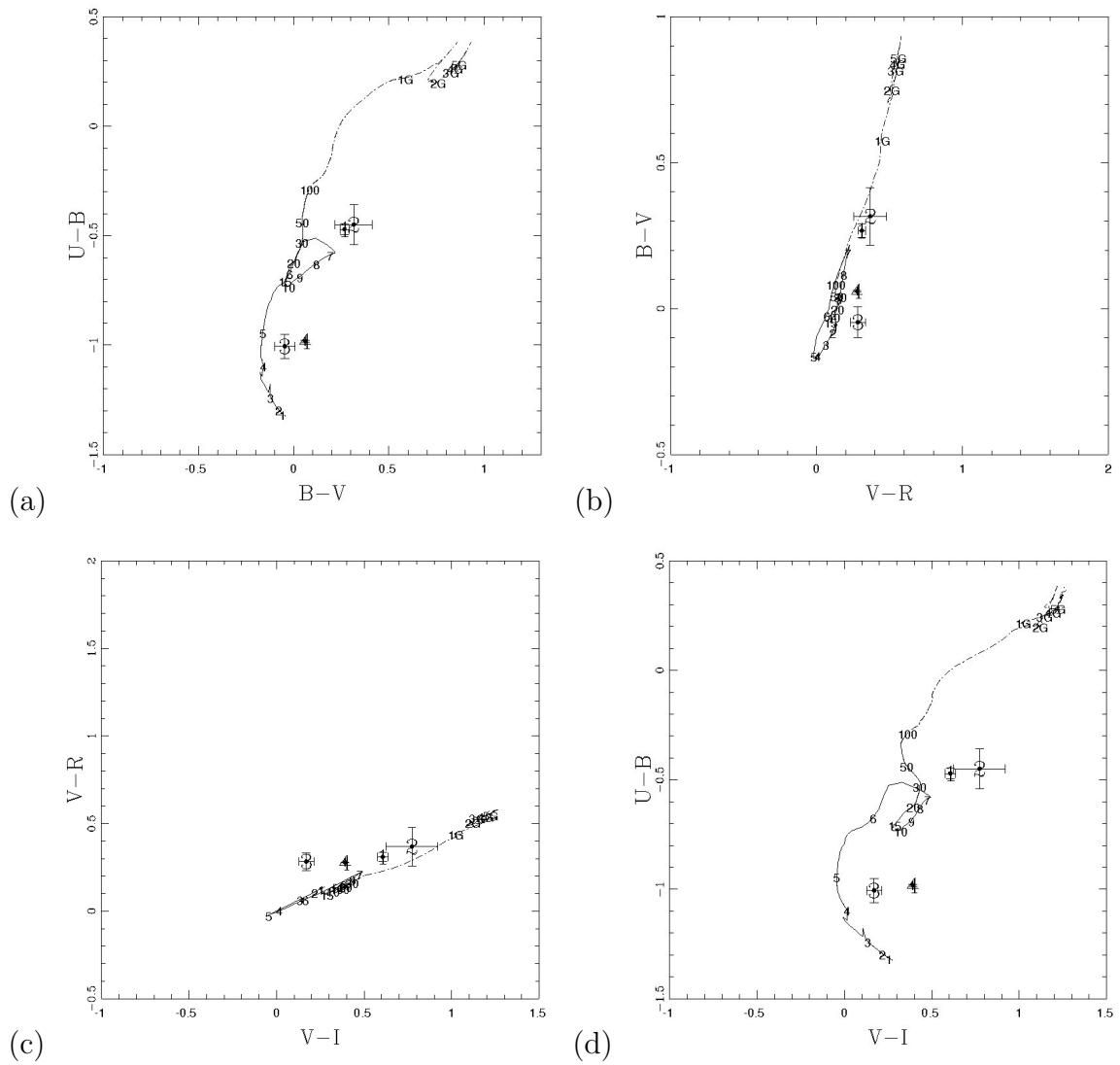


FIGURE 5.5: foreground corrected Colour-Colour plot of the galaxy NGC 1140, for the metallicity  $z=0.008$ ; (a)  $U-B$  Vs  $B-V$  (b)  $B-V$  Vs  $V-R$  (c)  $V-R$  Vs  $V-I$  (d)  $U-B$  Vs  $V-I$

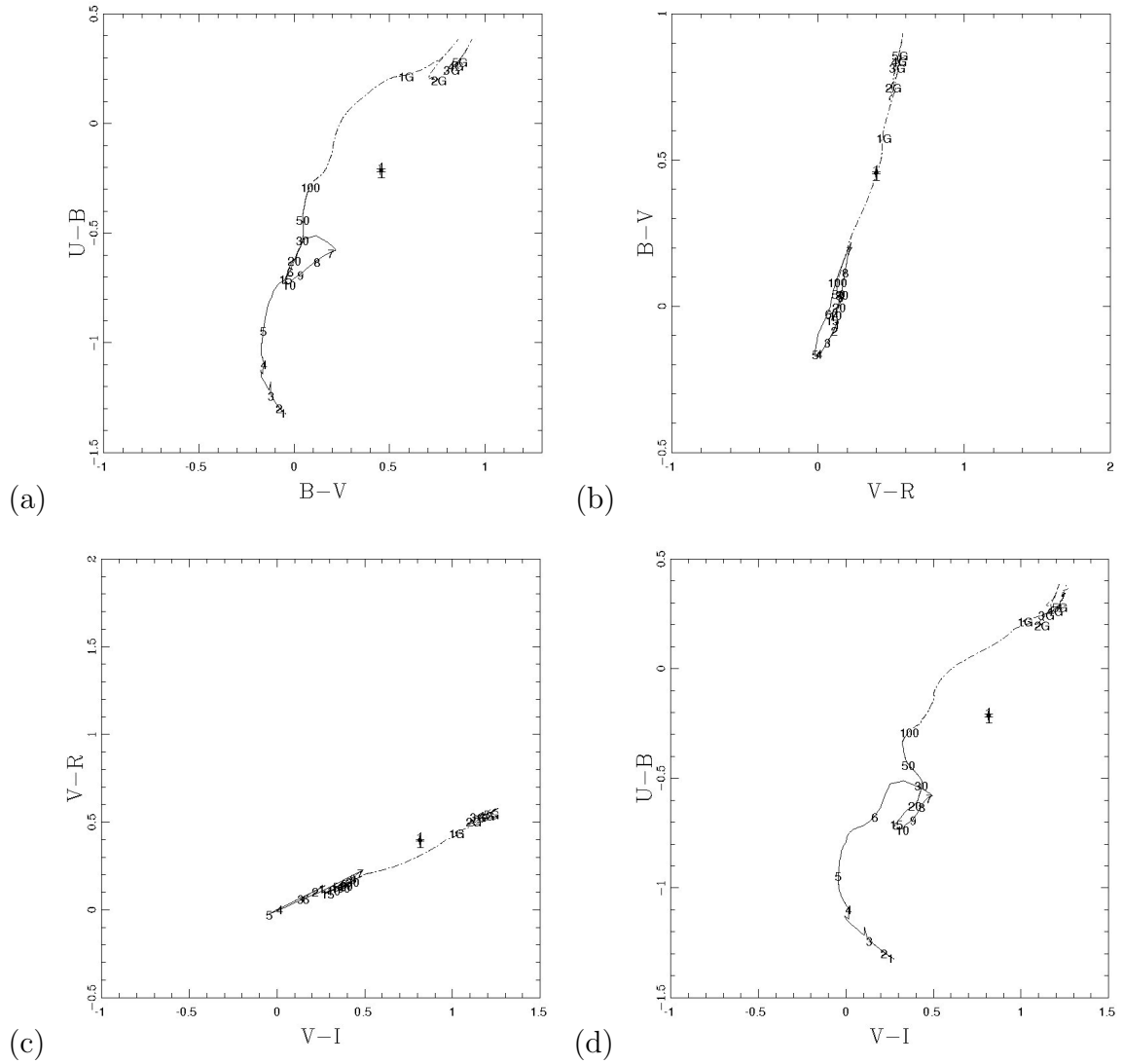


FIGURE 5.6: Colour-Colour plot of the galaxy IRAS 07164+5301, for the metallicity  $z=0.008$ ; (a)  $U-B$  Vs  $B-V$  (b)  $B-V$  Vs  $V-R$  (c)  $V-R$  Vs  $V-I$  (d)  $U-B$  Vs  $V-I$

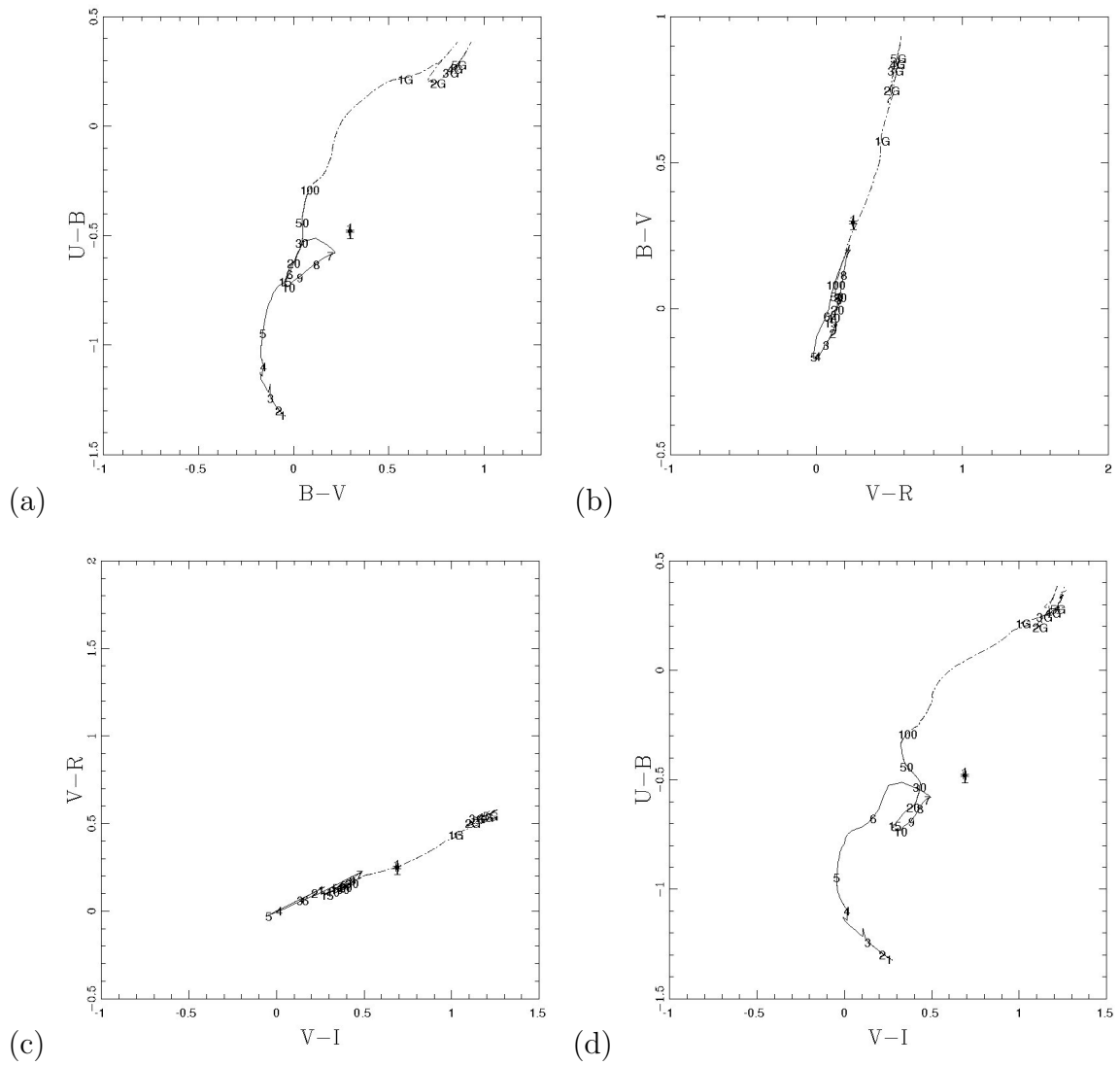


FIGURE 5.7: Foreground corrected colour-colour plot of the galaxy NGC 3738, for the metallicity  $z=0.008$ ; (a)  $U-B$  Vs  $B-V$  (b)  $B-V$  Vs  $V-R$  (c)  $V-R$  Vs  $V-I$  (d)  $U-B$  Vs  $V-I$

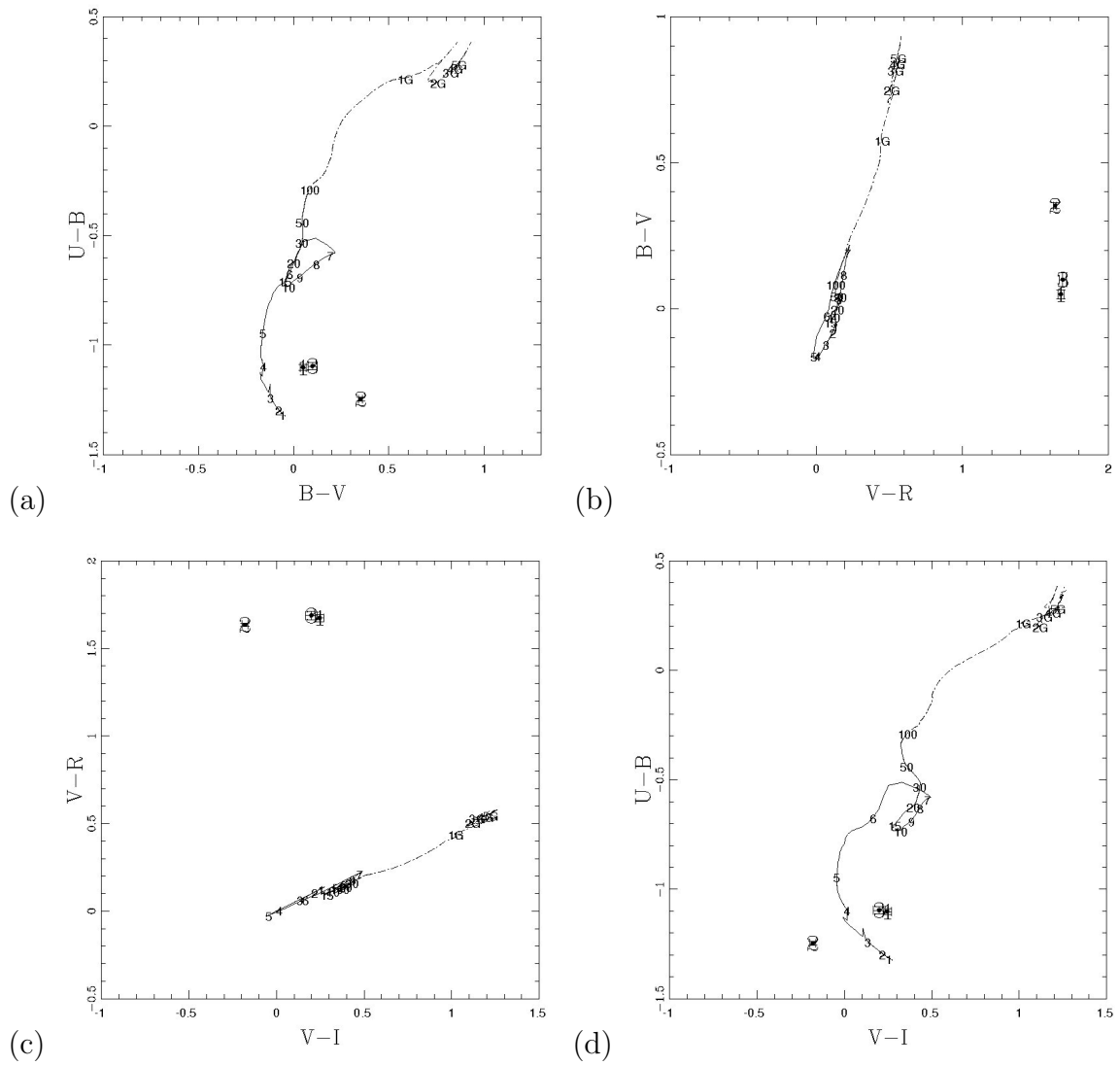


FIGURE 5.8: Foreground corrected colour-colour plot of the galaxy UM 311, for the metallicity  $z=0.008$ ; In this figure only ID number 3 is the galaxy other ID's 1 and 2 are near by galaxies. (a)  $U-B$  Vs  $B-V$  (b)  $B-V$  Vs  $V-R$  (c)  $V-R$  Vs  $V-I$  (d)  $U-B$  Vs  $V-I$

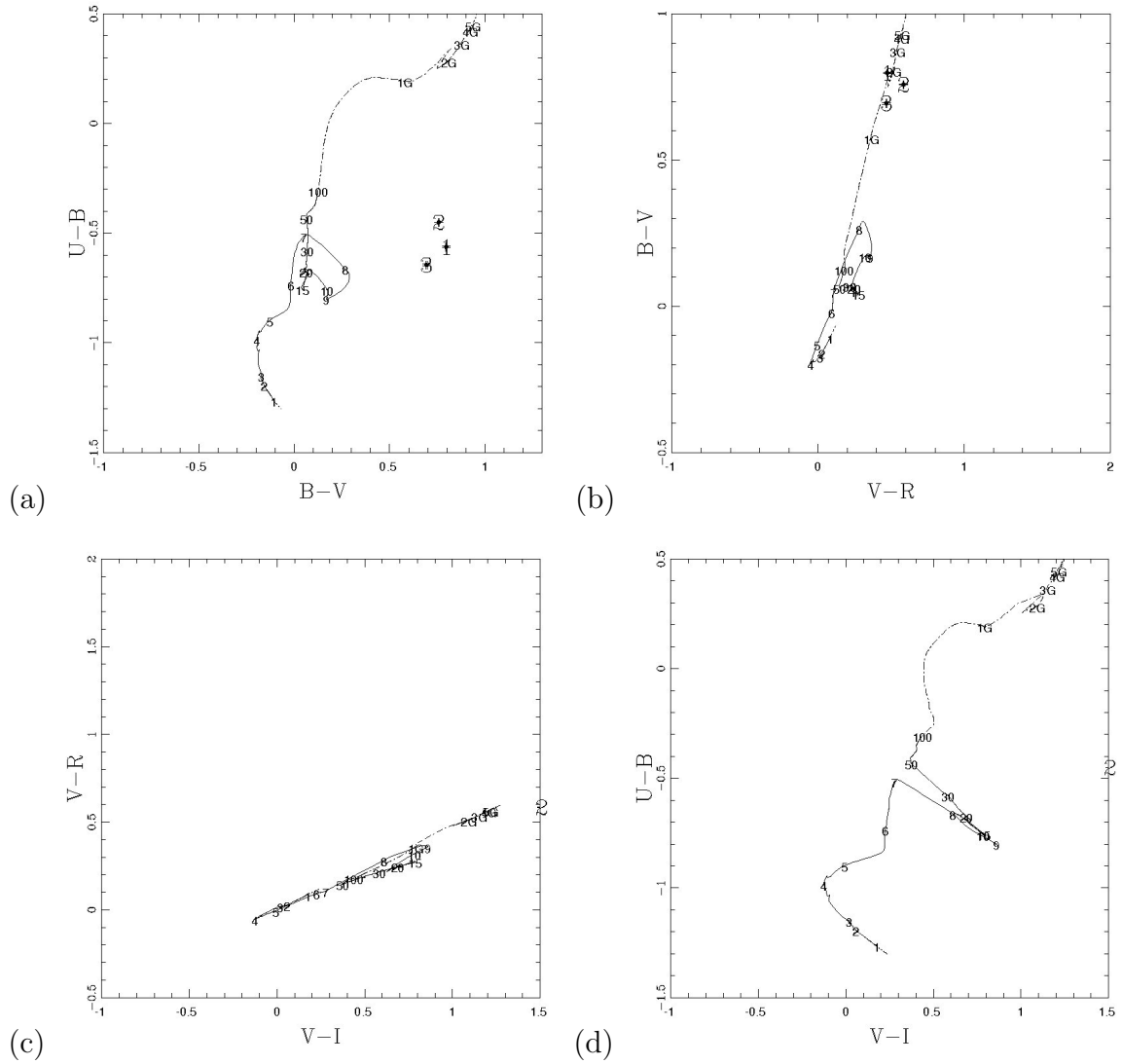


FIGURE 5.9: Foreground corrected colour-colour plot of the galaxy NGC 6764, for the metallicity  $z=0.008$ ; (a) U-B Vs B-V (b) B-V Vs V-R (c) V-R Vs V-I (d)U-B Vs V-I



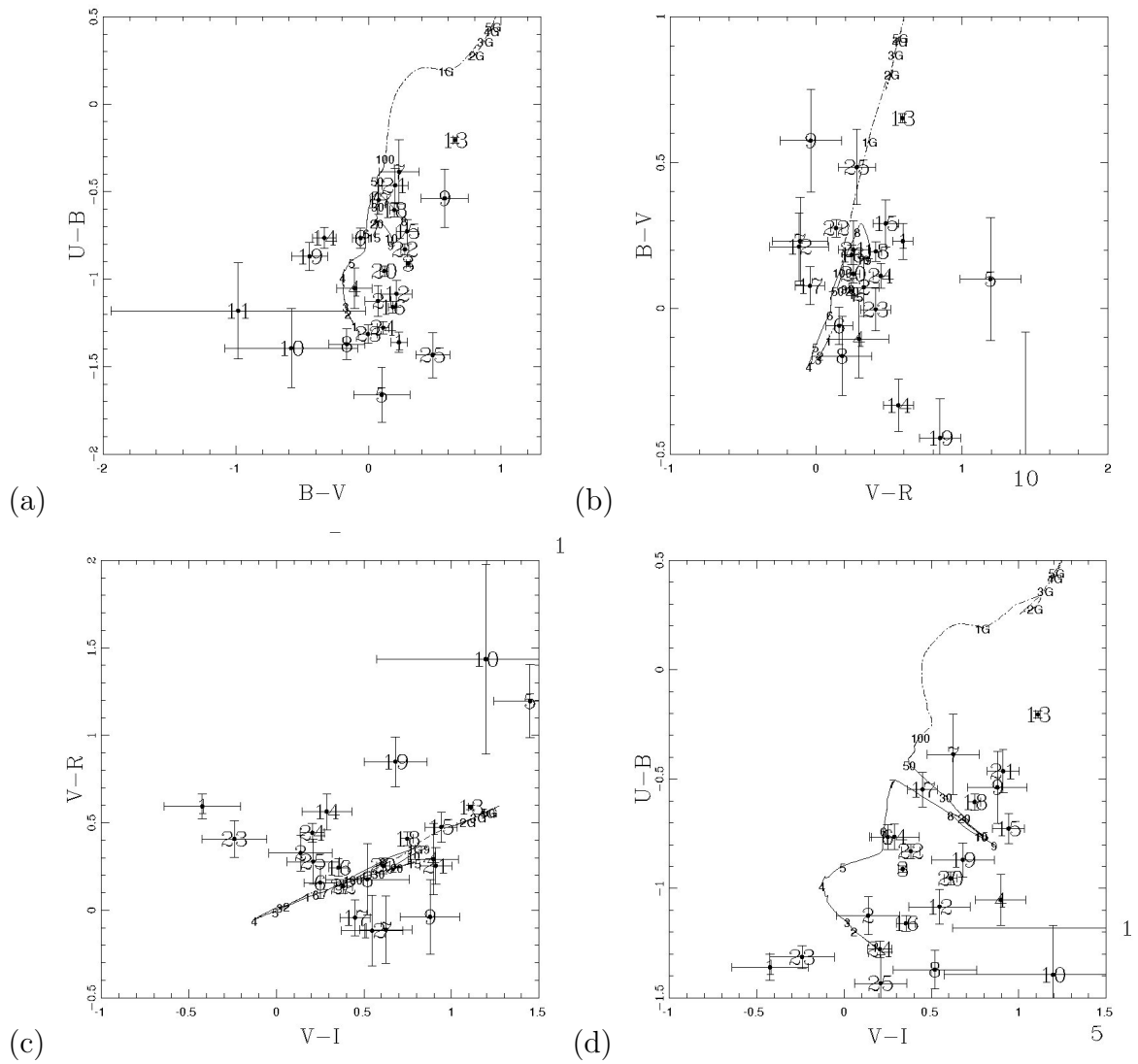


FIGURE 5.11: Foreground corrected colour-colour plot of the galaxy NGC 3003, for the metallicity  $z=0.008$ ; (a)  $U-B$  Vs  $B-V$  (b)  $B-V$  Vs  $V-R$  (c)  $V-R$  Vs  $V-I$  (d)  $U-B$  Vs  $V-I$

# Chapter 6

## Analysis of individual galaxies

### 6.1 NGC 1140

NGC 1140 is a SbPec galaxy located at a distance of 17.9 Mpc. It is an object showing blue colors,  $B - V = 0.01 \pm 0.02$  mag, and intermediate metallicity,  $12 + \log(\text{O}/\text{H}) = 8.38 \pm 0.10$ . [Hunter et al. \(1994a\)](#) used optical broad-band images,  $\text{H}\alpha$  data, optical spectroscopy and neutral hydrogen observations to identify the central giant star forming region and a chain of other star forming regions coinciding with the low light level extension in the south-west tail of the galaxy (see [Fig. 3.1](#)). Later, [Hunter et al. \(1994b\)](#) used HST data to show that the central region consists of a supergiant H II region and few super-star clusters with sizes of  $< 10$  pc. With our ground-based images it is not possible to resolve the individual clusters observed by the HST in the central giant H II region and hence it has been considered as a single star forming region (knot #1). The other star forming knots numbered #2, #3 and #4, which are in the south-west part of the galaxy, also show very blue colours. In fact knots #3 and #4 are bluer than the central knot. The bluer colour of the outer body of the galaxy indicates that extensive star formation is going on throughout this galaxy. The age of the most recent burst and the stellar populations decrease from the center ( $\sim 6.2$  Myr and

500 Myr) to the external regions ( $\sim 3.7$  Myr and 100 Myr) of NGC 1140, suggesting that the arc-like plume where they are located has been originated very recently. WR features were previously detected in NGC 1140 by [Guseva et al. \(2000\)](#) and [Moll et al. \(2007\)](#). We clearly see both the blue and red WR bumps (see Figs. 4.10 and 4.11). As it was discussed before, the derived WR properties within NGC 1140 agree well with those expected for a galaxy with its metallicity [López-Sánchez & Esteban \(2010a\)](#).

The star formation rates calculated using the  $H\alpha$  flux for the four knots reveals that the central region is undergoing an intense burst of star formation, while the other three star forming knots have moderate rate of star formation. Our estimation of the SFR within this galaxy,  $\sim 0.43 M_{\odot}/\text{yr}$ , agrees with that previously determined by [Hunter et al. \(1994b\)](#) and with [Moll et al. \(2007\)](#). Our data also confirms that the age of the burst decreases from the nuclear region to the external areas. FIR and 20-cm radio-continuum data are available for this galaxy. Using the flux densities for  $60 \mu\text{m}$  and  $100 \mu\text{m}$  provided by IRAS (*Infrared Astronomical Satellite*, [Moshir et al. 1990](#)) and applying the relations provided by [Condon \(1992\)](#) and [Kennicutt \(1998\)](#), we derive  $\text{SFR}_{60 \mu\text{m}} = 0.25 M_{\odot} \text{yr}^{-1}$  and  $\text{SFR}_{\text{FIR}} = 0.30 M_{\odot} \text{yr}^{-1}$ , respectively. On the other hand, considering the 1.4 GHz flux for this galaxy provided by [Hunter et al. \(1994a\)](#) and the [Condon, Cotton & Broderick \(2002\)](#) calibration, we derive  $\text{SFR}_{1.4 \text{GHz}} = 0.20 M_{\odot} \text{yr}^{-1}$ . All these SFR values agree with our  $H\alpha$ -based SFR.

Considering the enhancement of SF activity in its center and its peculiar optical and HI morphology. [Hunter et al. \(1994a,b\)](#) concluded that NGC 1140 is undergoing recent violent disturbances which may be explained assuming a merger of two low surface brightness galaxies. Our new data agrees with this scenario. Hence, NGC 1140 seems to be another example of a WR galaxy in which starburst has been triggered by galaxy interactions, as it was found in the majority of the objects analyzed by [López-Sánchez \(2010\)](#).

## 6.2 IRAS 07164+5301

**IRAS 07164+5301** is known as an extreme starburst source. (?). The optical spectrum of the galaxy was previously studied by [Huang et al. \(1996\)](#) but the broad-band colours of IRAS 07164+5301 are analyzed here for the first time. We derive a somewhat blue colours in this galaxy,  $U - B = -0.47 \pm 0.05$ ,  $B - V = -0.16 \pm 0.04$ . The comparison of the derived optical colours with the stellar population synthesis models and the analysis of the equivalent width of the  $H\alpha$  emission line provide an age of  $\sim 5.6-7$  Myr for the most recent star-formation event in this galaxy. However, our broad-band colours also identify an underlying old stellar population with ages between 500 and 800 Myr. The youth of the starburst agrees with the detection of WR features in the optical spectrum of the galaxy analyzed by [Huang et al. \(1996\)](#), who reported the presence of broad lines around  $4686 \text{ \AA}$  suggesting  $N \text{ III } \lambda 4640$ ,  $C \text{ III } \lambda 4650$  and  $He \text{ II } \lambda 4686$ . These authors also indicated a tentative detection of  $O \text{ V } \lambda 5835$  and a lack of  $C \text{ IV } \lambda 5808$ . However, our spectrum does not allow the detection of any spectral features.

Using our optical spectrum, we compute a radial velocity of  $V_r = 12,981 \text{ km s}^{-1}$  (redshift  $z = 0.0433$ ) for IRAS 07164+5301. Hence, this galaxy lies at a distance of 177 Mpc. The high radial velocity this galaxy possesses is the reason we cannot detect its emission using the rest-frame filter. However, we used the flux of the line observed in our optical spectrum to estimate a SFR of  $\sim 7.8 M_{\odot} \text{ yr}^{-1}$ . Using the FIR and 20 cm radio-continuum data available for this galaxy, we derive  $\text{SFR}_{60 \mu m} = 8.3 M_{\odot} \text{ yr}^{-1}$ ,  $\text{SFR}_{\text{FIR}} = 8.1 M_{\odot} \text{ yr}^{-1}$ , and  $\text{SFR}_{1.4 \text{ GHz}} = 5.7 M_{\odot} \text{ yr}^{-1}$ . The 1.4 GHz data were provided by [Condon et al. \(1998\)](#). All these values are in excellent agreement with the SFR we have estimated here using the  $H\alpha$  emission.

Using several empirical calibrations we derive an oxygen abundance of  $12 + \log(O/H) = 8.50$  for IRAS 07164+5301. This value is much lower than the previous estimation of its metallicity provided by [Huang et al. \(1996\)](#), who derived  $12 + \log(O/H) = 8.96$ . Taking into account that we have estimated the oxygen

abundance of this object using several parameters ( $N_2$ ,  $N_2O_3$ ,  $R_{23}$ ,  $P$ ) and calibrations, all giving similar values (except for the caveat of those methods based on photoionization models, as we discussed before) we consider that our metallicity estimation of IRAS 07164+530 is more appropriate than that obtained by [Huang et al. \(1996\)](#).

### 6.3 NGC 3738

NGC 3738 is classified as an irregular ([de Vaucouleur et al. 1991](#)), low-metallicity galaxy. As it has a very low radial velocity,  $V_r=229 \text{ km s}^{-1}$ , it is not easy to estimate the distance to this galaxy, and hence its distance estimations are ranging from 4 to 5.4 Mpc ([Hunter 1982](#); [Hunter, Gallagher & Rautenkranz 1982](#); [Hunter & Hoffman 1999](#)). The distance value tabulated in Table 2.2 for this galaxy,  $d=5.56$  Mpc, comes just from the value of the Hubble constant. However, the most recent distance estimation for this galaxy using the luminosity of the tip of the red giant branch stars is 4.90 Mpc ([Karachentsev et al. 2003](#)).

The optical spectrum of NGC 3738 resembles those of H II regions with emission dominated by massive, hot stars. [Martin \(1997\)](#) points out the presence of a broad He II  $\lambda 4686$  emission line in the integrated spectrum of this galaxy, and hence NGC 3738 was also listed as WR galaxy by [Schaerer et al. \(1999\)](#). Our optical spectrum does not allow us to detect the faint WR features. However, we can use the bright emission lines to estimate the metallicity of the galaxy,  $12+\log(\text{O}/\text{H})=8.51$ . This value is rather high when comparing the oxygen abundance derived by [Martin \(1997\)](#), which was  $12+\log(\text{O}/\text{H})=8.23$ . Deeper optical spectra of NGC 3738 are needed to clarify this issue.

NGC 3738 has a bright star forming region in center, for which we derive a SFR of  $0.023 M_{\odot} \text{ yr}^{-1}$ . This value agrees well with the SFR estimation provided using the H $\alpha$  flux provided by [Kennicutt et al. \(2008\)](#) for this galaxy,  $0.030 M_{\odot} \text{ yr}^{-1}$ . Using the FIR fluxes available for this galaxy and the same

equations cited in the previous subsection, we derive  $\text{SFR}_{60\mu\text{m}}=0.015 M_{\odot}\text{yr}^{-1}$  and  $\text{SFR}_{\text{FIR}}=0.018 M_{\odot}\text{yr}^{-1}$ . These SFR determinations are also in agreement with the SFR value we derived using our  $\text{H}\alpha$  images. The age of the most recent star-formation event we estimate for this galaxy following its  $EW(\text{H}\alpha)$  is  $7.4\pm 0.1$  Myr. This age estimation agrees with that obtained using the  $U - B$  colors, although from  $B - V$  and, specially,  $V - R$  and  $V - I$  colors we expect that a stellar population with age older than 400-500 Myr are also present in the galaxy.

## 6.4 UM 311

**UM 311** is an intriguing extragalactic H II region which shows a radial velocity of  $V_r=1,675 \text{ km s}^{-1}$ . Hence, it is located at a distance of 18.7 Mpc. An essential note in NED defines UM 311 as an ‘‘H II region in the GPair CGCG 0113.0-0107’’. Our optical images (see Fig. 3.8) clearly show two galaxies in apparent interaction, a spiral galaxy (NGC 405) and a dwarf elliptical at its NE (UGC 807), which have radial velocities of  $1,761 \text{ km s}^{-1}$  and  $11,431 \text{ km s}^{-1}$ . Therefore, these two galaxies are not physically associated. Because of the very similar radial velocity, UM 311 may indeed be an H II region within NGC 405. However, its observed properties (blue colours, compactness and intensity of the star-formation activity) does not discard the possibility that it is an independent Blue Compact Dwarf Galaxy (BCDG) which is interacting with the spiral galaxy NGC 405. A similar example of a BCDG interacting with a spiral galaxy is the stunning NGC 1512 / NGC 1510 system (Koribalski & López-Sánchez 2009). Interferometric HI data are needed to completely elucidate this issue.

The first report of WR stars within UM 311 was done by Masegosa, Moles & del Olmo (1991) as they detected the broad He II  $\lambda 4686$  emission line. Later, many authors have analyzed the WR content of this object: Izotov & Thuan (1998) confirmed the presence of both the blue and red WR bumps in UM 311.

Guseva et al. (2000) noticed that the blue WR bump was particularly strong in this object. Pindao (1999); Buckalew et al. (2005); Zhang et al. (2007) and Brinchmann, Kunth & Durret (2008) also included UM 311 in their studies of WR galaxies. However, the poor quality of our optical spectrum does not allow to detect the faint broad features attributed to WR stars. UM 311 has been also used in the analysis of the chemical abundances of low-metallicity extragalactic H II regions (e.g. Izotov & Thuan 1998, 1999; Izotov et al. 2004; Izotov et al 2006; Pilyugin 2001a) and hence its oxygen abundance has been determined with good precision,  $12+\log(\text{O}/\text{H})=8.31\pm 0.04$  (Izotov & Thuan 1998). Using several empirical calibrations and the data provided by our optical spectrum, we estimate that the oxygen abundance of UM 311 is  $12+\log(\text{O}/\text{H})=8.27$ , in excellent agreement with the previous estimations.

Using our H $\alpha$  images, we derive a SFR of  $0.044 M_{\odot} \text{yr}^{-1}$ . This value is pretty low when comparing with the SFR derived by Hopkins, Schulte-Ladbeck & Drozdovsky (2002) using FIR and radio-continuum data,  $\text{SFR}_{60\mu\text{m}}=1.5 M_{\odot} \text{yr}^{-1}$  and  $\text{SFR}_{1.4\text{GHz}}=1.1 M_{\odot} \text{yr}^{-1}$ . However, we consider that our SFR estimation is more appropriate, as both FIR and radio-continuum images do not enough spatial resolution to resolve UM 311 within the spiral galaxy NGC 405. Finally, our analysis of the stellar populations within UM 311 suggests it possesses both a very young stellar population and an important underlying old stellar population, this one perhaps coming from the spiral disc of NGC 405. Indeed, the estimated age for the most recent star-formation event in UM 311 is 3 Myr, using both the  $EW(\text{H}\alpha)$  and the  $U - B$  color. However, the rest of the optical colours clearly indicate that stars with ages older than 500 Myr are also present in UM311.

## 6.5 NGC 6764

NGC 6764 is barred spiral (SBb type) galaxy (see Fig.3.9) which is also classified as a classical LINER galaxy (Guseva et al. 2000; Alonso-Herrero et al.

2000). Indeed, using optical emission line ratios we confirm that the nucleus of this galaxy lies in the LINER region of the BPT diagram (Fig. 4.14). Osterbrock & Cohen (1982) point out the presence of broad N III  $\lambda$ 4640 and He II  $\lambda$ 4686 emission lines in the spectrum of the nucleus of NGC 6764. These features were later reported by Eckart et al. (1996); Guseva et al. (2000) and Fernandes et al. (2004). Osterbrock & Cohen (1982) also reported a signal excessive widths of He I  $\lambda$ 5876 and H $\alpha$  which they attributed to emission from WR stars. Indeed, broad C III  $\lambda$ 5696 and C IV  $\lambda$ 5808 lines from WC stars were discovered by Fernandes et al. (2004). Our optical spectrum confirms the broad features in the blue WR bump, although the presence of the red WR bump is not clear (see Fig.4.7). The presence of WR stars make this galaxy one of the most significant examples of a starburst-dominated classical LINER (Guseva et al. 2000).

The starburst activity in NGC 6764 was first observed by Eckart et al. (1991, 1996), who revealed a dense concentration of molecular gas and very recent (few tens of Myr) starburst at the nucleus of NGC 6764. These are the age estimations ( $\sim$ 20-50 Myr) we derive for the young population of this galaxy using the  $U - B$  color. Leon et al. (2007) recently analyzed the interplay between the central activity and the molecular gas within NGC 6764, finding that the nuclear starburst is 3-7 Myr old. However, the rest of the optical colours indicate the presence of a very important old stellar population underlying the bursts, with ages older than 1 Gyr. From our H $\alpha$  images we identify 3 regions showing ionized gas emission: the center of the galaxy (knot #2) and the regions located at the end of the bar (knot #3 at the east; knot #1 at the west). Knot #1 shows a SFR of  $\sim 1.5 M_{\odot} \text{ yr}^{-1}$  and hosts a star-formation activity that started  $\sim 8.4$  Myr ago.

We cannot compute the oxygen abundance of the nucleus of the galaxy because its LINER nature. However, we derive a metallicity of  $12 + \log(\text{O}/\text{H}) = 8.65$  for knot #3 using several independent empirical calibrations. So far, this is the first gas-phase metallicity estimation reported in this galaxy.

## 6.6 NGC 4861

NGC 4861 is classified as a Magellanic irregular galaxy (Sandage & Tammann 1981) and a BCDG because of its blue colours and high UV continuum (French 1980; Thuan & Martin 1981). This object is located at a distance of 12.9 Mpc. NGC 4861 has a comet-like morphology (see Fig.3.11) with many star-forming regions located along its major axis. The morphology of the galaxy was discussed by Dottori et al. (1994) who concluded that NGC 4861 might have undergone a merger process. From HI maps, this galaxy is an edge-on and rotating disk system (Conselice et al. 2000). Some authors have distinguished the bright star-forming region at its south (our knot #1) as NGC 4861 and the dwarf irregular galaxy IC 3961 (the rest of the galaxy) and recommended the definition of Mkn 59 to describe the full system. In any case, NGC 4861 has been amply studied as an example of a compact blue galaxy (e.g. Kobulnicky & Skillman 1998; Izotov et al. 1997; Izotov & Thuan 1999; Lee, Salzer & Melbourne 2004; Esteban et al. 2009).

Since the discovery of the broad He II  $\lambda 4686$  emission line in the spectrum of this galaxy (Dinerstein & Shields 1986), many studies have confirmed the presence of WR stars in NGC 4861 (Schaerer et al. 1999) and also detected the broad C IV  $\lambda 5808$  emission (Izotov et al. 1997; Guseva et al. 2000). Our optical spectrum also shows these broad WR features, and hence we derived  $WR/(WR+O)=0.062$  and  $WCE/WNL=0.30$ , in agreement with previous estimations. The most recent analysis of the ionized gas within this object was presented by Esteban et al. (2009), who derived an oxygen abundance of  $12+\log(O/H)=8.05\pm 0.04$  using many nebular and auroral emission lines from optical spectra obtained with the 10m Keck I telescope. Although slightly higher than the value we derive here using the emission lines observed in our optical spectrum (including the auroral [O III]  $\lambda 4363$  line),  $12+\log(O/H)=7.95\pm 0.05$ , both measurements agree well.

The analysis of our  $H\alpha$  images allows us to quantify the star-formation activity throughout NGC 4861. The net- $H\alpha$  image (Fig.3.12) reveals 12 well-defined star-forming regions. Bright knot #1 hosts the majority of the starburst activity. For this region we derive a SFR of  $\sim 0.31 M_{\odot} \text{yr}^{-1}$  using the  $H\alpha$  luminosity. The SFR obtained from the available FIR and 1.4 GHz data are quite low,  $\text{SFR}_{60\mu m} = 0.086 M_{\odot} \text{yr}^{-1}$  and  $\text{SFR}_{1.4\text{GHz}} = 0.049 M_{\odot} \text{yr}^{-1}$ , compared with our  $H\alpha$ -based estimation of the SFR. This may suggest that there has been a very recent enhancement of the star-formation activity within this object. Using the  $EW(H\alpha)$ , we determine that the most recent starburst event happened  $\sim 6$  Myr ago. The ages determined for the rest of the regions within NGC 4861 are very similar. The study of the  $U - B$  colour also gives ages of 3-8 Myr for the majority of the knots. However all possess an important old stellar population underlying the bursts, with ages sometimes reaching up to 1 Gyr. The main age derived using the  $B - V$  and  $V - R$  colors is around 100-200 Myr. This fact together with the presence of strong absorption features in the optical spectrum of the galaxy indicate the presence of an intermediate-age stellar population in this BCDG.

## 6.7 NGC 3003

**NGC 3003** is a SBbc type galaxy located at 24 Mpc which appears to be almost edge-on (see Fig 3.14) . Its morphology shows two asymmetric spiral arms, suggesting that it may be a disturbed galaxy. Its SW areas show a bright and compact region which may be the remnant of a dwarf galaxy, also it may also be just an intense H II region within the spiral arms of NGC 3003.

Ho et al. (1995) reported the presence of the broad blue WR bump in NGC 3003, and therefore the galaxy was included in the WR galaxy catalogue created by [Schaerer et al. \(1999\)](#). This feature has not been observed again in this galaxy. Indeed it is not seen in our optical spectrum, however it has a very

low S/N ratio. Using the brightest emission lines and the typical empirical calibrations, we derive an oxygen abundance of  $12+\log(\text{O}/\text{H})=8.57$  for this galaxy. Besides NGC 3003 has been amply studied before, we have not found in the literature any other estimation of its gas-phase metallicity.

Our net- $\text{H}\alpha$  image allows us to identify 25 independent star-forming regions, including the bright nucleus (knot #13) and the intriguing bright object at the SE (knot #3). These two knots actually host the highest  $\text{H}\alpha$  emission of the galaxy. The total  $\text{H}\alpha$  luminosity of the galaxy adding up the flux of all star-forming region is  $2.97 \times 10^{40} \text{ erg s}^{-1}$ , which can be translated in a total SFR of  $0.16 M_{\odot} \text{ yr}^{-1}$ . Our derived  $\text{H}\alpha$  luminosity is 4 times lower than that derived by [Hoopes, Walterbos & Rand \(1999\)](#) who reported  $L_{\text{H}\alpha} = 1.18 \times 10^{41} \text{ erg s}^{-1}$ . Some part of the missing  $\text{H}\alpha$  flux may be consequence of not considering an adequate value for the correction for extinction, which may be important in edge-on galaxies. However, we should also expect that there is some diffuse  $\text{H}\alpha$  gas in the galaxy which does not belong to the analyzed regions and hence it was not considered in our total flux. The SFR derived from the FIR and radio-continuum data available for this galaxy are  $\text{SFR}_{60\mu\text{m}} = 0.39 M_{\odot} \text{ yr}^{-1}$ ,  $\text{SFR}_{\text{FIR}} = 0.15 M_{\odot} \text{ yr}^{-1}$ , and  $\text{SFR}_{1.4\text{GHz}} = 0.58 M_{\odot} \text{ yr}^{-1}$ . All these values suggest that the total  $\text{H}\alpha$  luminosity computed by [Hoopes et al. \(1999\)](#), who translates in a SFR of  $0.64 M_{\odot} \text{ yr}^{-1}$ , may be slightly overestimated.

We also estimated the age of the most recent star-formation event via the  $\text{H}\alpha$  equivalent width, finding typical values between 5 and 7 Myr. The youngest ages are found in the center of the galaxy and in knot #3.  $U - B$  colours also indicate a typical age between 5 and 50 Myr for the young stellar population, although following the  $B - V$  and  $V - R$  colors the majority of the knots seem to have an older stellar population, with an age usually higher than 1 Gyr, underlying the bursts.

# Chapter 7

## Summary, Conclusions and Future Prospects

### 7.1 Summary

The presented thesis work deals with extra galactic objects which means the galaxies observed at a certain far away distance from the Milky way (Our own Galaxy). These studies are carried out in optical regions for a sample of seven wolf-rayet galaxies.

These Wolf-Rayet (WR) galaxies are defined as those galaxies which show broad emission features associated to WR stars in their integrated spectra. The presence of the Wolf-Rayet stars are reflected in galaxy spectrum as two important broad features, the blue WR bump (between 4650 - 4690 Å, mainly due to N III, N V and He II) and the red WR bump (at  $\sim 5808$  Å, due to C IV emission line). The nebular He II  $\lambda 4686$  is also associated to the presence of these massive stars, however other ionization mechanisms may also create this line, as discussed by Garnett et al. (1991); Garnett (2004); Guseva, Izotov & Thuan (2000) and López-Sánchez & Esteban (2010a). Wolf-Rayet galaxies were first cataloged by Conti (1991) and later by Schaerer, Contini & Pindao (1999), but hundreds of

these objects were found using the *Sloan Digital Sky Survey*, SDSS (Zhang et al. 2007; Brinchmann, Kunth & Durret 2008). The morphological type of WR galaxies varies from the low-mass blue compact dwarf (BCD) irregular galaxies, to massive spirals and luminous merging galaxies. WR features are often found in starburst galaxies. The progenitors of the Wolf-Rayet stars are the most massive ( $M \gtrsim 25 M_{\odot}$ ), luminous ( $10^5$  to  $10^6 L_{\odot}$ ) and hot ( $\sim 50,000$  K) O stars, and they finalize their days exploding as type Ib/Ic supernovae (Meynet & Maeder 2005). Actually, the minimum stellar mass that an O star needs to reach the WR phase and its duration depends on the metallicity. In general, the WR phenomenon is short lived, it exists only for  $\leq 1$  Myr. Hence, the detection of WR features in the spectra of a galaxy constrains the properties of the star-formation processes. Because the first WR stars typically appear around 2 – 3 Myr after the starburst is initiated and disappear within some 5 Myr (Meynet & Maeder 2005), their detection informs about both the youth and strength of the burst, offering the opportunity to study an approximately coeval sample of very young starbursts (Schaerer & Vacca 1998), but also to study the formation and impact of massive stars in starburst galaxies (Guseva et al. 2000; Fernandes et al. 2004; Buckalew et al. 2005; López-Sánchez & Esteban 2010a,b) and the role that interaction with or between dwarf galaxies and/or low surface brightness objects plays in the triggering mechanism of the star-formation activity (López-Sánchez & Esteban 2008; López-Sánchez 2010).

With the aim of getting a better understanding of the properties of the Wolf-Rayet (WR) galaxies, we have performed a detailed analysis of a sample of these objects using broad-band  $U, B, V, R, I$ , narrow-band  $H\alpha$  imaging and low-resolution optical spectroscopy. In this thesis we present the results of 7 analyzed WR galaxies. We compile the main properties of these objects. The thesis is organized as follows: observations and data reduction are described in Chapter 2. The narrow-band photometric results are presented in Chapter 3. This section includes the identification of the star-forming regions, and the estimation of the both the SFR and the most recent star-forming episode via the analysis of the

H $\alpha$  images. Chapter 4 describes our results from optical spectroscopy. We here analyze the physical conditions of the ionized gas (reddening, nature of the ionization, electron density and electron temperature when possible) and compute the oxygen abundances of the ionized gas within our sample galaxies. Chapter 4 also includes the analysis of the WR features in NGC 1140 and NGC 4861. Chapter 5 discusses about the Broad-band photometry results and the determinations of their optical colours. And also about how we determined the ages of both the old and young stellar populations. We also present the analysis of the individual galaxies in Chapter 6. Finally, we list our summary and conclusions in Chapter 7.

## 7.2 Conclusion

- We presented a detailed photometric and spectroscopic study of sample of 7 Wolf-Rayet galaxies. The observed galaxies are NGC 1140, IRAS 07164+5301, NGC 3738, UM 311, NGC 6764, NGC 4861 and NGC 3003. Star-forming regions within these galaxies have been identified using narrow-band H $\alpha$  images. Combining with the data obtained using our optical broad-band images, we analyze the morphologies, colours, star-formation rates and stellar populations of these star-forming regions.
- We discussed the morphology of the galaxies using our broad-band images. In some cases (NGC 1140, UM 311, NGC 4861 and NGC 3003) we find features which may indicate that the galaxy has experienced a recent interaction.
- We used the H $\alpha$  images and optical broad-band colours in combination with Starburst99 models to trace the age of both the young and old underlying stellar populations within all these regions, and derive the age of the

most recent star-formation event. We confirm that almost all the analyzed regions show a very young ( $<10$  Myr) burst on top of an older ( $\sim 500$  Myr – 1 Gyr) stellar population.

- The  $H\alpha$ -based SFR derived for each galaxy usually agrees well with the SFR derived using FIR and radio-continuum data. These values confirm the starbursting nature of all the analyzed objects.
- The optical spectra have been used to search for the faint WR features, to confirm that the ionization of the gas is consequence of the massive stars, and to quantify the chemical properties of each object.
- The high S/N optical spectrum of NGC 1140 and NGC 4861 allowed us to precise the oxygen abundance of the ionized gas using the direct method (i.e., via the detection of the faint [O III]  $\lambda 4363$  emission line). We also derive the chemical abundances of N, S, Ne and Ar in these two galaxies. In NGC 4861, the N/O ratio is  $\sim 0.3$ - $0.4$  dex higher than that expected from its oxygen abundance. This fact may be related to the presence of WR stars within this galaxy. Indeed, we clearly detected the features originated by WR stars in NGC 1140 and NGC 4861 and used them to derive the population of O, WNL and WCE stars following the recipes described in [López-Sánchez & Esteban \(2010a\)](#). In both cases, the derived WR/(WR+O) and WCE/WNL ratios agree well with those expected for galaxies with the oxygen abundances derived.
- For the rest of the galaxies we also provide an estimation of the oxygen abundance of the ionized gas using several and independent empirical calibrations. Here we present the first oxygen abundances computed

---

for NGC 6764 and NGC 3003, which are  $12+\log(\text{O}/\text{H})=8.65$  and  $8.57$ , respectively. We also precise the oxygen abundance of IRAS 07164+5301,  $12+\log(\text{O}/\text{H})=8.50$ , which is  $\sim 34\%$  of the only available determination of the metallicity of this galaxy.

## 7.3 Future Prospects

### 7.3.1 Continuation of Optical studies

**(Using new Models and Archival data)** Similar work is planned for a sample of a few more WR galaxies. such as NGC 2403, NGC 3995, NGC 5430 and MRK 1236. Observations of these objects have been made already. Partially the narrow band photometry work has been done for this and spectroscopy and Broad-band work is yet to be done. Mean while, HST (Hubble Space Telescope) data with high resolution images of the same star forming regions(knots) are planned to be analyze. Also, a special study has to be taken for NGC 2403 in detail, which is having almost more than 25 star forming regions in it. This will be interesting to carry out for further work, since the spectroscopic observations also has been taken for many star forming regions. The study in chemical abundances variation among the galaxies within different red shift and within the same galaxy but in different spiral arms is also planned to study. Also, working with the other available models such as PEGASE and SED (Spectral Energy Distribution) through determining the ages. And, using GALFIT and SExtractor (astronomical data reduction) softwares. to study the galaxy morphology in detail along with the spectroscopy analysis through available SDSS data.

### 7.3.2 Multiwavelength Studies of Galaxies

Since, the sufficient information has been occurred for this presented work through optical observations, further plans are to explore in other wavelength regions of all kind of Galaxies. Particularly, planned to explore in radio wavelengths regions of the galaxies. Some time it is very difficult to get complete understanding of the galaxies by looking through optical telescopes alone to investigate the regions of star formation within the dusty regions. However, radio waves can penetrate through the dusty regions to reveal the underneath information of the galaxies.

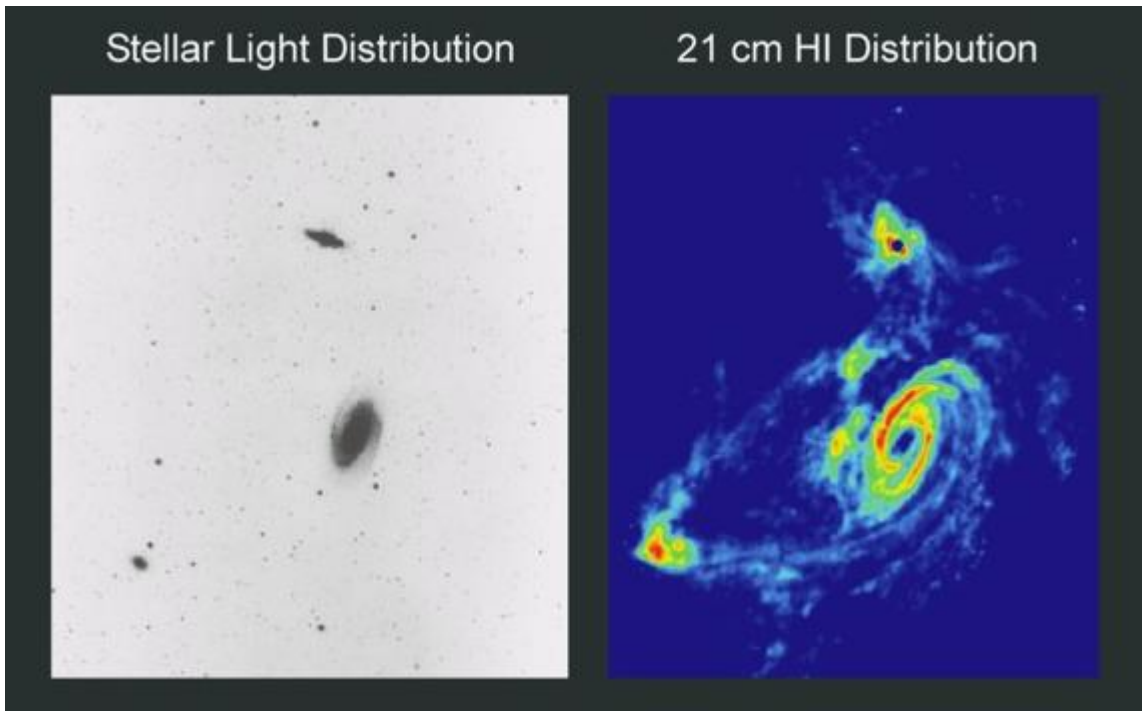


FIGURE 7.1: An example for advantage of Multiwavelength studies in galaxies

This is a picture of the entire M81 group (Fig. 7.1). This is a very good example for the usage of two different wavelength studies. The left image is the optical part of the spectrum while the right image of the galaxies was taken in the radio part of the spectrum. Here the intensity of the radiation is coded by the false color, the brighter regions appear red in this image and the dimmer regions are colored blue. This particular spectral line of radiation with a wavelength of 21cm is dominated by an emission line characteristic of neutral hydrogen gas. Therefore studying this line allows us to track how the gas in this group of galaxies is being affected by their interaction. M81 is the large spiral near the center of the image, M82 lies above M81 in this image and NGC 3077 is the small galaxy off to the left. The long tails of hydrogen that can be seen connecting the galaxies are caused by tidal interactions that happen as a result of the galaxies being so near to each other, these same interactions are causing the rapid star formation in M82. Tidal interactions are caused when two objects interact gravitationally. Because the strength of the gravitational interaction depends on the distance between two objects the close sides of the two objects feel the pull stronger than

the far sides of the objects. This difference in the gravitational force is what causes the tidal tails that you see. Hence from the above example it clearly shows the importance of radio observations especially for my type of work, to locate the interacting galaxies.

### 7.3.3 Proping the AGN-Starburst Connection

The nature of the dominant ionizing source in Active Galactic Nuclei (AGNs) is still poorly understood. Under the unified scenario, Seyfert 1 and Seyfert 2 galaxies represent the same kind of objects seen from different angles by the observer. In Seyfert 1 galaxies, one sees the central engine (a black hole surrounded by an accretion disc) whereas in Seyfert 2 galaxies a dusty torus completely blocks the non-thermal phenomenon. On the other hand, it has been suggested that starbursts may play an important role in the Seyfert phenomenon. In this case, AGNs are in various distinct evolutionary phases of a burst of star formation in the core of early-type spiral galaxies. Physical processes associated with the starburst phenomenon can in principle account for most of the AGNs properties. (Chap. 1.1.3) In an hybrid version that take advantage of both views, a very compact circum nuclear starburst coexists with a massive central black hole responsible for the ionizing continuum. (Kunth & Contini 1999).

In this still some fundamental question remains to be answered. Like, Are the non-thermal nuclear activity and the circumnuclear starbursts connected? WR signatures in AGNs UV studies have open new ways of studying the possible presence of a powerful starburst in AGNs. However, UV-bright Seyfert 2 galaxies are not so numerous, mostly because of dust obscuration, hence detailed UV observations are difficult to achieve even with the HST. This is why we believe that Wolf-Rayet (WR) stars are excellent tracers to follow up in relation with the AGN-starburst phenomenon, mainly because they provide, in turn, conspicuous signatures in the visible. The detection of the broad emission feature at He II 4686Å is indeed attributed mainly to WR stars of WN subtype,

whereas C IV 5808Å, the strongest emission line of WC stars, is observed in WR galaxies (Schaerer, Contini & Kunth 1999). Moreover, although they represent only a special short lived phase in the evolution of the starburst population, their occurrence is highly expected in metal-rich environment.

These same questions can be replaced in other way around; Like, Are there any evolutionary connections among the three types of galactic nuclei ? If this is the case, we have further important questions; How are they connected ? What are important physical processes in such connections ? Indeed, many astronomers, have been enslaved by the so-called starburst-AGN connection. (a) Massive stars formed in a nuclear starburst evolve through hot phases (i.e., Wolf-Rayet stars, planetary nebula nuclei, and so on) to supernova explosions inevitably. Therefore, we have to take account of all the evolutionary phases when we discuss the evolution of starburst nuclei. (b) Compact remnants (i.e., stellar-sized black holes and neutron stars) are also inevitably remained in the nuclear starburst region. Therefore, we have to think about the dynamical evolution of such remnants under a realistic gravitational potential together with dynamical interactions with existing stars in the concerned region. Careful consideration on these two points makes it possible to discuss the starburst-AGN connection.

So this curiosity made me to take up this topic for further extension to my current work and as for my future work. So, I wish to explore in AGN studies and AGN-starburst connection as a extension to this work. Which will give a very good understanding about the total systems of galaxies evolution and histories. I have already taken initiative being part of the study of the rapid optical variability of blazars, which is an important topic of further studies related to AGN-starburst connection. (Gopal-krishan *including chrisphin karthick et al 2011*).



## Appendix A

### HCT- H $\alpha$ Filter Response Curve

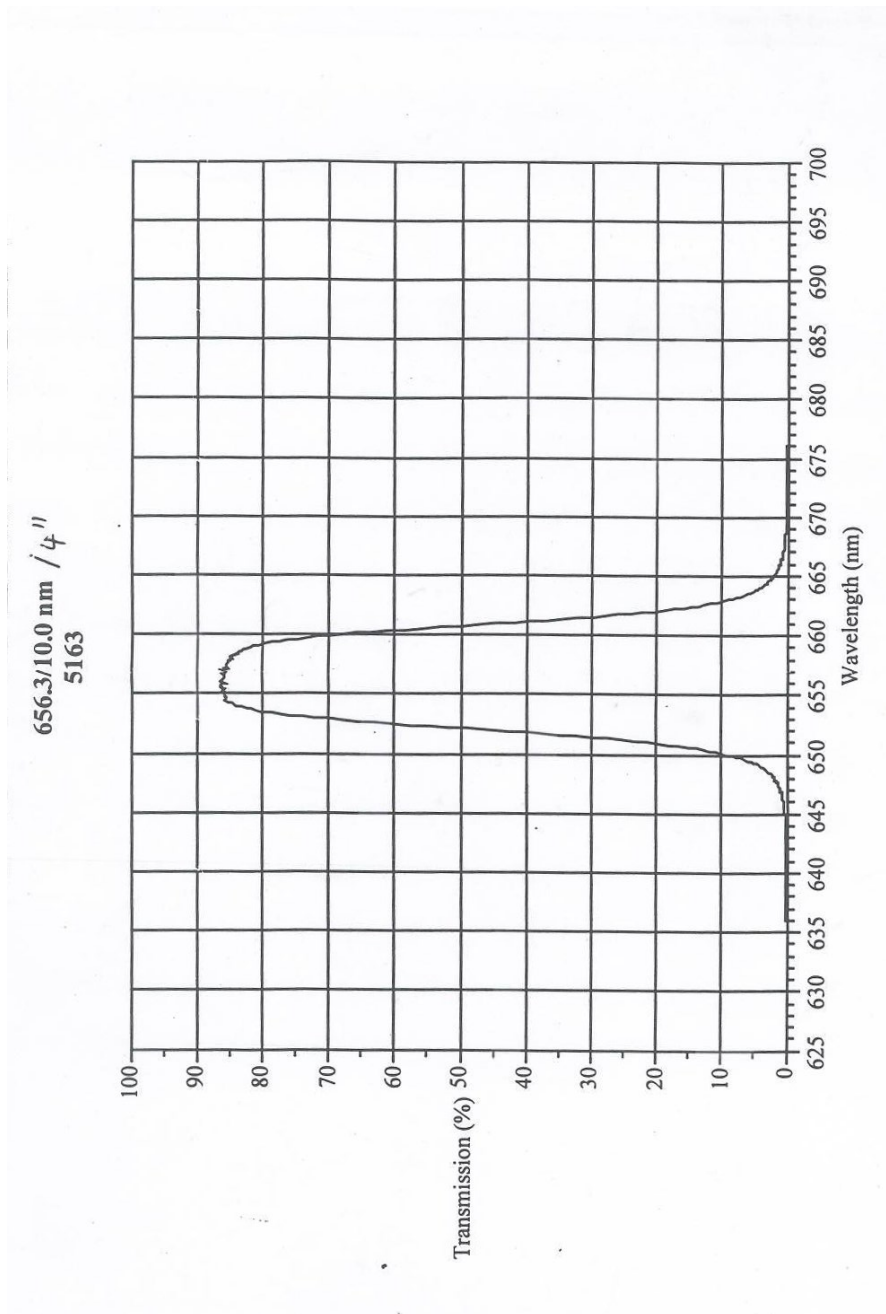


FIGURE A.1: HCT-H $\alpha$  Filter response curve ( 656.3/10.0 Å )

# Appendix B

## Solar abundances

Solar abundances as per Asplund, Grevesse & Sauval 2005

Atom (X)	A	ATW	log n	n(X)/n(H) (by number)	n(X)/n(He) (by number)	mass fraction
H	1	1.0080	12.00	1.000E+00	1.175E+01	7.347E-01
He	2	4.0026	10.93	8.511E-02	1.000E+00	2.483E-01
Li	3	6.9390	1.05	1.122E-11	1.318E-10	5.675E-11
Be	4	9.0120	1.38	2.399E-11	2.818E-10	1.576E-10
B	5	10.8100	2.70	5.012E-10	5.888E-09	3.949E-09
C	6	12.0100	8.39	2.455E-04	2.884E-03	2.149E-03
N	7	14.0100	7.78	6.026E-05	7.079E-04	6.153E-04
O	8	16.0000	8.66	4.571E-04	5.370E-03	5.331E-03
F	9	19.0000	4.56	3.631E-08	4.266E-07	5.028E-07
Ne	10	20.1800	7.84	6.918E-05	8.128E-04	1.018E-03
Na	11	23.0000	6.17	1.479E-06	1.738E-05	2.480E-05
Mg	12	24.3100	7.53	3.388E-05	3.981E-04	6.004E-04
Al	13	26.9800	6.37	2.344E-06	2.754E-05	4.610E-05
Si	14	28.0900	7.51	3.236E-05	3.802E-04	6.625E-04
P	15	30.9700	5.36	2.291E-07	2.692E-06	5.171E-06
S	16	32.0600	7.14	1.380E-05	1.622E-04	3.226E-04
Cl	17	35.4500	5.50	3.162E-07	3.715E-06	8.171E-06
Ar	18	39.9500	6.18	1.514E-06	1.778E-05	4.407E-05
K	19	39.1000	5.08	1.202E-07	1.413E-06	3.426E-06
Ca	20	40.0800	6.31	2.042E-06	2.399E-05	5.965E-05
Sc	21	44.9600	3.05	1.122E-09	1.318E-08	3.677E-08
Ti	22	47.9000	4.90	7.943E-08	9.333E-07	2.773E-06
V	23	50.9400	4.00	1.000E-08	1.175E-07	3.713E-07
Cr	24	52.0000	5.64	4.365E-07	5.129E-06	1.655E-05
Mn	25	54.9400	5.39	2.455E-07	2.884E-06	9.830E-06
Fe	26	55.8500	7.45	2.818E-05	3.311E-04	1.147E-03
Co	27	58.9300	4.92	8.318E-08	9.772E-07	3.573E-06
Ni	28	58.7100	6.23	1.698E-06	1.995E-05	7.267E-05

FIGURE B.1: Element abundances in the present-day solar photosphere. (Asplund, Grevesse & Sauval 2005)

# Appendix C

## Empirical calibrations of the oxygen abundance

Oxygen abundance is important as one of the fundamental characteristics of a galaxy: its radial distribution is combined with radial distributions of gas and star surface mass densities to constrain models of chemical evolution. Parameters defined in empirical calibrations involving bright oxygen lines are

$$R_3 = \frac{I([\text{O III}])\lambda 4959 + I([\text{O III}])\lambda 5007}{\text{H}\beta}, \quad (\text{C.1})$$

$$R_2 = \frac{I([\text{O II}])\lambda 3727}{\text{H}\beta}, \quad (\text{C.2})$$

$$R_{23} = R_3 + R_2, \quad (\text{C.3})$$

$$P = \frac{R_3}{R_{23}}, \quad (\text{C.4})$$

$$y = \log \frac{R_3}{R_2} = \log \frac{1}{P^{-1} - 1}. \quad (\text{C.5})$$

[Jensen, Strom & Strom \(1976\)](#) presented the first exploration in this method considering the  $R_3$  index, which considers the  $[\text{O III}] \lambda\lambda 4959, 5007$  emission lines. However, were [Pagel et al. \(1979\)](#) who introduced the most widely used abundance indicator, the  $R_{23}$  index, which also included the bright  $[\text{O II}] \lambda 3727$  emission line. Since then, many studies have been performed to refine the calibration

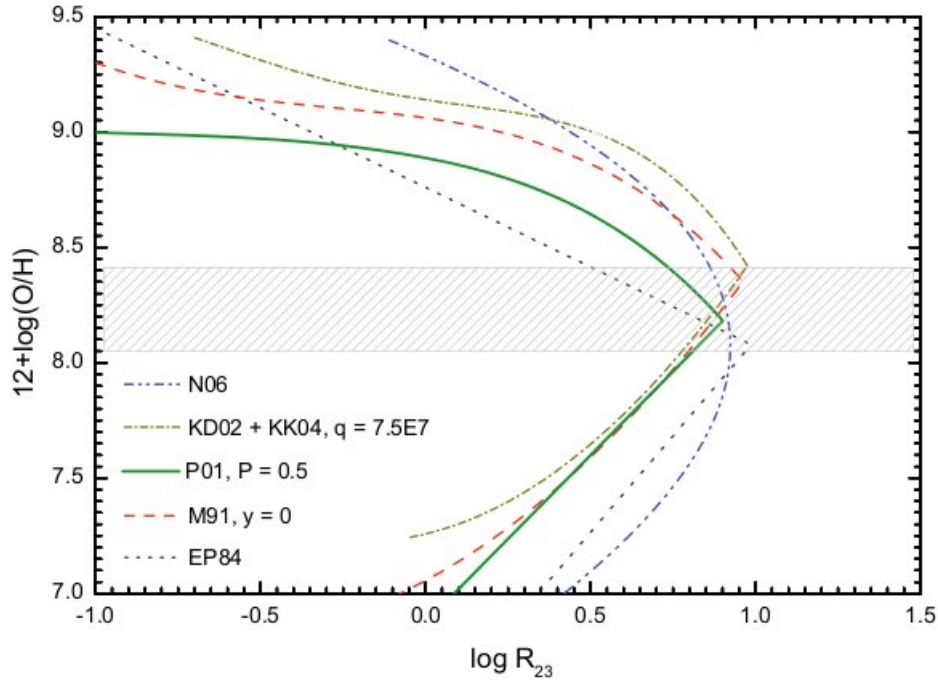


FIGURE C.1: Empirical calibrations of oxygen abundance using the  $R_{23}$  parameter. Note that they are bi-valuated. The dashed zone indicates the region with higher uncertainties in O/H. The empirical calibrations plotted in the figure are: EP94: Edmund & Pagel (1984); M91: McGaugh (1991) using  $y=0$  ( $R_2 = R_3$ ); P01: Pilyugin (2001) using  $P = 0.5$  ( $R_2 = R_3$ ); (KD02+KK04): Kewley & Dopita (2002) using the formulation of Kobulnicky & Kewley (2004) assuming  $q = 7.5 \times 10^7$  cm s $^{-1}$ ; N06: Nagao et al. (2006) using their cubic fit to  $R_{23}$  (Lopez sanchez et al 2010).

of  $R_{23}$  (Edmunds & Pagel 1984; McCall, Rybski & Shields, 1985; Dopita & Evans 1986; Torres-Peimbert et al. 1989; McGaugh 1991; Zaritsky, Kennicutt & Huchra 1994; Pilyugin 2000, 2001a,b; Kewley & Dopita 2002; Kobulnicky & Kewley 2004; Pilyugin & Thuan 2005; Nagao, Maiolino & Marconi 2006). The most successful are the calibrations of McGaugh (1991) and Kewley & Dopita (2002), which are based on photoionization models, and the empirical relations provided by Pilyugin (2001a,b) and Pilyugin & Thuan (2005). Both kinds of calibrations improve the accuracy by making use of the [O III]/[O II] ratio as ionization parameter, which accounts for the large scatter found in the  $R_{23}$  versus oxygen abundance calibration, which is larger than observational errors (Kobulnicky, Kennicutt & Pizagno 1999). Figure C.1 shows the main empirical calibrations that use the  $R_{23}$  parameter.

The main problem associated with the use of  $R_{23}$  parameter is that it is **bivaluated**, i.e., a single value of  $R_{23}$  can be caused by two very different oxygen abundances. The reason of this behaviour is that the intensity of oxygen lines *does not indefinitely increase* with metallicity. Thus, there are two *branches* for each empirical calibration (see Fig. C.1): the *low-metallicity* regime, with  $12+\log(\text{O}/\text{H})\leq 8.1$ , and the *high-metallicity* regime, with  $12+\log(\text{O}/\text{H})\geq 8.4$ . That means that a very large fraction of the star-forming regions lie in the ill-defined turning zone around  $12+\log(\text{O}/\text{H})\simeq 8.20$ , where regions with the same  $R_{23}$  value have oxygen abundances that differ by almost an order of magnitude. Hence, additional information, such as the  $[\text{N II}]/\text{H}\alpha$  or the  $[\text{O II}]/[\text{O III}]$  ratios, is needed to break the degeneracy between the high and low branches (i.e., Kewley & Dopita, 2002). Besides, the  $R_{23}$  method requires that spectrophotometric data are corrected by reddening, which effect is crucial because  $[\text{O II}]$  and  $[\text{O III}]$  lines have a considerably separation in wavelength.

Here we list all empirical calibrations that were considered in this work, compiling the equations needed to derive the oxygen abundance from bright emission line ratios following every method.

**Edmund & Pagel (1984):** Although the  $R_{23}$  parameter was firstly proposed by Pagel et al. (1979), the first empirical calibration was given by Edmunds & Pagel (1984),

$$\begin{aligned} 12 + \log(\text{O}/\text{H})_{up} &= 8.76 - 0.69 \log R_{23}, \\ 12 + \log(\text{O}/\text{H})_{low} &= 6.43 + 1.67 \log R_{23}, \end{aligned} \tag{C.6}$$

with the limit between the lower and the upper branches at  $12+\log(\text{O}/\text{H})\sim 8.0$ .

**McCall, Rybski & Shields (1985)** presented an empirical calibration for oxygen abundance using the  $R_{23}$  parameter, only valid for  $12+\log(\text{O}/\text{H})>8.15$ . However, they did not give an analytic formulae but only listed it numerically (see their Table 15). The four-order polynomial fit for their values gives the

following relation:

$$12 + \log(\text{O}/\text{H})_{up} = 9.32546 - 0.360465x + 0.203494x^2 + 0.278702x^3 - 1.36350x^4 \quad (\text{C.7})$$

with  $x = \log R_{23}$ .

**Zaritzky, Kennicutt & Huchra (1994)** provided a simple analytic relation between oxygen abundance and  $R_{23}$ :

$$12 + \log(\text{O}/\text{H})_{up} = 9.265 - 0.33x - 0.202x^2 - 0.207x^3 - 0.333x^4. \quad (\text{C.8})$$

Their formula is an average of three previous calibrations: [Edmunds & Pagel \(1984\)](#), [McCall et al. \(1985\)](#) and [Dopita & Evans \(1986\)](#). Following the authors, this calibration is only suitable for  $12 + \log(\text{O}/\text{H}) > 8.20$ , but perhaps a more realistic lower limit is 8.35.

**McGaugh (1991)** calibrated the relationship between the  $R_{23}$  ratio and gas-phase oxygen abundance using H II region models derived from the photoionization code CLOUDY ([Ferland et al. 1998](#)). McGaugh's models include the effects of dust and variations in ionization parameter,  $y$ . [Kobulnicky et al. \(1999\)](#) give analytical expressions for the [McGaugh \(1991\)](#) calibration based on fits to photoionization models; the middle point between both branches is  $12 + \log(\text{O}/\text{H}) \sim 8.4$ :

$$12 + \log(\text{O}/\text{H})_{up} = 7.056 + 0.767x + 0.602x^2 - y(0.29 + 0.332x - 0.331x^2) \quad (\text{C.9})$$

$$12 + \log(\text{O}/\text{H})_{low} = 9.061 - 0.2x - 0.237x^2 - 0.305x^3 - 0.0283x^4$$

$$-y(0.0047 - 0.0221x - 0.102x^2 - 0.0817x^3 - 0.00717x^4) \quad (\text{C.10})$$

**Pilyugin (2000)** found that the previous calibrations using the  $R_{23}$  parameter had a systematic error depending on the hardness of the ionizing radiation, suggesting that the excitation parameter,  $P$ , is a good indicator of it. In several papers, Pilyugin performed a detailed analysis of the observational

data combined with photoionization models to obtain empirical calibrations for the oxygen abundance. Pilyugin (2000) confirmed the idea of McGaugh (1991) that the strong lines of [O II] and [O III] contain the necessary information for the determination of accurate abundances in low-metallicity (and may be also in high-metallicity) H II regions. He used new observational data to propose a linear fit involving only the  $R_{23}$  parameter,

$$12 + \log(\text{O}/\text{H})_{up} = 9.50 - 1.40 \log R_{23}, \quad (\text{C.11})$$

$$12 + \log(\text{O}/\text{H})_{low} = 6.53 + 1.40 \log R_{23}, \quad (\text{C.12})$$

assuming a limit of  $12 + \log(\text{O}/\text{H}) \sim 8.0$  between the two branches. This calibration is close to that given by Edmunds & Pagel (1984); it has the same slope, but Pilyugin (2000) is shifted towards lower abundances by around 0.07 dex. However, this new relation is not sufficient to explain the wide spread of observational data. Thus, Pilyugin (2001a) give the following, more real and complex, calibration involving also the excitation parameter  $P$ :

$$12 + \log(\text{O}/\text{H})_{up} = \frac{R_{23} + 54.2 + 59.45P + 7.31P^2}{6.01 + 6.71P + 0.371P^2 + 0.243R_{23}}. \quad (\text{C.13})$$

This is the so-called *P-method*, which can be used in moderately high-metallicity H II regions ( $12 + \log(\text{O}/\text{H}) \geq 8.3$ ). Pilyugin used two-zone models of H II regions and assumed the  $T_e(\text{O II}) - T_e(\text{O III})$  relation from Garnett (1992). For the low metallicity branch, Pilyugin (2001b) found that

$$12 + \log(\text{O}/\text{H})_{low} = 6.35 + 1.45 \log R_{23} - 1.74 \log P. \quad (\text{C.14})$$

Pilyugin estimates that the precision of oxygen abundance determination with this method is around 0.1 dex.

**Pilyugin & Thuan (2005)** revisited these calibrations including more spectroscopic measurements of H II regions in spiral and irregular galaxies with a measured intensity of the [O III]  $\lambda 4363$  line and recalibrate the relation between

the oxygen abundance and the  $R_{23}$  and  $P$  parameters, yielding to:

$$12 + \log(\text{O}/\text{H})_{low} = \frac{R_{23} + 106.4 + 106.8P - 3.40P^2}{17.72 + 6.60P + 6.95P^2 - 0.302R_{23}}, \quad (\text{C.15})$$

$$12 + \log(\text{O}/\text{H})_{up} = \frac{R_{23} + 726.1 + 842.2P + 337.5P^2}{85.96 + 82.76P + 43.98P^2 + 1.793R_{23}}. \quad (\text{C.16})$$

**Kewley & Dopita (2002)** used a combination of stellar population synthesis and photoionization models to develop a set of ionization parameters and abundance diagnostic based only on the strong optical emission lines. Their *optimal* method uses ratios of [N II], [O II], [O III], [S II], [S III] and Balmer lines, which is the full complement of strong nebular lines accessible from the ground. They also recommend procedures for the derivation of abundances in cases where only a subset of these lines is available. **Kewley & Dopita (2002)** models start with the assumption that  $R_{23}$ , and many of the other emission-line abundance diagnostics, also depends on the **ionization parameter**  $q \equiv c \times U$ , that has units of  $\text{cm s}^{-1}$ . They used the stellar population synthesis codes STARBURST 99 (**Leitherer et al. 1999; Vázquez & Leitherer 2005**) and PEGASE.2 (**Fioc & Rocca-Volmerange 1997**) to generate the ionizing radiation field, assuming burst models at zero age with a Salpeter IMF and lower and upper mass limits of 0.1 and  $120 M_{\odot}$ , respectively, with metallicities between 0.05 and 3 times solar. The ionizing radiation fields were input into the photoionization and shock code, MAPPINGS (**Sutherland & Dopita 1993**), which includes self-consistent treatment of nebular and dust physics. **Kewley & Dopita (2002)** previously used these models to simulate the emission-line spectra of H II regions and starburst galaxies (**Dopita et al. 2000**), and are completely described in their study.

**Kobulnicky & Kewley (2004)** gave a parameterization of the **Kewley & Dopita (2002)**  $R_{23}$  method with a form similar to that given by **McGaugh (1991)** calibration. **Kobulnicky & Kewley (2004)** presented an iterative scheme to resolve for both the ionization parameter  $q$  and the oxygen abundance using

only [O III], [O II] and H $\beta$  lines. The parameterization they give for  $q$  is

$$\log(q) = \frac{32.81 - 1.153y^2 + [12 + \log(\text{O}/\text{H})] [-3.396 - 0.025y + 0.1444y^2]}{4.603 - 0.3119y - 0.163y^2 + [12 + \log(\text{O}/\text{H})] [-0.48 + 0.0271y + 0.02037y^2]} \quad (\text{C.17})$$

where  $y = \log([\text{O III}]/[\text{O II}])$ . This equation is only valid for ionization parameters between  $5 \times 10^6$  and  $1.5 \times 10^8 \text{ cm s}^{-1}$ . The oxygen abundance is parameterized by

$$12 + \log(\text{O}/\text{H})_{up} = 9.72 - 0.777x - 0.951x^2 - 0.072x^3 - 0.811x^4 - \log(q) \\ \times (0.0737 - 0.0713x - 0.141x^2 + 0.0373x^3 - 0.058x^4) \quad (\text{C.18})$$

$$12 + \log(\text{O}/\text{H})_{low} = 9.40 + 4.65x - 3.17x^2 - \log(q)(0.272 + 0.547x - 0.513x^2) \quad (\text{C.19})$$

being  $x = \log R_{23}$ . The first equation is valid for  $12 + \log(\text{O}/\text{H}) \geq 8.4$ , while the second for  $12 + \log(\text{O}/\text{H}) < 8.4$ . Typically, between two and three iterations are required to reach convergence. Following the authors, this parameterization should be regarded as an improved, implementation-friendly approach to be preferred over the tabulated  $R_{23}$  coefficients given by [Kewley & Dopita \(2002\)](#).

**Nagao, Maiolino & Marcani (2006)** did not consider any ionization parameter. They merely used data of a large sample of galaxies from the SDSS to derive a cubic fit to the relation between  $R_{23}$  and the oxygen abundance,

$$\log R_{23} = 1.2299 - 4.1926y + 1.0246y^2 - 0.063169y^3, \quad (\text{C.20})$$

with  $y = 12 + \log(\text{O}/\text{H})$ .

Besides  $R_{23}$ , additional parameters have been used to derive metallicities in star-forming galaxies. Without other emission lines, the  $N_2$  **parameter**, which is defined by

$$N_2 \equiv \log \frac{I([\text{N II}])\lambda 6583}{\text{H}\alpha}, \quad (\text{C.21})$$

can be used as a crude estimator of metallicity. However, we note that the

[N II]/H $\alpha$  ratio is particularly sensitive to shock excitation or a hard radiation field from an AGN. The  $N_2$  parameter was firstly suggested by [Storchi-Bergmann, Calzetti & Kinney \(1994\)](#), who gave a tentative calibration of the oxygen abundance using this parameter. This calibration has been revisited by [van Zee, Salzer & Haynes \(1998\)](#); [Denicoló, Terlevich & Terlevich \(2002\)](#); [Pettini & Pagel \(2004\)](#) and [Nagao et al. \(2006\)](#). The **Denicoló et al. (2002)** calibration is

$$12 + \log(\text{O}/\text{H}) = 9.12 + 0.73N_2, \quad (\text{C.22})$$

which considerably improves the previous relations because of the inclusion of an extensible sample of nearby extragalactic H II regions. The uncertainty of this method is  $\sim 0.2$  dex because  $N_2$  is sensitive to ionization and O/N variations, so strictly speaking it should be used mainly as an indicator of galaxy-wide abundances. [Denicoló et al. \(2002\)](#) also compared their method with photoionization models, concluding that the observed  $N_2$  is consistent with nitrogen being a combination of both primary and secondary origin.

[Pettini & Pagel \(2004\)](#) revisited the relation between the  $N_2$  parameter and the oxygen abundance including new data for the high- and low-metallicity regimen. They only considered those extragalactic H II regions where the oxygen values are determined either via the  $T_e$  method or with detailed photoionization modelling. Their linear fit to their data is

$$12 + \log(\text{O}/\text{H}) = 8.90 + 0.57N_2, \quad (\text{C.23})$$

which has both a lower slope and zero-point than the fit given by [Denicoló et al. \(2002\)](#). A somewhat better relation is provided by a third-order polynomial fit of the form

$$12 + \log(\text{O}/\text{H}) = 9.37 + 2.032N_2 + 1.26(N_2)^2 + 0.32(N_2)^3, \quad (\text{C.24})$$

valid in the range  $-2.5 < N_2 < -0.3$ . Nagao et al. (2006) also provided a relation between  $N_2$  and the oxygen abundance, their cubic fit to their SDSS data yields

$$\log N_2 = 96.641 - 39.941y + 5.2227y^2 - 0.22040y^3, \quad (\text{C.25})$$

with  $y=12+\log(\text{O}/\text{H})$ .

Pettini & Pagel (2004) revived the  $O_3N_2$  parameter, previously introduced by Alloin et al. (1979) and defined by

$$O_3N_2 \equiv \log \frac{[\text{O III}] \lambda 5007 / \text{H}\beta}{[\text{N II}] \lambda 6583 / \text{H}\alpha}. \quad (\text{C.26})$$

Pettini & Pagel (2004) derived the following least-square linear fit to their data:

$$12 + \log(\text{O}/\text{H}) = 8.73 - 0.32O_3N_2. \quad (\text{C.27})$$

Nagao et al. (2006) also revisited this calibration and derived a cubic fit between the  $O_3N_2$  parameter and the oxygen abundance,

$$\log O_3N_2 = -232.18 + 84.423y - 9.9330y^2 + 0.37941y^3, \quad (\text{C.28})$$

with  $y=12+\log(\text{O}/\text{H})$ .

Other important empirical calibrations that were not used in this study involve the  $S_{23}$  parameter, introduced by Vílchez & Esteban (1996) and revisited by Díaz & Pérez-Montero (2000); Oey & Shields (2000) and Pérez-Montero & Díaz (2005). In the last years, bright emission line ratios such as  $[\text{Ar III}]/[\text{O III}]$  and  $[\text{S III}]/[\text{O III}]$  (Stasińska 2006) or  $[\text{Ne III}]/[\text{O III}]$  and  $[\text{O III}]/[\text{O II}]$  (Nagao et al. 2006) have been explored as indicators of the oxygen abundance in H II regions and starburst galaxies. Peimbert et al. (2007) suggested to use the oxygen recombination lines to get a more precise estimation of the oxygen abundance. Nowadays, there is still a lot of observational and theoretical work to do involving empirical calibrations (see recent review by Kewley & Ellison 2008), but

---

these methods should be used only for objects whose H II regions have the same structural properties as those of the calibrating samples ([Stasińska 2009](#))([López-Sánchez 2010](#)).

# BIBLIOGRAPHY

- Alloin D., Collin-Souffrin S., Joly M. & Vigroux L. 1979, A&A, 78, 200
- Allen D. A., Wright A. E., Goss W. M., 1976, MNRAS, 177, 91
- Alonso-Herrero, A., Rieke, M. J., Rieke, G. H. & Shields, J. C. 2000, ApJ, 530, 688
- Amorín, R., Pérez-Montero, E., Vílchez, J.M. & Papaderos, P. 2012, ApJ, in press (arXiv:1202.3419)
- Amorín, R. O.; Muñoz-Tuñón, C., Aguerri, J.A.L., Cairós, L.M. & Caon, N. 2007, A&A, 467, 541
- Asplund, M., Grevesse, N. & Sauval, A. J. 2005, in ASP Conf. Ser. 335, *Cosmic Abundances as Records of Stellar Evolution and Nucleosynthesis*, ed. F.N. Bash & T.G. Barnes (San Francisco: ASP), 25
- Baldwin J., Phillips M., & Terlevich R., 1981, PASP, 93, 5
- Begelman M. C., Blandford R. D., Rees M. J., 1984, RvMP, 56, 255
- Bresolin, F., Gieren, W., Kudritzki, R-P., Pietrzyński, G., Urbaneja, M.A. & Carraro, G. 2009, ApJ, 700, 309
- Brinchmann J., Kunth D., Durret F., 2008, A & A, 485, 657
- Brinchmann, J., Kunth, D., & Durret, F. 2008, A&A, 485, 657
- Buckalew, B.A., Kobulnicky, H.A. & Dufour, R.J. 2005, ApJS, 157, 30

- Bushouse H. A., 1986, *AJ*, 91, 255
- Cardelli J. A., Clayton G. C., Mathis J. S., 1989, *Apj*, 345, 245
- Calzetti, D. et al. 2007, *ApJ*, 666, 870
- Cardelli, J. A., Clayton, G. C. & Mathis J. S. 1989, *ApJ*, 345, 245
- Carini M. T., Miller H. R., Goodrich B. D., 1990, *AJ*, 100, 347
- Charlot S., Fall S. M., 2000, *Apj*, 539, 718
- Condon, J.J. 1992, *ARA&A* 30, 575
- Conti P. S., 1991, *Apj*, 377, 115
- Condon, J. J., Cotton, W. D., Greisen, E. W., Yin, Q. F., Perley, R. A., Taylor, G. B. & Broderick, J. J. 1998, *AJ*, 115, 1693
- Condon, J.J., Cotton, W.D. & Broderick, J.J. 2002, *AJ*, 124, 675
- Conti, P.S., 1976, *MSRSL*, 9, 193
- Conti, P.S., 1991, *Apj*, 377, 115
- Conselice, C.J., Gallagher, J.S., Calzetti, D., Homeier, N. & Kinney, A. 2000, *AJ*, 119, 79
- Crowther P. A., 2007, , 45, 177
- de Naray R. K., McGaugh S. S. & de Blok W. J. G., 2004, *MNRAS*, 355, 887
- H. Dottori, J. Cepa, J. Vílchez & C.S. Barth, 1994, *A&A*, 283, 753
- Denicoló, G., Terlevich, R. & Terlevich, E. 2002, *MNRAS*, 330, 69
- Díaz, A.I., & Pérez-Montero, E. 2000, *MNRAS*, 312, 130
- Dinerstein, H.L. & Shield, G.A. 1986, *ApJ*, 311, 45
- Dopita, M.A. & Evans, I. N. 1986, *ApJ*, 307, 431

- Dopita, M.A., Kewley, L. J., Heisler, C.A. & Sutherland, R.S. 2000, *ApJ*, 542, 224
- Eckart, A., Cameron, M., Jackson, J. M., Genzel, R., Harris, A. I., Wild, W. & Zinnecker, H. 1991, *ApJ*, 372, 67
- Eckart, A., Cameron, M., Boller, Th., Krabbe, A., Blietz, M., Nakai, N., Wagner, S. J. & Sternberg, A. 1996, *AJ*, 472, 58
- Edmunds, M.G. & Pagel, B.E.J. 1978, *MNRAS*, 185, 77
- Edmunds, M.G. & Pagel, B.E.J. 1984, *MNRAS*, 211, 507
- Esteban, C., Peimbert, M., García-Rojas, J., Ruiz, M. T., Peimbert, A. & Rodríguez, M., 2004, *MNRAS*, 355, 229
- Esteban, C., Bresolin, F., Peimbert, M., García-Rojas, J., Peimbert, A. & Mesa-Delgado, A. 2009, *ApJ*, 700, 654
- Ferland G. J., Korista K. T., Verner D. A., Ferguson J. W., Kingdon J. B. & Verner E. M, 1998, *PASP*, 110, 761
- Fernandes, I.F., de Carvalho, R., Contini, T. & Gal, R.R. 2004, *MNRAS* 355, 728
- Fioc, M. & Rocca-Volmerange, B. 1997, *A&A* 326, 950
- French, H. B. 1980, *Apj*, 240, 41
- Gallagher, S.C., Durrell. P.R., Elmegreen, D.M., Chandar, R. English, J., Charlton, J.C., Gronwall, C., Young, J., Tzanavaris, P., Johnson, K.E., Mendes de Oliveira, C., Whitmore, B., Hornschemeier, A.E., Maybhate, A. & Zabludoff, A. 2010, *AJ*, 139, 545
- Garnett, D.R. 1992, *AJ*, 103, 1330
- Genzel R., Lutz D., Tacconi L., 1998, , 395, 859

- García-Rojas, J., Esteban, C., Peimbert, A., Peimbert, M., Rodríguez, & M., Ruiz, 2005, MNRAS, 362, 301
- Garnett, D.R. 1992, AJ, 103, 1330
- Garnett, D.R. 2003, lectures on *Cosmochemistry: The melting pot of the elements*. XIII Canary Islands Winter School of Astrophysics, Puerto de la Cruz, Tenerife, Spain, November 19-30, 2001, edited by C. Esteban, R. J. García López, A. Herrero, F. Sánchez. Cambridge contemporary astrophysics. Cambridge, UK: Cambridge University Press, ISBN 0-521-82768-X, 2004, p. 171
- Garnett, D.R., Kennicutt, R. C.Jr., Chu, Y.-H. & Skillman E. D. 1991, ApJ, 373, 458
- Gullixson C. A., 1992, in S. B. Howell ed., *Astronomical CCD Observing and Reduction Techniques* Vol. 23 of *Astronomical Society of the Pacific Conference Series*, Two Dimensional Imagery. p. 130
- Guseva N. G., Izotov Y. I., Thuan T. X., 2000, Apj, 531, 776
- Guseva, N., Izotov, Y. I. & Thuan, T.X. 2000, ApJ, 531, 776
- Hoopes, C.G., Walterbos, R. A. M. & Rand, R.J. 1999, ApJ, 522, 669
- Hopkins, A. M., Schulte-Ladbeck, R. E. & Drozdovsky, I. O. 2002, AJ, 124, 862
- Huang, Jiehao; Gu, Qiusheng; Su, Hongjun; Shang, Zhaohui, 1996, Ap&SS, 235, 109
- Huang, J.H., Gu, Q.S., Ji,L., Li, W.D., Wei, J.Y. & Zheng, W. 1999, ApJ, 513, 215
- Hunter D. A., 1982, ApJ, 260, 81
- Hunter D. A., Gallagher, J. & Rautenkranz, D. 1982, ApJS, 49, 53
- Hunter D. A., O Connell R. W., Gallagher III J. S., 1994a, AJ, 108, 84

- Hunter D. A., van Woerden H., Gallagher III J. S., 1994b, *ApJS*, 91, 79
- Hunter D. A., & Hoffman, L. 1999, *AJ*, 117, 2789
- Izotov, Y. I., Foltz, C. B., Green, R. F., Guseva, N. G. & Thuan T. X., 1997, *ApJ*, 487, L37
- Izotov, Y.I. & Thuan, T.X. 1998, *ApJ*, 500, 188
- Izotov, Y.I. & Thuan, T.X. 1999, *ApJ*, 511, 639
- Izotov, Y.I., Papaderos, P., Guseva, N.G., Fricke, K.J. & Thuan, T.X. 2004, *A&A* 421, 539
- Izotov, Y.I., Stasińska, G., Meynet, G., Guseva, N.G. & Thuan, T.X. 2006, *A&A*, 448, 955
- James, B.L., Tsamis, Y.G., Barlow, M.J., Westmoquette, M.S., Walsh, J.R., Cuisinier, F. & Exter, K.M. 2009, *MNRAS*, 398, 2
- Jensen E. B., Strom K. M. & Strom S. E. 1976, *ApJ*, 209, 748
- Karachentsev, I.D., Sharina, M. E., Dolphin, A. E., Grebel, E. K., Geisler, D., Guhathakurta, P., Hodge, P. W., Karachentseva, V. E., Sarajedini, A. & Seitzer, P. 2003, *A&A*, 398, 467
- Kataoka J., et al., 2001, *ApJ*, 560, 659
- Kauffmann, G. et al. 2003, *MNRAS*, 346, 1055
- Kennicutt, R.C. Jr. 1998, *ARAA*, 36, 189
- Kennicutt, R.C. Jr., Bresolin, F. & Garnett, D.R. 2003, *ApJ*, 591, 801
- Kennicutt, R. C., Jr., Lee, J.C., Funes, S.J., José G., Sakai, S., & Akiyama, S. 2008, *ApJS*, 178, 247
- Kewley, L.J., Dopita, M.A., Sutherland, R.S., Heisler, C.A. & Trevena, J. 2001, *ApJS*, 556, 121

- Kewley, L.J. & Dopita, M.A. 2002, *ApJS*, 142, 35
- Kewley, L.J., & Ellison, S.E. 2008, *ApJ*, 681, 1183
- Kinman, T.D. & Davidson, K. 1981, *ApJ*, 243, 127
- Kong X., Cheng F. Z., Weiss A., Charlot S., 2002, *A & A*, 396, 503
- Kobulnicky, H.A., Skillman, E.D., Roy, J.-R., Walsh, J.R. & Rosa, M.R., 1997, *ApJ*, 277, 679
- Kobulnicky, H.A. & Skillman, E.D. 1998, *ApJ*, 497, 601
- Kobulnicky, H.A, Kennicutt, R.C.Jr. & Pizagno, J.L. 1999, *ApJ* 514, 544
- Kobulnicky, H. A. & Kewley L. J. 2004, *ApJ*, 617, 240
- Koribalski, B.S. & López-Sánchez, Á.R. 2009, *MNRAS*, 400, 1749
- Kunth D., Joubert M., 1985, *A & A*, 142, 411
- Kunth D., Schild H., 1986, *A & A*, 169, 71
- Kunth D., Contini T., 1999, in K. A. van der Hucht, G. Koenigsberger, & P. R. J. Eenens ed., *Wolf-Rayet Phenomena in Massive Stars and Starburst Galaxies Vol. 193 of IAU Symposium, Wolf-Rayet stars as tracing the AGN-starburst connection.* p. 725
- Kunth D., Östlin G., 2000, , 10, 1
- Larson R. B., Tinsley B. M., 1978, *Apj*, 219, 46
- Landolt A.U. 1992, *AJ*, 104, 340
- Landolt A. U., 1992, *AJ*, 104, 340
- Lee, J.C., Salzer J.J. & Melbourne, J. 2004, *ApJ*, 616, 752L
- Leitherer C., Ortiz Otálvaro P. A., Bresolin F., Kudritzki R.-P., Lo Faro B., Pauldrach A. W. A., Pettini M., Rix S. A., 2010, *Apj*, 189, 309

- Leitherer C., Schaerer D., Goldader J. D., González Delgado R. M., Robert C., Kune D. F., de Mello D. F., Devost D., Heckman T. M., 1999, *Apj*, 123, 3
- Leitherer, C., Schaerer, D., Goldader, J.D., González-Delgado, R.M., Robert, C., Kune, D.F., de Mello, D.F., Devost, D. & Heckman, T.M. 1999, *ApJS*, 123, 3
- Leon, S.; Eckart, A.; Laine, S.; Kotilainen, J. K.; Schinnerer, E.; Lee, S.-W.; Krips, M.; Reunanen, J. & Scharwachter, J. 2007, *A&A*, 473, 747
- Lutz D., Genzel R., Sternberg A., Netzer H., Kunze D., Rigopoulou D., Sturm E., Egami E., Feuchtgruber H., Moorwood A. F. M., de Graauw T., 1996, *A & A*, 315, L137
- Lutz D., Spoon H. W. W., Rigopoulou D., Moorwood A. F. M., Genzel R., 1998, , 505, L103
- López-Sánchez, Á.R. 2010, *A&A*, 521, 63
- López-Sánchez, Á.R., Esteban, C. & Rodríguez, M. 2004a, *ApJS*, 153, 243
- López-Sánchez, Á.R., Esteban, C. & Rodríguez, M. 2004b, *A&A* 428,445
- López-Sánchez, Á.R., Esteban, C. & García-Rojas, J. 2006, *A&A*, 449, 997
- López-Sánchez, Á.R., Esteban, C., García-Rojas, J., Peimbert, M. & Rodríguez, M. 2007, *ApJ*, 656, 168
- López-Sánchez, Á.R. & Esteban, C. 2008, *A&A*, 491, 131
- López-Sánchez, Á.R. & Esteban, C. 2009, *A&A*, 508, 615
- López-Sánchez, Á.R. & Esteban, C. 2010a, *A&A*, 516, 104
- López-Sánchez, Á.R. & Esteban, C. 2010b, *A&A*, 517, 85
- López-Sánchez, Á.R., Mesa-Delgado, A., López-Martín, L & Esteban, C. 2011, *MNRAS*, 411, 2076

- López-Sánchez, Á.R., Dopita, M.A., Kewley, L.J., Zahid, H.J., Nicholls, D.C. & Scharwächter, J. 2012, MNRAS, accepted
- Maeder A., Conti P. S., 1994, , 32, 227
- Massey P., Strobel K., Barnes J. V., Anderson E., 1988, Apj, 328, 315
- Marscher A. P., 1996, in Blazar continuum variability, eds. H.R. Miller, J.R. Webb, and J.C. Noble, ASP Conf. Ser. Vol. 110, (San Francisco: ASP), p. 248
- Martin, C. L. 1997, ApJ, 491, 561
- Masegosa, M., Moles, M. & del Olmo, A. 1991, A&A, 244, 273
- McCall, M.L., Rybski, P.M. & Shields, G.A. 1985, ApJS 57, 1
- McGaugh, S.S. 1991, ApJ, 380, 140
- Méndez, D.I. & Esteban, C., 2000, A&A, 359, 493
- Meynet G. & Maeder A. 2005. A&A, 429, 581
- Moll, S.L., Mengel, S., de Grijs, R., Smith, L. J. & Crowther, P.A. 2007, MNRAS, 382, 1877
- Mollá, M., Vílchez, J.M., Gavilán, M. & Díaz, A.I. 2006, MNRAS, 372, 1069
- Monreal-Ibero, A., Vílchez, J.M.; Walsh, J.R. & Muñoz-Tuñón, C. 2010, A&A, 517, 27
- Moshir M. et al. 1990, Infrared Astronomical Satellite Catalogs, The Faint Source Catalog, Version 2.0
- Moustakas, J., Kennicutt, R.C., Jr., Tremonti, C. A., Dale, D. A., Smith, J.-D. T. & Calzetti, D. 2010, ApJS, 190, 233
- Nagao, T., Maiolino, R. & Marconi, A. 2006, A&A, 459, 85

- Noeske, K.G., Papaderos, P., Cairós, L.M. & Fricke, K.J. 2003, *A&A*, 410, 481
- Oey M. S. & Shields J. C., 2000, *ApJ*, 539, 687
- O'Donnell J. E., 1994, *Apj*, 422, 158
- Oke, J. B. 1990, *ApJ*, 99, 1621
- Oke J. B., 1990, *AJ*, 99, 1621
- Oey M. S. & Shields J. C., 2000, *ApJ*, 539, 687
- Osterbrock, D.E. & Cohen, R.D. 1982, *ApJ*, 261, 64
- Osterbrock D. E., Ferland G. J., 2006, *Astrophysics of gaseous nebulae and active galactic nuclei*
- Pagel, B. E. J., Edmunds, M. G., Blackwell, D. E., Chun, M. S., Smith, G. 1979, *MNRAS*, 189, 95
- Peimbert, M. & Costero, R. 1969, *Bol. Obs. Ton. y Tac.*, 5, 3
- Peimbert, M., Peimbert, A., Esteban, C.; García-Rojas, J., Bresolin, F., Carigi, L., Ruiz, M.T. & López-Sánchez, Á.R. 2007, *RMxAC*, 29, 72
- Pindao M., Schaerer D., González Delgado R. M., Stasińska G., 2002, *A & A*, 394, 443
- Popescu C. C., Hopp U., 2000, *AAps*, 142, 247
- Pérez-Montero, E., Vílchez, J. M., Cedrés, B., Hägele, G. F.; Mollá, M. Kehrig, C., Díaz, A. I., García-Benito, R. & Martín-Gordón, D. 2011, *A&A*, 532, 141
- Pérez-Montero, E. & Díaz, A. I. 2005, *MNRAS*, 361, 1063
- Pettini, M. & Pagel, B.E.J. 2004, *MNRAS*, 348, 59
- Pilyugin, L.S. 2000, *A&A*, 362, 325

- Pilyugin, L.S. 2001a, A&A, 369, 594
- Pilyugin, L.S. 2001b, A&A, 374, 412
- Pilyugin, L.S. & Thuan, T.X. 2005, ApJ, 631, 231
- Pilyugin, L.S., Víchez, J.M. & Thuan, T.X. 2010, ApJ, 720, 1738
- Pindao, M. 1999, in *IAU Symp. 193: Wolf-Rayet Phenomena in Massive Stars and Starburst Galaxies*, 193, 614
- Pindao, M., Schaerer, D., González-Delgado, R.M. & Stasińska, G. 2002, A&A 394, 443
- Pustilnik, S., Kniazev, A., Pramskij, A., Izotov, Y., Foltz, C., Brosch, N., Martin, J.-M. & Ugryumov, A. 2004, A&A 419, 469
- Rees M. J., 1984, in W. Brinkmann & J. Truemper ed., X-ray and UV Emission from Active Galactic Nuclei Comments on the physics of active galactic nuclei. pp 138–151
- Rieke G. H., Low F. J., 1972, , 176, L95
- Romero G. E., Cellone, S. A., Combi J. A., Andruchow I., 2002, A&A, 390, 431
- Rosales-Ortega, F.F., Díaz, A.I., Kennicutt, R.C. & Sánchez, S.F. 2011, MNRAS, 415, 2439
- Sandage, A. & Tammann, G. A.1981, *A Revised Shapley-Ames Catalog of Bright Galaxies* , Washington, DC; Carnegie Inst. Washington
- Sandage A. R., Miller W. C., 1964, Science, 144, 405
- Sargent W. L. W., Searle L., 1970, , 162, L155
- Schaerer D., Contini T., Pindao M., 1999, A&A, 136, 35
- Schaerer, D. & Vacca, W.D. 1998, ApJ, 497, 618

- Schaerer, D., Contini, T. & Pindao, M. 1999, A&AS 136, 35
- Schlickeiser R., 1996, A&AS, 120, 481
- Schlegel, D.J., Finkbeiner, D.P. & Davis, M. 1998, ApJ, 500, 525
- Shaw, R.A. & Dufour, R.J. 1995, PASP, 107, 896
- Stalin C. S., Gopal-Krishna,
- Stasińska, G. 1978, A&A, 66, 257
- Stasińska, G. 2006, A&A, 454, 127
- Stasińska, G. 2009, proceedings of IAU symposium 262, *Stellar Populations - planning for the next decade*, eds Bruzual & Charlot, astro-ph:0910.0175
- Storchi-Bergmann, T., Calzetti, D. & Kinney, A.L. 1994, ApJ, 429, 572
- Storey, P.J. & Hummer, D.G. 1995, MNRAS 272, 41
- Sutherland, R.S. & Dopita, M.A. 1993, ApJS, 88, 253
- Stoche J. T., Morris S. L., Weymann R. J., Foltz C. B., 1992, ApJ, 396, 487
- Thuan, T.X. & Martin, G.E. 1981, ApJ, 247, 823
- Tinsley B. M., 1968, Apj, 151, 547
- Torres-Peimbert, S., Peimbert, M. & Fierro, J. 1989, ApJ, 345, 186
- Urry C. M., Padovani P., 1995, PASP, 107, 803
- van Zee, L., Salzer, J.J. & Haynes, M.P. 1998, ApJ, 497, 1
- Vázquez, G.A. & Leitherer, C. 2005, ApJ, 621, 695
- Vázquez G. A., Leitherer C., 2005, Apj, 621, 695
- Veilleux S., Kim D.-C., Sanders D. B., Mazzarella J. M., Soifer B. T., 1995, Apj, 98, 171

- Veilleux S., Sanders D. B., Kim D.-C., 1999, *Apj*, 522, 139
- Veilleux, S. & Osterbrock, D.E. 1987, *ApJS*, 63 295
- Verma A., Charmandaris V., Klaas U., Lutz D., Haas M., 2005, , 119, 355
- Vílchez, J.M., & Esteban, C. 1996, *MNRAS*, 280, 720
- de Vaucouleurs G., de Vaucouleurs A., Corwin Jr. H.G., Buta R.J., Paturel G.,  
Fouqué P. 1991, *Third Reference Catalogue of Bright Galaxies* (New York:  
Springer Verlag),
- Waller, W.H. 1990, *PASP*, 102, 1217
- Wagner S. J., Witzel A., 1995, *ARA&A*, 33, 163
- Wiita P. J., 2006, in *Blazar Variability Workshop II: Entering the GLAST Era*  
ASP Conference Series, Vol. 350,
- Whitford A. E., 1958, *AJ*, 63, 201
- Whittet D. C. B., 1994, *Astronomische Nachrichten*, 315, 318
- Xie G. Z., Li K. H., Bai J. M., Dai B. Z., Liu W. W., Zhang X., Xing S. Y.,  
2001, *ApJ*, 548, 200
- York, D.G. et al. 2000, *AJ*, 120, 1579
- Zaritsky, D., Kennicutt, R. C. Jr. & Huchra, J.P. 1994, *ApJ* 420, 87
- Zhang, W., Kong, X., Li, C., Zhou, H.-Y., Cheng, F.-Z. 2007, *ApJ*, 655, 851